Supplementary Information for

Dual-Effect Pre-Potassiation Unlocks Stable and High-Energy Potassium-Ion Batteries

*Nan Li, ‡[a] Yixiang He, ‡[b] Jiacheng Zhu, ‡[c] Xiaofang Wang, ‡[d] Yifan Chen, ‡[a] Yusi Yang, ‡[a] Linlin Wang, ‡[a] Xiaogang Niu, ‡[a] Xiao Ji, *[e] Xuefeng Wang, *[c] Qianfan Zhang, *[b] and Yujie Zhu *[a]*

[a] School of Chemistry, Beihang University, Beijing 100191, People's Republic of China

[b] School of Materials Science and Engineering, Beihang University, Beijing 100191, People's Republic of China

[c] Institute of Physics, Chinese Academy of Sciences, College of Materials Science and Opto-Electronic Technology, University of Chinese Academy of Sciences, Beijing 100190, People's Republic of China

[d] School of Physics, Hubei University, Wuhan, Hubei 430062, People's Republic of China

[e] School of Optical and Electronic Information, Huazhong University of Science and Technology, Wuhan, Hubei 430074, People's Republic of China

Experimental methods

Chemicals

All chemicals and reagents were analytical grade, commercially available, and used as-received. Ethylenediaminetetraacetic acid dipotassium salt dehydrate (EDTA-2K•4H_2O, 99%), $Mn(CH_3COO)_2$•4H_2O (99%), $K_4Fe(CN)_6$•3H_2O (99%), polyvinylidene difluoride (PVDF, 99%), and carboxymethyl cellulose sodium (CMC-Na, 99%) were purchased from Shanghai Aladdin Bio-Chem Technology Co., Ltd. N-methyl-2-pyrrolidinone (NMP, ≥99%) and 1,1,2,2-tetrafluoroethyl 2,2,2-trifluoroethyl ether (HFE, ≥99%) were acquired from Beijing InnoChem Science&Technology Co., Ltd. Triethyl phosphate (TEP, ≥99%), potassium bis(trifluoromethylsulfonyl)imide (KTFSI, ≥99.9%), potassium bis(fluorosulfonyl)imide (KFSI, ≥99.9%), and Ketjien black were purchased from Duoduo Chemical Technology Co., Ltd. Graphite was purchased from Chengdu Jiacai Technology Co., Ltd.

Synthesis of $K_2Mn[Fe(CN)_6]$

The $K_2Mn[Fe(CN)_6]$ (KMF) sample was obtained by a simple precipitation method previously reported by our group.[1] Typically, 50 mL of 0.04 M $Mn(CH_3COO)_2$•4H_2O aqueous solution containing 0.04 M EDTA-2K•4H_2O was dropwise added into 50 mL of 0.04 M $K_4Fe(CN)_6$•3H_2O aqueous solution by the peristaltic pump in ten minutes with continuous magnetic stirring and N_2 bubbling. After aging for 4 h without stirring, the resulting precipitates (yield: 86%) were collected by centrifugation, subsequently washed twice with deionized water followed by an additional wash with ethanol, and finally dried under vacuum at 80 °C for 12 h.

Synthesis of the chemically overpotassiated KMF electrodes

The chemically overpotassiated KMF electrodes were synthesized by reacting pristine KMF electrodes with potassium-naphthalene solution. All operations were performed inside an Ar-filled glovebox (with O_2 and H_2O<0.1 ppm). To prepare potassium-naphthalene solutions, potassium metal was added to a 0.1 M solution of naphthalene in anhydrous diglyme (5 mol of metal per 1 mol of naphthalene). The mixture was

stirred for 2 h, after which the remaining potassium metals were taken out from the resulting dark-green solutions. The KMF electrode was prepared by spreading the slurry containing KMF, Ketjien black, and polyvinylidene fluoride (PVDF) (weight ratio: 7:2:1) onto the Al foil (18 μm, Canrd Technology Co. Ltd.). The chemically overpotassiated KMF electrodes were synthesized in an Ar-filled glovebox. KMF electrodes, which were circles with d=11 mm with KMF an area loading of 2 mg cm^{-2}, were immersed in the potassium-naphthalene solutions for overnight at room temperature. The volume of the potassium-naphthalene solution was typically 1 mL per one electrode.

Material characterizations

X-ray diffraction (XRD) data for the KMF powder and electrodes were collected by the Shimadzu Xlab 6000 X-ray diffractometer with Cu Kα X-ray radiation (λ=1.54184 Å) and the scanning rate was 2° per minute in the range of 10°-80°. The *in-situ* XRD patterns were obtained using a Benchtop X-ray Powder Diffraction (Bruker, D2 Phaser) with Cu Kα radiation (λ=1.54184 Å). The working electrodes were prepared by spreading the slurry containing KMF, Ketjien black, and polyvinylidene fluoride (PVDF) (weight ratio: 7:2:1) onto the Al foil (18 μm, Canrd Technology Co. Ltd.). The *in-situ* cell used a Be film as the X-ray window. Meanwhile, a glass microfiber filter (grade GF/D, Whatman, USA) was used as the separator, a KMF electrode (with an area loading of 3 mg cm^{-2}) was used as the working electrode, potassium metal was used to as the reference and counter electrode, and 0.5 M KTFSI and 0.5 M KFSI dissolved in a mixture of TEP:HFE (1:1 vol.%) was used as the electrolyte. The patterns were collected in the range of 20°-60° under a scanning rate of 2° per minute. The *in-situ* cell was first discharged to 50 mAh g^{-1} (based on the mass of KMF), then charged to 4.4 V (*vs.* K^+/K), and finally discharged to 2.7 V (*vs.* K^+/K) at a current rate of 0.1C (1C=150 mA g^{-1}).

The contents of K, Mn and Fe were determined by inductively coupled plasma emission spectrometry (ICP-OES; ICPE-9800, Shimadzu, Japan). The sample for the ICP tests was prepared by dissolving the KMF sample in the aqua regia.

The conductivity of electrolytes was gauged by using a DDS-307A conductivity spectroscopy at room temperature and before the tests, 2 mL electrolyte was kept at 25 ˚C for 6 h to reach the thermal equilibrium. For each sample, three tests were run in parallel to minimize the statistic error and the average values of the three tests were plotted.

The viscosity of electrolytes was gauged by an Anton Paar MCR-302 rotary rheometer, with a heating rate of 3 ˚C min^{-1}, within the temperature ranging from -20 to 40 ˚C.

The morphology of the samples was captured using transmission electron microscope (TEM, HT7700, Hitachi). High-angle annular dark-field (HAADF) scanning TEM (STEM) measurements were performed on a Thermo Fisher Themis Z equipped with a probecorrector (S-CORR) at 300 kV. The element distribution was determined by drift-corrected mapping *via* energy-dispersive X-ray spectroscopy (EDS) utilizing a Thermo Fisher Super-X detector. Cryogenic transmission electron microscopy (cryo-TEM) characterizations were carried out using a JEOL JEM-F200 microscope under cryogenic temperatures (-180 °C) at 200 kV. The cycled KMF and graphite powder samples were scraped from the cycled KMF and graphite electrodes, rinsed with TEP, and loaded on the TEM grids. Then, the grid was transferred into the cryo-holder (Fischione 2550) in an Ar-filled glove box. Using a sealed container, the cryo-holder was quickly inserted into a JEOL JEM-F200 microscope. Liquid nitrogen was poured into the cryo-holder, and the sample temperature dropped and stabilized at about -180 °C. The lattice spacings of KMF, graphite, and other inorganic species were measured by Digital Micrograph (DM, Gatan) software. The KMF and graphite electrodes were collected after the KMF-graphite cell was overdischarged to 50 mAh $g^{-1}_{\text{-KMF}}$ and after 100 cycles.

X-ray photoelectron spectroscopy (XPS) characterizations were carried out using a Thermo Scientific K-Alpha (USA) equipped with Al Kα (*hv*=1486.6 eV) X-ray radiation. The graphite electrodes were collected after the KMF-graphite cell was overdischarged to 50 mAh $g^{-1}_{\text{-KMF}}$ and after 300 cycles. The samples were fed into the

analytical chamber with a sample chamber pressure of less than 2.0×10^{-7} mbar. The spot size of the analysis chamber was 400 μm, the operating voltage was 12 kV, and the filament current was 6 mA. The full-spectrum was collected with a step of 1 eV, and the high-resolution scans for specific elements were obtained with a step of 0.1 eV. All peaks were calibrated by referencing the binding energy of C 1*s* to 284.6 eV.

The Fe and Mn *K*-edge X-ray absorption near edge structure (XANES) and the extended X-ray absorption fine structure (EXAFS) were investigated in the National Synchrotron Radiation Laboratory (NSRL, Hefei, China). References, such as Fe and Mn foils, were used to calibrate the beamline energy. Fluorescence detection was performed using a 7-element Si drift detector for samples and the total electron yield was used for measurement of samples with high concentration, such as references. The soft X-ray absorption spectroscopy (sXAS) under total electron yield (TEY) mode measurement was performed in the National Synchrotron Radiation Laboratory (NSRL, Hefei, China). The beamline was connected to a bending magnet and covers photon energies from 100 to 1,000 eV with a resolving power (E/ΔE) better than 1,000 and the photon flux is 1×109 photons per second. The data were extracted, and the profiles were fitted according to Athena and Artemis codes. Firstly, the EXAFS spectra were obtained by subtracting the post-edge background from the overall absorption and then normalizing with respect to the edge-jump step. Subsequently, χ(k) data in the *k*-space were Fourier transformed to real (*R*) space using a Hanning windows (d*k*=1.0 $Å^{-1}$) to separate the EXAFS contributions from different coordination shells. To obtain the quantitative structural parameters around central atoms, least-squares curve parameter fitting was performed using the ARTEMIS module of IFEFFIT software packages. The following EXAFS equation was used:

$$\chi(\mathrm{k}) = \sum_j \frac{N_j S_0^2 F_j(k)}{kR_j^2} \exp\left(-2k^2\sigma_j^2\right) \exp\left[\frac{-2R_j}{\lambda(k)}\right] \sin\left[2kR_j + \phi_j(k)\right] S_0^2$$

S_0^2 was the amplitude reduction factor, $F_j(k)$ was the effective curved-wave backscattering amplitude, N_j was the number of neighbors in the j^{th} atomic shell, R_j was the distance between the X-ray absorbing central atom and the atoms in the j^{th}

atomic shell (backscatterer), λ was the mean free path in Å, $\phi_j(k)$ was the phase shift (including the phase shift for each shell and the total central atom phase shift), and σ_j was the Debye-Waller parameter of the j^{th} atomic shell (variation of distances around the average R_j). The functions $F_j(k)$, λ, and $\phi_j(k)$ were calculated with the ab initio code FEFF8.2. The coordination numbers of reference samples were fixed as the nominal values. The obtained S_0^2 was fixed in the subsequent fitting of Mn and Fe species, respectively (S_0^2=0.97 for Mn species and S_0^2=0.76 for Fe species). While the internal atomic distances R, Debye-Waller factor σ^2, and the edge-energy shift ΔE_0 were allowed to run freely. In the fitting process, σ^2<0.01, $|\Delta E_0|$<15 eV, R factor<0.02, where error bounds that characterize the structural parameters obtained by EXAFS spectroscopy were estimated as *CN*±20%, *R*±1%, σ^2±20%. To further investigate the first-shell backscattering atoms and detect light and heavy scatters, wavelet transform (WT) analysis was employed using the Igor pro script developed by Funke *et al*.[2] The details of the theory and application in EXAFS analysis were reported by Muñoz *et al*.[3] This qualitative analysis was primarily focused on the nature of the backscattering atoms as well as the bond lengths owing to the fine resolution in both wavenumbers *k* and radial distribution function *R*, and complemented the limitation of FT analysis. A Morlet wavelet was chosen as the basis mother wavelet.

All retrieved electrodes for the characterizations were obtained by disassembling the cells in the glove box (with O_2 and H_2O<0.1 ppm), where they were washed with dry triethyl phosphate (TEP) to remove the residue electrolyte salts, and subsequently dried in the glove box for 24 hours. To prevent exposure to air during sample transfer, all samples were hermetically sealed in glass bottles.

ToF-SIMS was conducted in the Analysis & Testing Center of Beihang University (Beijing, China). The graphite sample was directly transferred from the glove box to the ToF-SIMS vacuum chamber by a special transfer vessel without being exposed to air. Sputter etching was conducted using an Ar^+ beam (3 kV 100 nA) to obtain the desired depth profile. The area of analysis was 50 × 50 μm^2. The test used a Cs^+ beam (1 keV 60 nA) with a sputter area of 200 × 200 μm and a sputter rate of 0.84 nm s^{-1},

and the sputter time was set to 1000 s. ToF-SIMS data were plotted as 3D heat maps by the Surface Lab 7 software.

Differential electrochemical mass spectrometry (DEMS) was carried out to investigate the gassing behavior of the graphite electrode. The cells were assembled from a 30 mm diameter graphite electrode (~3 mg cm^{-2} areal loading) with a 4 mm hole in the center, a 40 mm GF/D glass microfiber separator, a 32 mm diameter K metal anode, and 700 µL electrolyte in a custom cell housing. The cell was first charged to 90 mAh g^{-1} (based on the mass of graphite), then discharged to 0.01 V, and then charged to 2.0 V (*vs.* K^+/K at a current rate of 0.1C, 1C=279 mAh g^{-1}), while a constant stream of He carrier gas (purity 6.0, 2.5 mL min^{-1}) was passed through. The resulting gas mixture was analyzed using a mass spectrometer (Omni Star GSD 320, Pfeiffer Vacuum GmbH).

Electrochemical measurements

The KMF cathode was fabricated by spreading the slurry containing KMF, Ketjien black, and polyvinylidene fluoride (PVDF) (weight ratio: 7:2:1) dissolved in NMP onto the Al foil (18 µm, Canrd Technology Co. Ltd.). The graphite anode was fabricated by spreading the aqueous slurry of graphite, Ketjien black, and carboxymethyl cellulose (weight ratio: 8:1:1) onto the Al foil (18 µm, Canrd Technology Co. Ltd.). The working electrodes were dried under vacuum at 80 °C overnight. For the potassium electrode preparation protocol, we referred to the method proposed by Pasta *et al.*[4] Potassium electrodes were prepared from potassium chunks in mineral oil (98% trace metals basis, Sigma Aldrich). First the K chunks were removed and melted in a beaker inside a Muffle furnace (Lindberg/Blue M™ Moldatherm™, Thermo Fisher Scientific Co. Ltd.) in an Ar-filled glovebox (with O_2 and H_2O<0.1 ppm). A spatula was then used to skim off and remove the visible impurity layers until the liquid K metal appeared clean. Then, the liquid K metal was quenched into clean mineral oil forming spheres of clean K. These K spheres were then cleaned with hexane (95% anhydrous, Sigma Aldrich). Just before use, the K was rolled to ~ 0.5 mm thickness using an aluminum rolling pin with the K sandwiched between two sheets of weighing paper coated in hexane and one

metal surface was gently polished using a plastic blade to remove any oxide and provide a sticking surface. Electrodes were then punched into discs of 14 mm using a wad punch. The K electrode was placed on the current collector (stainless steel) with the polished surface down. Next, for the active and exposed K surface, first the K was polished with the microtome blade. The microtome blade was used to form a mirror-like finish, resulting in an improved polished K surface free of surface irregularities. The active K metal surface was polished at the very end of cell setup, just before electrolyte addition. So, the polished surface was exposed to the glovebox environment for minimal time before the electrolyte was added. For the KMF-K cells and graphite-K cells, the loading mass of the KMF and graphite on the electrode was approximately 2 mg cm^{-2}. To construct the full-cell, the cathode-to-anode mass ratio of the full-cell was set to be 1.82:1. Unless otherwise stated, the calculation of the specific capacities for both metallic potassium cells and full-cells was based on the mass of KMF in the cells. The calculation of the specific energy for the full-cells was based on the total mass of KMF and graphite in the cells. The specific energy of the cells was calculated by integration of voltage with the specific capacity which was automatically done by the Land battery testing system. The average discharge voltage was obtained by dividing the specific energy by the specific capacity. To ensure the repeatability of battery performance, we tested the performance of coin type cells at four current densities respectively. The coin-type cells were assembled using CR-2032 type coin cells (spacer, 0.5 mm; spring, 1.8 mm) in an Ar-filled glovebox with both oxygen and moisture contents below 0.1 ppm. Potassium-metal half-cells were assembled with the prepared working electrodes and potassium metal foil separated by a glass microfiber filter (grade GF/D, Whatman, USA) soaked with the electrolyte of 0.5 M KTFSI and 0.5 M KFSI dissolved in a mixture of TEP:HFE (1:1 vol.%). All coin cells were filled with about 100 μL electrolyte to ensure the wetting of cell components, and then were left at open-circuit condition for 24 h before any electrochemical tests. All coin cells were disassembled, vented, replenished with electrolyte, and reassembled in the glove box after overdischarge. Galvanostatic charge-discharge tests were carried out by using the Land battery testing system

(CT2001A, Wuhan, China) and the Neware battery test system (CT-4008T, Shenzhen, China) in the voltage range of 0.01-2.0 V (vs. K^+/K) for the graphite-K cells, 2.7-4.4 V for the KMF-K cells, and 1.5-4.3 V for the KMF-graphite full-cells. For the overdischarge or overcharge experiment, the specific capacity was used as the cutoff condition (based on the mass of KMF or graphite of the corresponding cells), and the subsequent charge and discharge process was maintained. The three-electrode experiments were performed using the Swagelok cell. It consisted of three electrodes, two directly opposite electrodes and one electrode perpendicular to the junction of the first two electrodes. Wherein, the KMF electrode and the graphite electrode were respectively placed at the opposite two electrodes, and the middle was separated by a glass microfiber filter (grade GF/D, Whatman, USA). A potassium metal sheet (14 mm in diameter, Changgao New Materials Co., Ltd) was placed at the vertical electrode and a glass microfiber filter (grade GF/D, Whatman, USA) was used to separate the K metal from the lower electrode. Two opposite electrodes were used to test the KMF-graphite cell, and the graphite side electrode and the vertical electrode were used to monitor the potential of the graphite relative to the K metal. The three-electrode experimental data were based on three measurements to ensure the accuracy of the calculation. The dimensions of the electrodes in the pouch-type full-cell were 5 cm in length and 4.5 cm in width. To ensure the scalability of the battery, we assembled two different pouch-type full-cells respectively for testing. The mass loadings of KMF and graphite in the pouch-type full-cell-1 shown in Fig. 4f were 3.00 and 1.65 mg cm^{-2}, respectively. The mass loadings of KMF and graphite in the pouch-type full-cell-2 shown in Fig. S38 were 4.89 and 2.63 mg cm^{-2}, respectively. To ensure sufficient wetting of the separator, 1 mL and 1.5 mL of the electrolyte were added to the pouch-type full-cell-1 and pouch-type full-cell-2, respectively. The mass loadings of KMF and graphite in the large-capacity pouch-type full-cell shown in Supplementary Fig. 39 were 8.50 and 4.65 mg cm^{-2}, respectively. The cells were assembled in a winding configuration and were filled with 15 mL of the electrolyte. The air pocket is left on the side of the pouch-type full-cells to collect the gas produced during the overdischarge and formation of the cells.

For the long-term cycling stability tests, the pouch-type KMF-graphite full-cell was firstly overdischarged at 0.05C and then cycled for 1 time between 1.0 and 4.3 V at 0.05C. Subsequently, the pouch-type full cells were cut open and degassed in an Ar-filled glovebox. Each of the three cells was then refilled with electrolyte at volumes of 200 μL, 300 μL, and 2.0 mL, respectively, and resealed after formation. Before the long-term cycling stability tests, the pouch-type KMF-graphite full-cell was activated 3 times between 1.0 and 4.3 V at 0.1C and then cycled between 1.0 and 4.3 V at 0.5C.

Calculation methods

The study employed the Vienna ab initio Simulation Package (VASP) based on density functional theory (DFT) to conduct comprehensive calculations. In our investigations, we utilized the projector-augmented wave potential to model interactions between ion cores and valence electrons. To ensure precision, we set the cutoff energy at 500 eV for the expansion of the valence electron wave function, with a convergence force criterion of 0.01 eV $Å^{-1}$.

For determining lattice parameters and formation energies, we turned to the HSE06 hybrid functional. The Monkhorst-Pack method was used to sample the Brillouin zone, with a k-point mesh of 3×3×3, both for DFT+U and HSE06 calculations. The preference for HSE06 over GGA+U was based on its broader applicability and enhanced accuracy. However, we observed that GGA+U, with specific U_{eff} values (4.3 eV for Fe and 5.0 eV for Mn, as previously developed for olivine $LiFePO_4$ and $LiMnPO_4$), produced reliable geometries and calculated voltages in line with experimental data.

In our investigations, two levels of exchange-correlation energy theory were implemented. Initially, we utilized the general gradient approximation with the PW91 functional, including an on-site Hubbard U term (GGA+U) on transition metal d orbitals for structural optimization. This approach was essential to mitigate issues related to artificial delocalization of electronic states, particularly the 3*d* electrons on the metal centers, which arise due to the self-interaction error inherent in pure DFT. To further analyze the electronic structure and bonding characteristics, we performed

Crystal Orbital Hamilton Population (COHP) calculations using the LOBSTER package.[5]

Our research considered various framework types of $K_nMnFe(CN)_6$, encompassing different magnetic moment configurations. To gain insights into the system's behavior, we calculated an approximate voltage profile based on the ground state DFT energies. This profile was derived from the following formula:

$$V = -\frac{E(K_{x1}MnFe(CN)_6) - E(K_{x2}MnFe(CN)_6) - (x_2 - x_1)E(K)}{x_2 - x_1}$$

In this formula, $E(K_xMnFe(CN)_6)$ represents the DFT energies of the most stable $K_xMnFe(CN)_6$ configurations at each composition, and $E(K)$ signifies the energy of bcc K metal (space group: *Im–3m*).

To gain deeper insight into the electronic structure and orbital hybridization, we performed projected density of states (PDOS) calculations. The PDOS was obtained by projecting wavefunctions onto atomic orbitals, allowing us to resolve the contributions of Mn and Fe *d* orbitals, as well as C and N *p* orbitals, in the formation of bonding and antibonding states. This analysis provided critical insights into *d-p* hybridization and its influence on the electronic properties of $K_xMnFe(CN)_6$.

All the classic molecular dynamic (cMD) simulations conducted in this work were performed using the Large-scale Atomic/Molecular Massively Parallel Simulator (LAMMPS, http://lammps.sandia.gov) package.[6] All-atom optimized potentials for liquid simulations (OPLS-AA) force-field with the K^+, FSI^-, and $TFSI^-$ anions description from previous publications,[7-9] while the force-field of TEP and HFE was obtained from the LigParGen.[10] The electrolyte systems were set up initially with the salt and solvent molecules distributed in the simulation boxes using Packmol[11] and Moltemplate (http://www.moltemplate.org/).[12] For each system, an initial energy minimization at 0 K (energy and force tolerances of 10−5) was performed to obtain the ground-state structure. After this, the system was heated from 0 K to room temperature (300 K) at constant volume over 0.2 ns using a Langevin thermostat, with a damping parameter of 100 ps. The system was equilibrated in the constant temperature (300 K) and constant pressure (1 bar) (NPT ensemble) for 10 ns. Finally, a MD run in the NVT

ensemble was performed for 5 ns for equilibrium, and a following 5 ns NVT simulation was used for analysis. The visualizations were made by using VESTA,[13] VMD,[14] and OVITO software.[15]

The classical MD simulations were performed by using LAMMPS at constant volume and temperature (NVT) to the electrolyte-electrode interface with two three-layer C electrodes in an FCC lattice sandwiching the $54 \times 54 \times 63$ $Å^3$ electrolyte. A vacuum layer of 50 Å in the z direction is set to ensure no interactions between the periodic electrode sheets in an adjacent cell. A surface charge was applied by placing a partial charge on the first layer of C atoms, the surface charge was set to be 0, ± 5 $\mu C/cm^2$, and ± 10 $\mu C/cm^2$, respectively. Equilibration was performed at a 1 fs time step for 5 ns at 300 K, followed by 5 ns simulation for data collection.

Supplementary notes

Note S1.

Transmission electron microscopy (TEM) images indicate an average particle size of approximately 200 nm of the as-synthesized KMF samples (Figs. S1a-b). The selected area electron diffraction (SAED) (Fig. S1c) showcases sharp diffraction spots with the monoclinic structure. High-resolution TEM (HRTEM) imaging (Fig. S1d) further identifies lattice fringes with an interplane spacing of 0.357 nm, matching well with the *d*-spacings of the (220) planes of monoclinic $K_2Mn[Fe(CN)_6]$. Moreover, elemental energy dispersive X-ray spectroscopy (EDS) analysis (Fig. S1e) demonstrates a uniform distribution of K, Mn, and Fe within the synthesized material.

Fig. S2a shows the powder X-ray diffraction (XRD) pattern of pristine KMF along with its Rietveld refinement results, which suggest a monoclinic phase with space group *P21/n* and lattice parameters of a=10.075675 Å, b=7.301648 Å, c=6.932913 Å, and β=90.246°. The crystalline structure retrieved from the Rietveld refinement is schematically illustrated in Fig. S2b, showing a typical open framework structure with the N-coordinated Mn cations and C-coordinated Fe cations.[16] The detailed atomic positions extracted from the Rietveld refinement are provided in Table S1.

Note S2.

The electrolyte utilized in this study is a localized high-concentration electrolyte consisting of 0.5 M KFSI and 0.5 M KTFSI dissolved in a mixture of triethyl phosphate (TEP) and 1,1,2,2-tetrafluoroethyl 2,2,2-trifluoroethyl ether (HFE) in a 1:1 volume ratio. TEP is selected as the primary solvent due to its nonflammability, commercial maturity, and cost-effectiveness. HFE is introduced to reduce the viscosity of the electrolyte (Fig. S4a). KFSI is chosen for its high dissociation degree, while KTFSI is selected for its ability to passivate aluminum foil in the TEP-based electrolytes.[17] The ratio of KFSI to KTFSI salts is determined by optimizing the electrolyte conductivity (Fig. S4b). Before the electrochemical evaluation of KMF, the stability of the electrolyte used in this study is examined using linear scanning voltammetry (LSV) tests with the K-Al cell, as shown in Figs. S4c-d. The LSV result reveals that the electrolyte exhibits negligibly low oxidation current between 3-4.5 V (*vs.* K^+/K), indicating that KMF can be stably cycled between 2.7 and 4.4 V (*vs.* K^+/K) in a potassium metal half-cell with the present electrolyte. Additionally, as shown in Fig. S4d, during the first reduction scan, the reduction current density at 1.2 V (*vs.* K^+/K) is only ~0.2 μA cm^{-2}, indicating that the overpotassiation platform observed in Fig. S5 is generated by K-ion insertion in the KMF lattice rather than by electrolyte decomposition.

Note S3.

To evaluate the feasibility of increasing K-ion content in KMF through electrochemical means, a series of overdischarge experiments, also known as overpotassiation, are conducted on KMF. Specifically, after assembling the KMF-K metal cells, they undergo initial overdischarge (overpotassiation) to specific capacities of 30, 50, 70, 90, 120, or 150 mAh g^{-1} (based on the mass of KMF in the cells). The resulting KMFs in these cells, termed overpotassiated KMF, are denoted as KMF-*n* in subsequent discussions, with "*n*" representing the specific capacity during the overpotassiation process. As illustrated in Fig. S5, the overdischarge process reveals a distinct potential plateau at 1.2 V (*vs.* K^+/K). Subsequent charge exhibits potential profiles characterized by a sloped curve from 1.2 to 3.5 V, followed by a shoulder from 3.5 to 4.0 V, and ultimately a long and flat plateau until the cutoff potential of 4.4 V. The specific capacities during the first charge (depotassiation) are nearly proportional to the preceding overdischarge (overpotassiation) capacities, suggesting that the excess K-ions introduced during overdischarge can be electrochemically extracted from KMF. Following the initial overdischarge and charge processes, the cells undergo discharge and charge within the typical potential range of 2.7-4.4 V (*vs.* K^+/K), exhibiting charge-discharge potential profiles similar to those of KMF subjected to a normal charge-discharge process (Fig. S3a).

The cycling performance of various overpotassiated KMFs is illustrated in Fig. S6. After 150 cycles, with the exception of KMF-150, which experiences over a 20% loss in capacity, all other overpotassiated KMFs demonstrate stable cycling performance, retaining over 90% of their capacity. This suggests that embedding certain amounts of K-ions into KMF through electrochemical overpotassiation does not adversely affect the charge-discharge reversibility and cycling stability of KMF. The lower capacity retention observed in KMF-150 may be attributed to the irreversible structural changes caused by excessive overpotassiation.

To explore the limits of overpotassiation, KMF is overdischarged to 0.05 V (*vs.* K^+/K). After this extreme overdischarge experiment, KMF exhibits very poor cycling

stability, indicating that excessive overpotassiation may lead to the collapse of the KMF crystal structure, resulting in rapid capacity decay (Fig. S7).

Note S4.

The refined results, with detailed atomic positions listed in Table S2, illustrate that KMF-50 also possesses a monoclinic crystal structure (space group *P21/n* with lattice parameters *a*=10.063584 Å, *b*=7.291874 Å, *c*=6.924734 Å, and β=90.283). The corresponding crystal structure, depicted in Fig. S9b, unveils a distorted open framework with some extra K embedded within this framework.

Note S5.

The TEM images (Figs. S10a-b) of KMF-50 reveal cubic morphology with distinct edges, while the corresponding selected area electron diffraction (SAED) pattern (Fig. S10c) exhibits sharp diffraction patterns reminiscent of those observed for pristine KMF. The HRTEM image of KMF-50 (Fig. S10d) reveals lattice fringes with an interplane spacing of 0.506 nm, closely matching the *d*-spacing of the (020) crystal plane of pristine KMF. Additionally, EDS elemental mapping (Fig. S10e) illustrates the uniform distribution of K, Mn, and Fe in the sample. Overall, TEM characterizations indicate that the structural integrity of KMF is preserved after overpotassiation to KMF-50.

Note S6.

Detailed atomic structure information is obtained through extended X-ray absorption fine structure (EXAFS) analyses, as illustrated in Figs. S12-15. The k^3-weighted EXAFS spectra and corresponding Fourier Transforms (FTs) at Fe and Mn *K*-edge are presented in Figs. S12 and S14 for various samples. From the fitting results (Tables S4-5), notable structural changes in the Fe and Mn coordination environments within KMF across different states are discerned. In the pristine KMF, MnN_6 octahedra featuring a Mn-N distance of 2.19 Å and FeC_6 octahedra with a Fe-C distance of 1.84 Å are identified (Tables S4-5). Following the overpotassiation process to KMF-50, the Mn-N bond contracts to ~2.16 Å (Table S4), indicating an approximate 1.37% decrease compared to pristine KMF. As the overpotassiation process continues, the Mn-N bond further shrinks to ~2.15 Å in KMF-150, which is about 1.83% less than that in the original KMF. This contraction is attributed to the elastic deformation of the cyanide framework induced by extra K insertion. Subsequently, upon complete charging, the Mn-N bond contracts further to ~1.97 Å, marking an approximate 10% decrease compared to that in the pristine KMF, consistent with previously reported findings.[18] In contrast, the Fe-C bond undergoes a slight change to 1.85 Å after the overpotassiation process to KMF-50, exhibiting a slight stretch compared to that in the pristine state (Table S5). When the overpotassiation process continues to reach KMF-150, the Fe-C bond continues to stretch, reaching 1.86 Å. Upon full charging, the Fe-C bond further extends to ~1.89 Å, representing an increase of about 2.7% compared to that in the pristine state. In sharp contrast with above samples, for the extremely overpotassiated KMF-0.05 V sample, Fe-Fe bond (2.47 Å) and Mn-Mn bond (2.69 Å) are identified, indicating the reduction of Mn(II) and Fe(II) to Mn(0) and Fe(0), respectively, and the collapse of the KMF crystalline structure.

Note S7.

The utilization of WT analysis allows for a 2D visual representation of the data, offering detailed insights into the local atomic structure. This approach provides information that is challenging to discern through traditional one-dimensional decomposition methods like Fourier Transform EXAFS.[3, 19] The color intensity in the Figs. S16-17 corresponds to the WT modulus associated with the decomposition of the EXAFS amplitude term. Fig. S16 presents the WT analysis of Fe *K*-edge EXAFS throughout the overpotassiation, charge, and discharge processes. For the pristine KMF, the peak intensity occurs around ~4.4 Å^{-1} in *k*-space ($r \approx 1.4$ Å) for the Fe *K*-edge, indicating the Fe-C bond, which exhibits minimal change in KMF-50. Further overpotassiation to KMF-150, the peak of Fe-C changes to ~4.3 Å^{-1} in *k*-space ($r \approx 1.5$ Å), reflecting a slight increase in the length of the Fe-C bond. Upon full charging, the peak intensity of Fe-C shifts to ~4.2 Å^{-1} ($r \approx 1.7$ Å), reflecting an increase in the average length of the Fe-C bond. Subsequent discharging to 2.7 V restores the peak intensity of Fe-C to its initial state in the pristine KMF.[20, 21] Higher-order shells are additionally observed at $k \approx 3.75$ Å^{-1} and $k \approx 4.95$ Å^{-1} yet their interpretation is likely linked to multiple scattering effects involving the combined transition metal (Mn). This inference arises from the ambiguous appearance of the WT modulus.[22] Regarding the Mn *K*-edge EXAFS WT analyses Fig. S17), the results reveal that the highest intensity for Mn-N is located at ~4.7 Å^{-1} in *k*-space (corresponding to $r \approx 1.9$ Å) for pristine KMF. Following overpotassiation, this intensity shifts to ~4.6 Å^{-1} ($r \approx 1.6$ Å) in KMF-50 and ~4.55 Å^{-1} ($r \approx 1.6$ Å) in KMF-150, further reducing to ~4.4 Å^{-1} ($r \approx 1.5$ Å) after subsequent full charging, and finally returning to ~4.9 Å^{-1} ($r \approx 1.9$ Å) after discharging to 2.7 V. This observation vividly illustrates a continuous shortening of the average Mn-N bond length throughout the overdischarge-charge process.[23] It is worth noting that completely different phenomena are observed in the WT analyses of KMF-0.05 V, namely Fe-Fe peak at ~7.8 Å^{-1} in *k*-space ($r \approx 2.25$ Å) and Mn-Mn peak at ~6 Å^{-1} in *k*-space ($r \approx 2.3$ Å). This observation provides further evidence that extreme overdischarge causes Mn(II) and Fe(II) to be reduced to Mn(0) and Fe(0), respectively.

Note S8.

The corresponding structure parameters obtained during the theoretical calculations are given in Table S6. Based on the calculations upon the transition from KMF to $K_{2.5}$MF-3, a reduction of unit cell volume from 539.68 $Å^3$ to 527.05 $Å^3$ is expected, consistent with the XRD results. With the further embedding of K-ions, the crystal volume gradually increases until 589.83 $Å^3$ of K_4MF-1. Here, we simply quantify this trend in terms of the defined σ (detailed calculation is listed in the notes to Table S6), which is used to represent the degree of inclination of the cell unit, or the degree of deviation from the cubic lattice. The smaller the σ value, the greater the degree of tilt or deviation, that is, the greater the degree of contraction of the C≡N bond in the KMF lattice toward the interior of the crystal. When the additional K^+ is embedded into KMF, the entire crystal structure shrinks, and with the increase of K^+ embedding, more K^+ enters the KMF lattice, causing the contracted lattice to expand further, so that its crystal volume increases.

Note S9.

After the initial overdischarge of the $K_2Mn[Fe(CN)_6]$ (KMF)-graphite cell, $K_2Mn[Fe(CN)_6]$ is converted into $K_{2+x}Mn[Fe(CN)_6]$ ($K_{2+x}MF$). The reversible capacity of graphite after overdischarge is 270 mAh g^{-1}, and the Coulombic efficiency (CE) of the first cycle after overdischarge is 75±4% (see Fig. S29 for details). The influence of the overpotassiation degree x of $K_{2+x}MF$ on the specific energy of the $K_{2+x}MF$ -graphite cell is roughly estimated as follows.

Assuming that a $K_{2+x}MF$-graphite cell with a total capacity of 1 Ah is fabricated, the graphite mass is calculated to be:

$$m_{graphite} = \frac{1000\ (mAh)}{270\ (mAh\ g^{-1})} = 3.703\ (g)$$

Assuming that all K-ions in the $K_{2+x}MF$ can be extracted, the theoretical specific capacity ($Q_{K_{2+x}MF}$)provided by $K_{2+x}Mn[Fe(CN)_6]$ after complete depotassiation is calculated as follows:

$$Q_{K_{2+x}MF} = \frac{26800\ (mAh\ mol^{-1}) \times (2+x)}{(345.09 + 39 \times x)\ (g\ mol^{-1})}$$

The average discharge voltage of the $K_2Mn[Fe(CN)_6]$-graphite cell is measured to be 3.6 V, and x additional K-ions are embedded in $K_2Mn[Fe(CN)_6]$ during the overpotassiation process.

For the sake of simplicity, the N/P ratio of the $K_{2+x}MF$-graphite cell is set to be 1. In other words, the capacity provided by the $K_{2+x}MF$ cathode during the initial full depotassiation process is equal to the capacity of the graphite anode during the initial potassiation process, as schematically shown in Fig. S30a. Thus, the actual mass of $K_{2+x}MF$ ($m_{K_{2+x}MF}$) required in the $K_{2+x}MF$-graphite cell is calculated as follows:

$$m_{K_{2+x}MF} = \frac{1000\ (mAh)}{0.75 \times Q_{K_{2+x}MF}\ (mAh\ g^{-1})}$$

The specific energy of the $K_{2+x}Mn[Fe(CN)_6]$-graphite cell is calculated as follows:

$$E_{K_{2+x}Mn[Fe(CN)_6]-graphite\ cell} = \frac{3.6\ (V) \times 1000\ (mAh)}{m_{K_{2+x}MF}\ (g) + m_{graphite}\ (g)}$$

where 3.6 V is the experimentally measured average discharge voltage of the $K_{2+x}Mn[Fe(CN)_6]$-graphite cell.

As shown in Fig. S30b., the maximum specific energy is realized at x=0.74. When x<0.74, the remaining K content in the KMF decreases after the initial charge, as schematically shown in Fig. S30c. Therefore, with the increase of x, the mass of KMF required to fabricate the $K_{2+x}MF$-graphite cell with a total capacity of 1 Ah gradually decreases, and the energy density of $K_{2+x}MF$-graphite cell increases, reaching a peak value at x=0.74. Further increasing the overpotassiation degree beyond this point leads to a decrease of the specific energy. This is because some of the extracted K-ions during depotassiation process, which are stored in the graphite anode, cannot be re-inserted into KMF due to its limited theoretical capacity of 155.3 mAh g^{-1} in the potential range of 2.7-4.4 V (*vs.* K^+/K), as schematically shown in Fig. S30d. Therefore, when x>0.74, the discharge capacity of the $K_{2+x}Mn[Fe(CN)_6]$-graphite cell is less than 1 Ah and the discharge specific energy of the cell is calculated as follows:

$$E_{K_{2+x}Mn[Fe(CN)_6]-graphite\ cell}{}' = \frac{\frac{m_{K_{2+x}MF}\ (g)}{(345.09+39\times x)\ (g\ mol^{-1})}\times 26800\ (mAh\ mol^{-1})\times 2\ (mol)\ \times 3.6\ (V)}{m_{K_{2+x}MF}\ (g)+m_{graphite}\ (g)}$$

Where 26800 is the capacity provided by 1 mol of electrons in terms of mAh, and 2 indicates that maximum 2 mols of electrons can be transferred during the discharge process due to the charge storage limitation of KMF.

It has to be emphasized that due to the oversimplified assumptions, above calculations are very rough estimations. Multiple factors will cause deviation of the calculated results from the real situations, including N/P ratios, electrolyte composition, electrolyte oxidation on the high-voltage KMF side, the incomplete K-ion extraction of $K_{2+x}MF$ depotassiation, and the variation of graphite's Coulombic efficiency after various overdischarge degrees.

Note S10.

Here, we use three-electrode cells, comprising a KMF cathode, a graphite anode, and a K metal reference electrode switched between them, to monitor the potential variation of KMF and graphite during the overdischarge process. As shown in Figs. S41a-f, two cells are tested in parallel. During overdischarge, when the voltage of the KMF-graphite full-cell decreases to -3.5 V (Fig. S41a), the potential of graphite increases to 4.46 V (*vs.* K^+/K) due to electrolyte oxidation (Fig. S41b). Meanwhile, the potential of KMF decreases to 0.96 V (*vs.* K^+/K) (Fig. S41c), enabling additional K-ion insertion into KMF, a phenomenon akin to the results observed in the KMF-K metal half-cells. It is worth noting that large polarization during K plating-stripping and unstable rest potential are found at the K metal electrodes, which may lead to the potential difference between the three- and two-electrode cells.[24] After overdischarge, the KMF-graphite full-cell is charged and discharged within the normal voltage range of 1.5-4.3 V, and the potential of graphite regularly varies between 0.02 V and 2.35 V (*vs.* K^+/K) (Fig. S41b) while that of KMF changes between 3.85 and 4.32 V (*vs.* K^+/K) (Fig. S41c). On the graphite anode side, after initially overdischarging the full-cell, the subsequent Coulombic efficiency of the graphite is 74.04% (Fig. S41b). In the other cell, the Coulombic efficiency of the graphite in the full-cell after the initial overdischarge is 73.11% (Fig. S41e). On the contrary, when the KMF-graphite full battery is charged and discharged directly without initial overdischarge, the first Coulombic efficiency of the graphite is only 65.68% (Fig. S41h), which is on par with the reported results in the literature.[25-27]

Note S11.

During the initial overcharge process of the graphite-K metal cell, the potential of graphite quickly increases to 4.5 V (*vs.* K^+/K) (Fig. S42a), mirroring the results observed in the KMF-graphite full-cell (Figs. S41b and e). It is worth emphasizing that the Al current collector, upon which graphite is loaded, displays a smooth surface morphology without noticeable pits after overcharging the graphite-K metal cell, indicating the absence of Al corrosion (Fig. S43). After the overcharge process, graphite in the K metal half-cell delivers potassiation and depotassiation capacities of 341.2 and 269.6 mAh g^{-1}, respectively, resulting in a CE of 79%, closely aligning with the corresponding CE of graphite obtained in the overdischarged KMF-graphite full-cell. Conversely, when examining the graphite electrode in the K metal half-cell under regular charge-discharge conditions, it exhibits initial potassiation and depotassiation capacities of 404.1 mAh g^{-1} and 269.8 mAh g^{-1}, respectively (Fig. S42a), accompanied by a lower Coulombic efficiency of 66.8%. Moreover, following the initial overcharge process, graphite in the K metal half-cell exhibits stable cycling performance with an average CE exceeding 99.5% (Figs. S42b-c).

Note S12.

Cryogenic transmission electron microscopy (cryo-TEM) is employed to further investigate the detailed microstructural properties of various KMF samples, with the corresponding cryo-TEM images presented in Fig. S45. Following overdischarge, no electrolyte decomposition products are observed on the surface of KMF-50 (Figs. S45a-b), which remains identical to the pristine KMF (Fig. S46). In contrast, the cathode electrolyte interphase (CEI) measuring approximately 4~5 nm formed on the surface of KMF after 100 cycles (Figs. S45c-d), confirming that electrolyte decomposition does not occur during the overdischarge process. Meanwhile, the energy dispersive spectrometry (EDS) mapping, shown in Figs. S47-48, illustrates the elemental distribution of K, Mn, Fe, F, P, S, and O on the surface of the KMF samples. The EDS results reveal that F, P, and S indicative of electrolyte decomposition products are absent on the surface of KMF-50 after overdischarge. In contrast, these elements are uniformly distributed on the surface of KMF after 100 cycles. These findings further confirm that the overdischarge process involves the embedding of K-ions into the KMF lattice, rather than electrolyte decomposition.

Notably, in the full-cell configuration, an overdischarge cutoff of 50 mAh g^{-1} was applied, corresponding to approximately $K_{2.75}MF$. According to the previous analysis (Note S8 and Table S6), the associated lattice-volume change is small and is therefore unlikely to compromise the mechanical stability of the material during prolonged cycling. To further verify this point, scanning electron microscopy (SEM) and transmission electron microscopy (TEM) were performed on KMF electrodes after extended cycling. As shown in Fig. S49, no discernible particle fracture was observed, confirming that the volume change induced by overdischarge does not weaken the mechanical robustness of the material.

Note S13.

To delve deeper into the influence of the initial overdischarge of the full-cell on the SEI formation mechanism on graphite, we employe classical molecular dynamics (cMD) simulations, along with calculations of the radial distribution function (RDF) and cumulative distribution functions (CDF), to visualize the ion distribution at the electrode-electrolyte interface (Figs. S50-51). The calculations reveal that HFE shows minimal accumulation around K^+ throughout the solvation shell while TEP exhibits a strong accumulation and tightly binds to K^+ (Fig. S50), indicating its pivotal role as the primary solvent determining the solvation structure. The solvation structure of the present electrolyte as simulated in MD is depicted in Fig. S51.

The cMD simulations are performed to profile the ion distribution at the electrode-electrolyte interface when charge is applied on the electrode (Figs. 5a-b and Fig. S52). Initially, when no charge is applied to the electrode, neither K-ions (denoted as 'K') nor anions (denoted as 'N') dominate the appearance at the electrode-electrolyte interface (Fig. 5b). However, upon the application of a charge of 5 μC cm^{-2}, K-ions migrate to the negatively charged electrode (left electrode in Fig. 5b and Fig. S52b), while anions accumulate on the positively charged electrode (right electrode in Fig. 5b and Fig. S52b), resulting in the formation of an anion-enriched interface. This effect intensifies notably with a higher charge of 10 μC cm^{-2} (Fig. S52c), leading to an increased probability for anions to appear at the positively charged electrode-electrolyte interface (Fig. 5b and Table S9). As suggested by the MD calculations, during overdischarging the KMF-graphite full-cell, K-ions insert into the negatively charged electrode (*i.e.*, KMF), while anions accumulate and decompose on the positively charged side (*i.e.*, graphite) to maintain electrolyte charge neutrality, subsequently contributing to the SEI formation on graphite.

Note S14.

In the XPS analyses (Fig. S53), the pristine graphite (Gr-P) powder exhibits a distinct signal in the C 1*s* spectrum attributed to the C−C bonds (284.3 eV), originating from graphite. Upon overdischarging the KMF-graphite full-cell, the C 1*s* spectrum reveals three contributions: C−C (284.3 eV), C−O (285.8 eV), and C=O (287.9 eV), indicating electrolyte decomposition on the graphite electrode during the initial overdischarge process (Fig. S53a). Additionally, in the F 1*s* and S 2*p* spectra (Figs. S53b-c), signals corresponding to K-F (684.8 eV), S-F (688.5 eV), and -OSO_2- (169.3 eV) emerge, suggesting the decomposition of anions on the graphite electrode during the initial overdischarge. This phenomenon may explain the increased Coulombic efficiency of graphite after the initial overdischarge, as fluoride compounds often exhibit high electrochemical stability and low electronic conductivity, making them favorable interfacial components in various battery systems.[28-31] The XPS analyses also reveal a P-O signal (134 eV) in the P 2*p* spectrum, originating from the decomposition of TEP solvents (Fig. S53d). Following 300 charge-discharge cycles (Gr-300 cycles) in the overdischarged KMF-graphite cell, the intensity of C−O, C=O, and P-O signals show only a minor increase, indicating minimal solvent decomposition and organic components accumulation on the graphite surface during long-term cycling. However, a notable increase in the intensity of K-F and SO_2F signals is observed, suggesting further anion decomposition contributing to the formation of an inorganic-rich SEI.

Note S15.

To gain insights into the electrolyte oxidative decomposition products, operando differential electrochemical mass spectrometry (DEMS) is employed to monitor the gas generated on the graphite side in the graphite-K metal cells. As illustrated in Fig. S59, CO_2, primarily produced by electrochemical electrolyte oxidation and/or degradation of surface impurities on graphite, exhibits a notable increase when the potential of graphite is initially raised to 4.5 V (*vs.* K^+/K), corresponding to the overdischarge process of the KMF-graphite full-cell. Previous studies have demonstrated that the use of CO_2 as an additive can optimize the performance of graphite by modulating its SEI structure and composition, which subsequently improves the Coulombic efficiency and stability of the battery.[32] In addition to CO_2, a less amount of O_2 is also detected. Following the initial overcharge of the graphite-K metal cell, the escape of CO_2 and O_2 is significantly reduced in subsequent regular charge-discharge cycles. This observation suggests that major electrolyte decomposition occurs during the initial overcharge process.[33] Furthermore, throughout the entire cycle, no flammable H_2 and CH_4 gas emissions are detected.

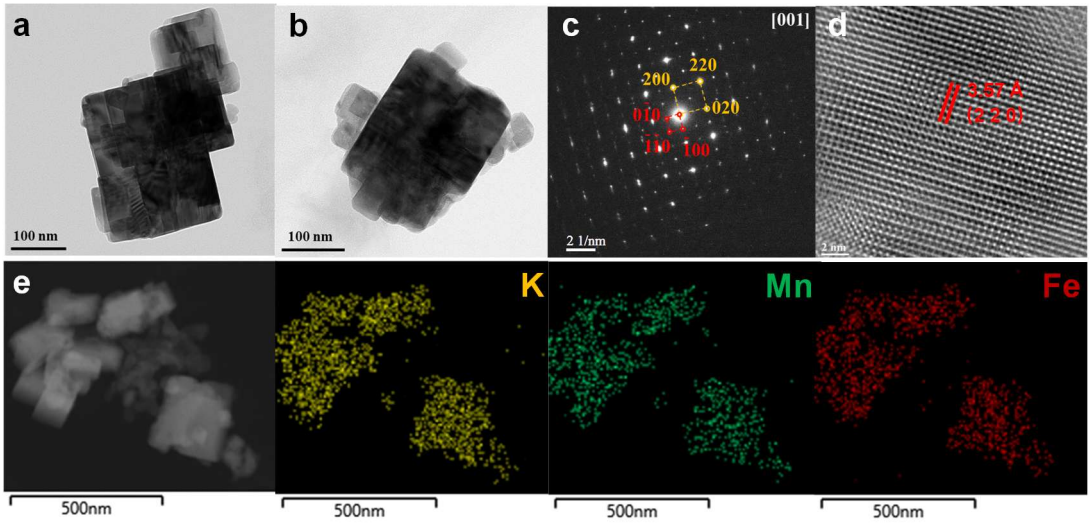

Fig. S1 TEM characterizations of pristine KMF. (a, b) TEM images, (c) SAED pattern, and (d) HRTEM image with the *d*-spacings of (220) of monoclinic KMF marked. (e) TEM image and the corresponding K, Mn, and Fe elemental mapping results.

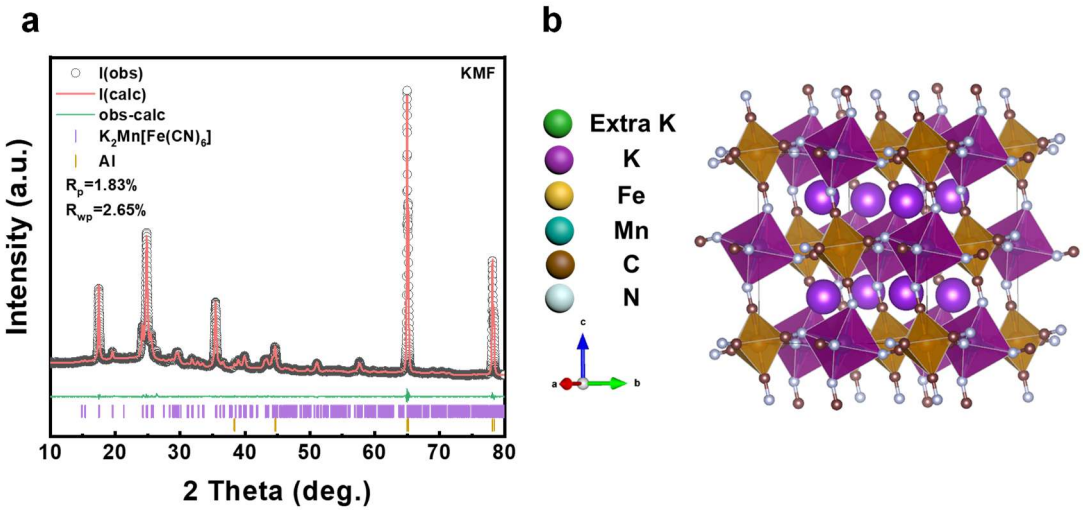

Fig. S2 Crystalline structure characterizations of pristine KMF. (a) XRD patterns and the corresponding Rietveld refinement of pristine KMF. (b) The crystalline structure of KMF retrieved from the Rietveld refinement.

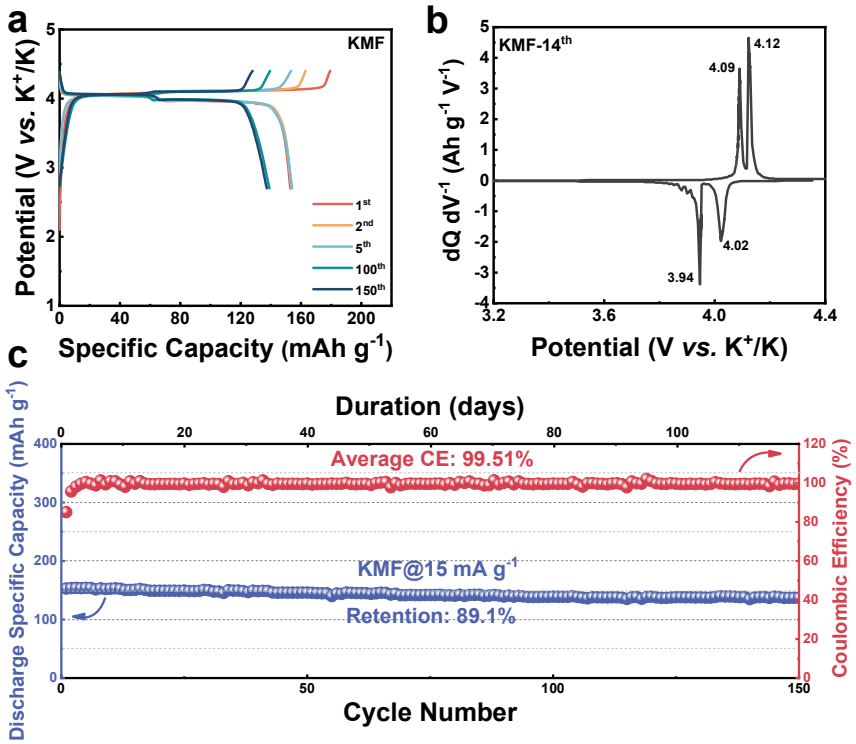

Fig. S3 Electrochemical performance of the KMF-K metal cells. (a) The galvanostatic charge-discharge potential profiles, (b) differential capacity (dQ dV^{-1}) curve of the 14th cycle, and (c) cycling performance of the KMF-K metal cell at 15 mA g^{-1} (~0.1C).

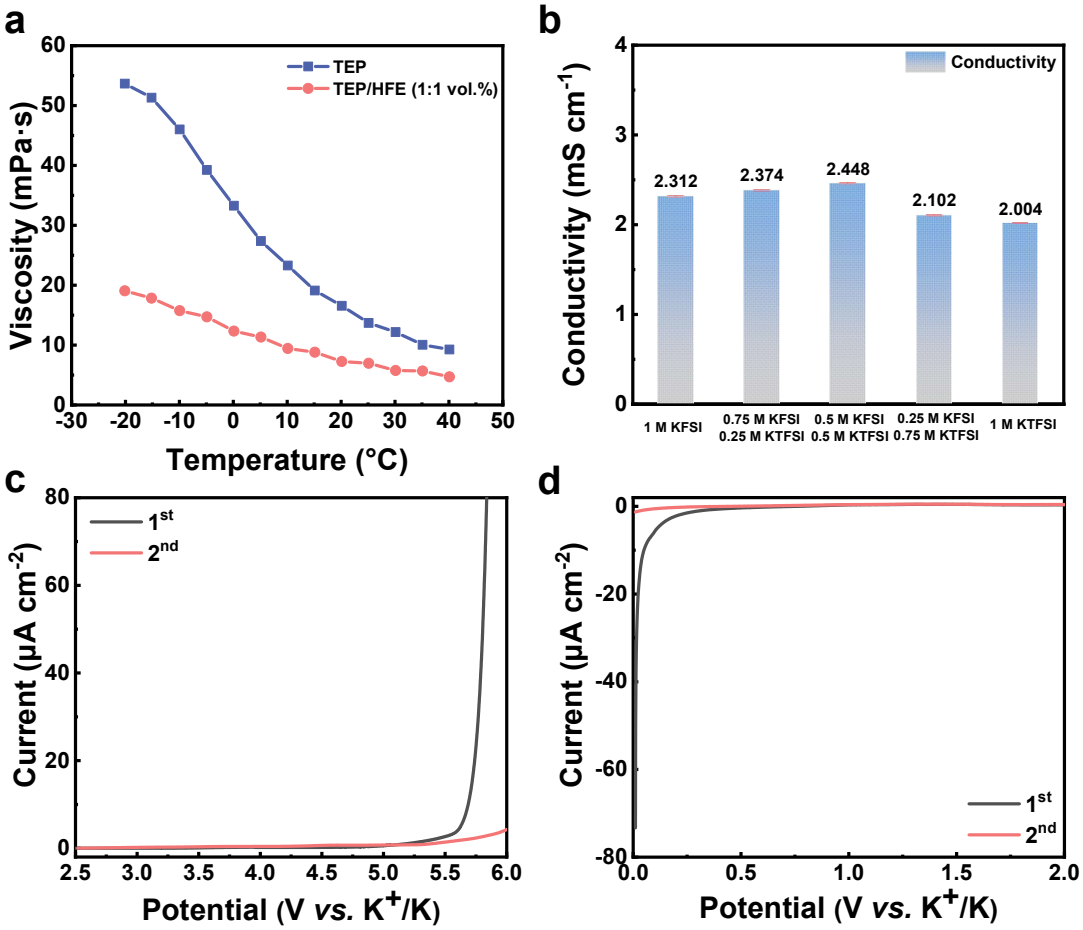

Fig. S4 Characterizations of the electrolyte. (a) Temperature dependent viscosity of the formulated electrolytes with or without the HFE in the temperature range of -20-40 °C. (b) The conductivity of the prepared localized high-concentration electrolytes with various concentration ratio of KFSI:KTFSI. (c, d) Linear scanning voltammetry (LSV) curves of the initial two scans at 1 mV s^{-1} in the 0.5 M KFSI and 0.5 M KTFSI dissolved in TEP and HFE electrolyte with Al foil as the working electrode and K metal as the counter and reference electrode.

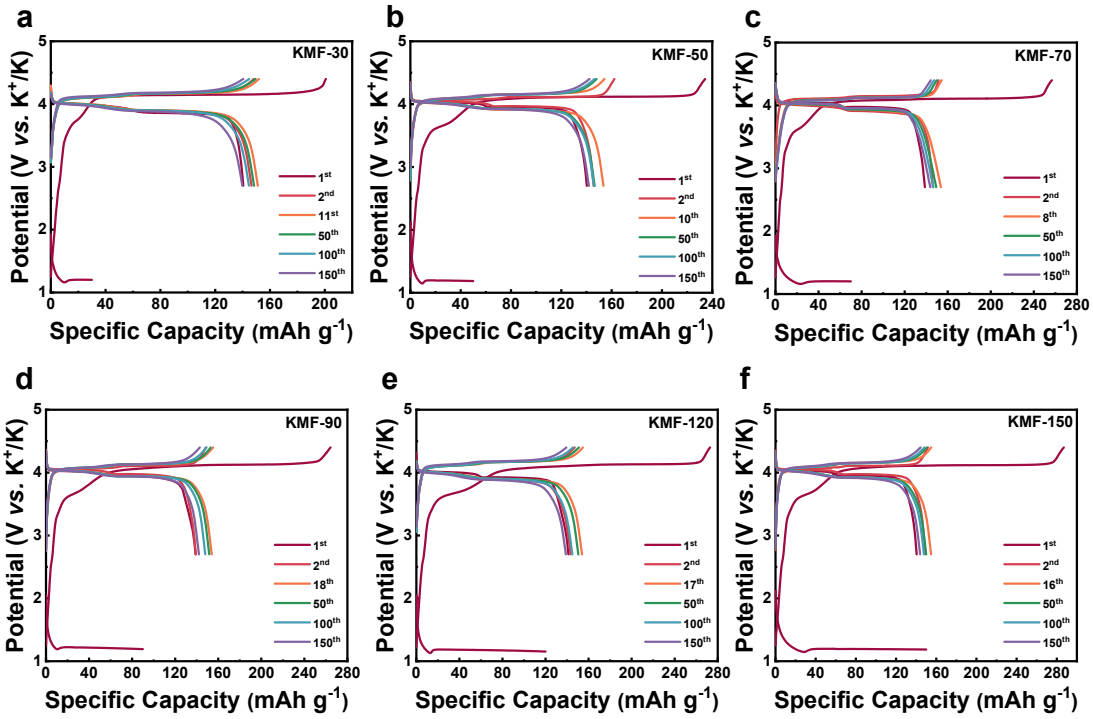

Fig. S5 Electrochemical performance of the KMF-K metal cells undergoing various initial overdischarge processes. Galvanostatic charge-discharge potential profiles of the KMF-K metal cells at 15 mA g^{-1} (~0.1C), (a) KMF-30, (b) KMF-50, (c) KMF-70, (d) KMF-90, (e) KMF-120, and (f) KMF-150.

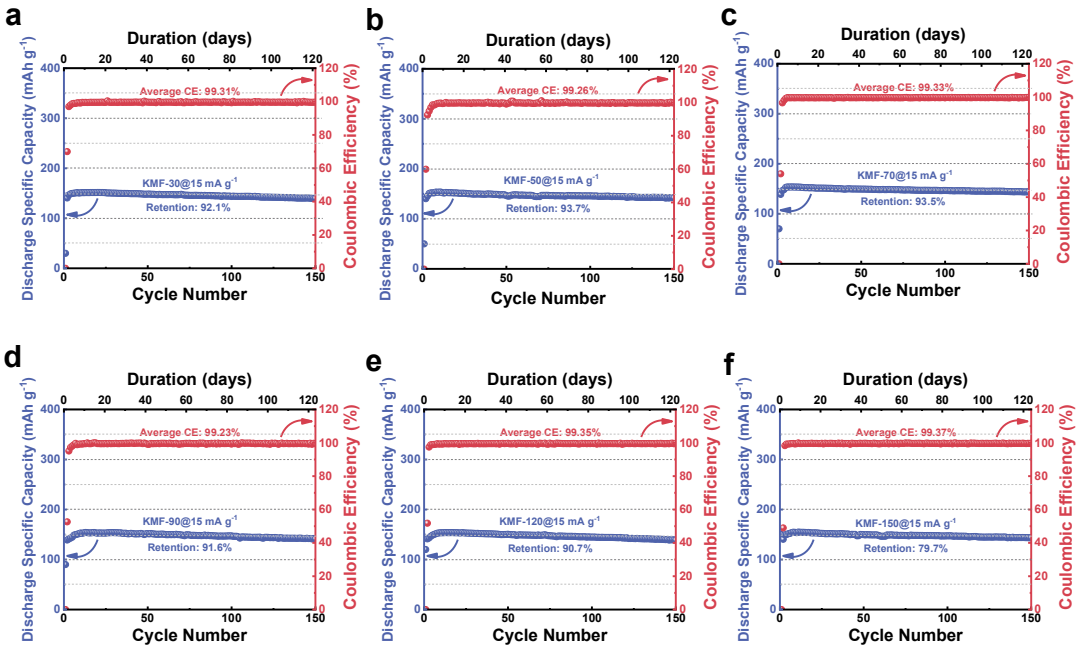

Fig. S6 Cycling stability of the KMF-K metal cells undergoing various initial overdischarge processes. (a) KMF-30, (b) KMF-50, (c) KMF-70, (d) KMF-90, (e) KMF-120, and (f) KMF-150.

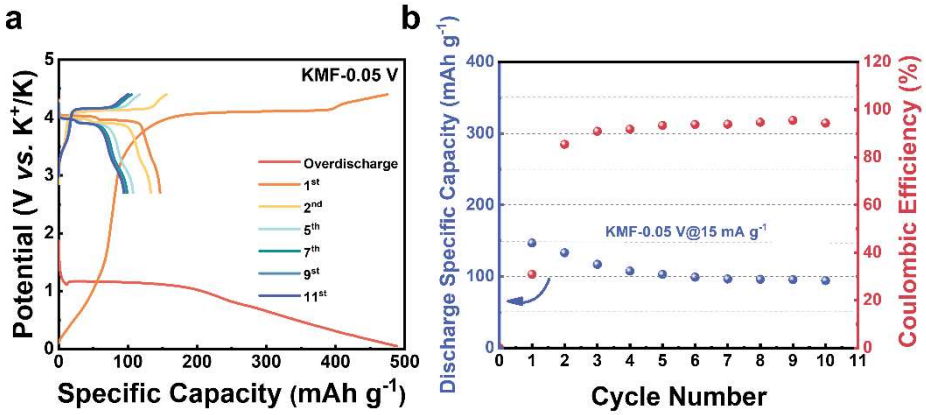

Fig. S7 Electrochemical performance of the KMF-K metal cell initially discharged to 0.05 V. (a) Galvanostatic charge-discharge potential profiles and (b) the corresponding cycling performance at 15 mA g^{-1} (~0.1C).

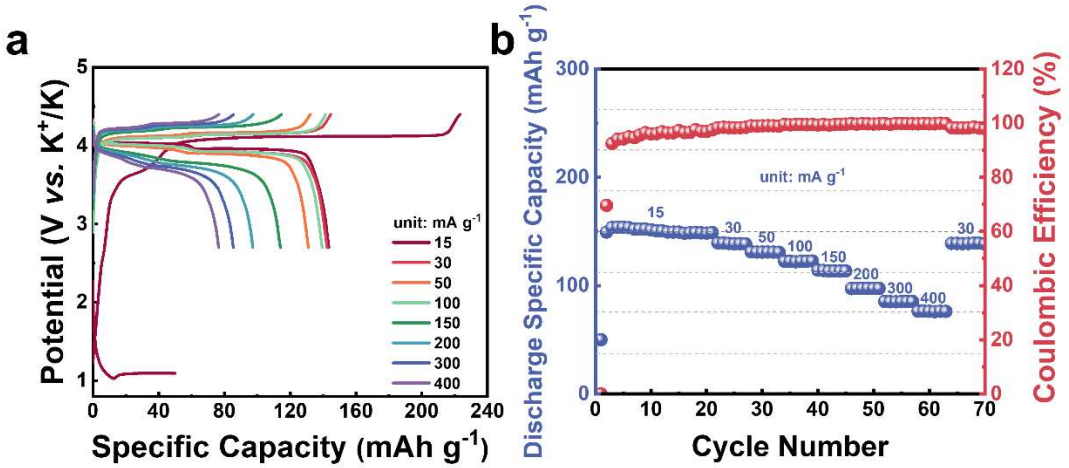

Fig. S8 Electrochemical performance of the KMF-50-K metal. (a, b) Potential profiles and rate capability at different specific currents from 15 to 400 mA g^{-1}.

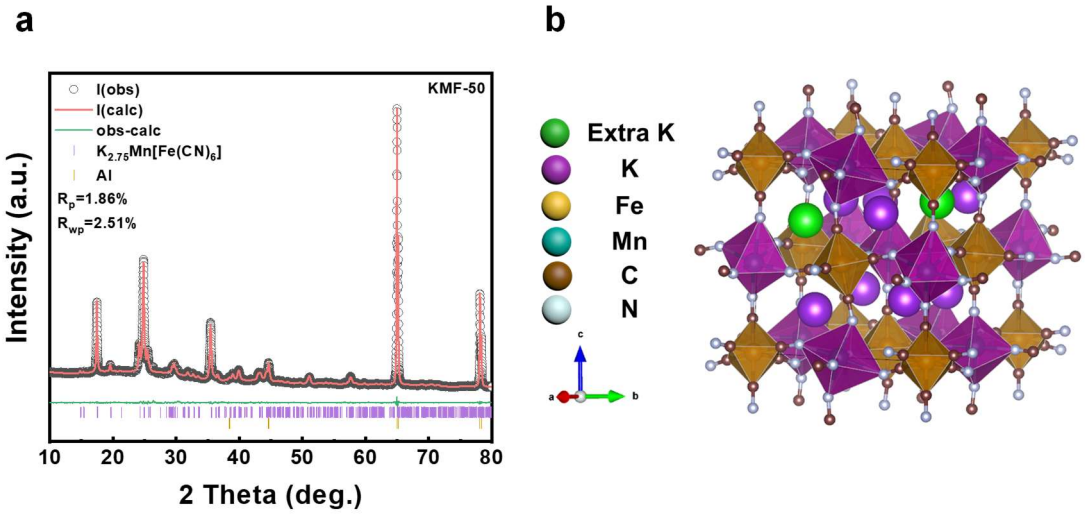

Figure S9. Crystalline structure characterizations of KMF-50. (a) XRD patterns and Rietveld refinement of the KMF-50. (b) The crystalline structure of KMF-50 retrieved from the Rietveld refinement.

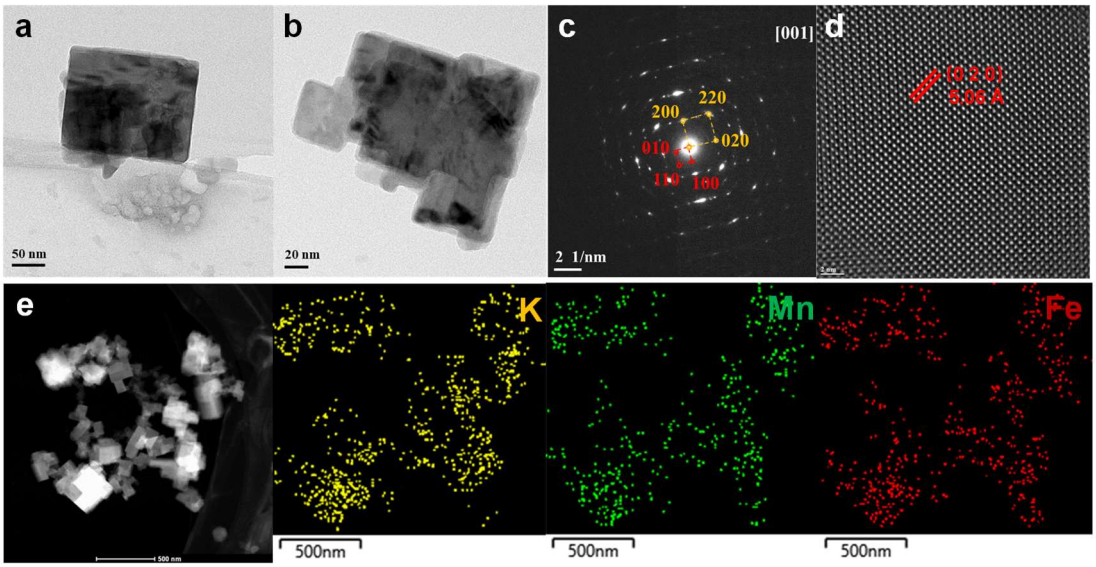

Fig. S10 Electron microscopic characterizations of KMF-50. (a, b) TEM images, (c) SAED pattern, and (d) HRTEM image of the KMF-50 with the *d*-spacings of the (020) crystal planes of monoclinic KMF marked. (e) TEM image and the corresponding K, Mn, and Fe elemental mapping results of KMF-50.

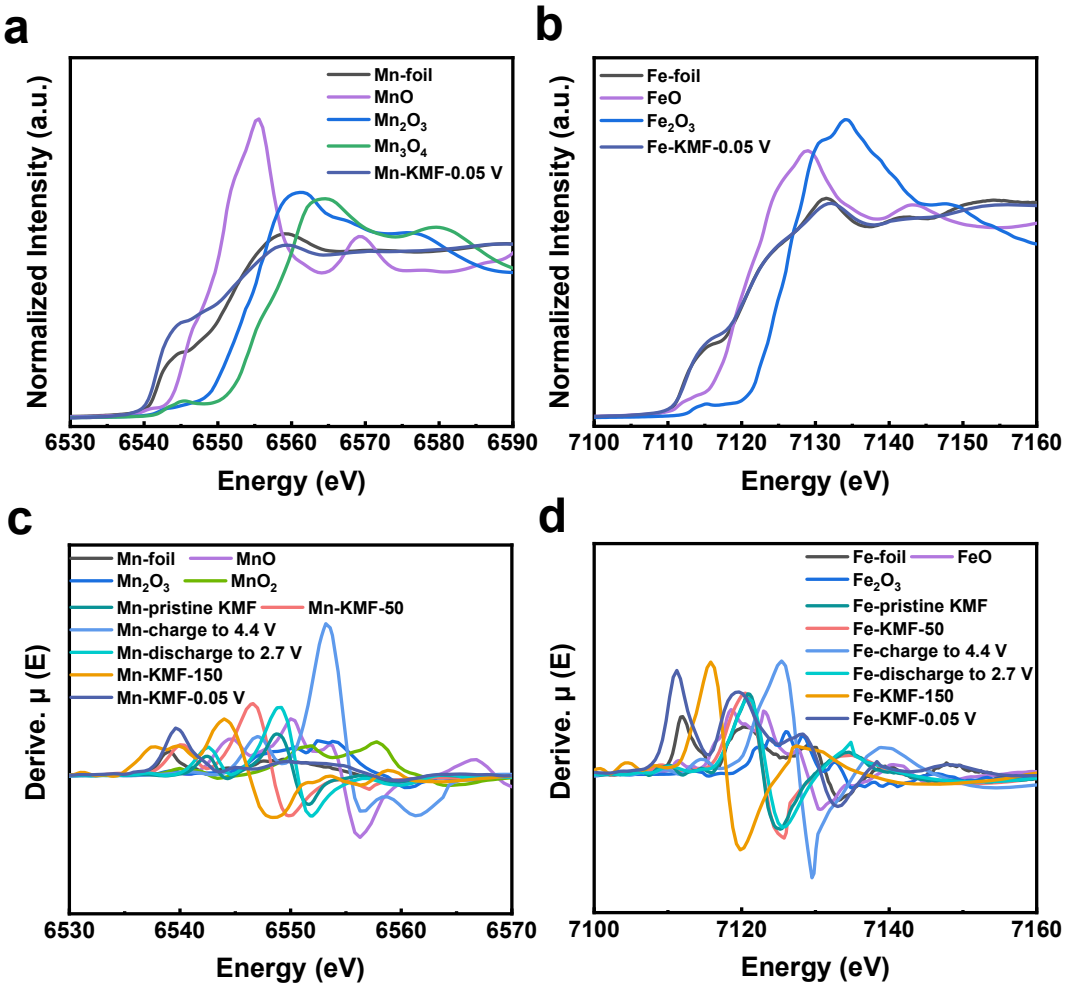

Fig. S11 *Ex-situ* XANES spectra of different KMF samples and standard samples. (a) Mn and (b) Fe *K*-edges. The first derivative derived from the principal absorption edge for (c) Mn and (d) Fe.

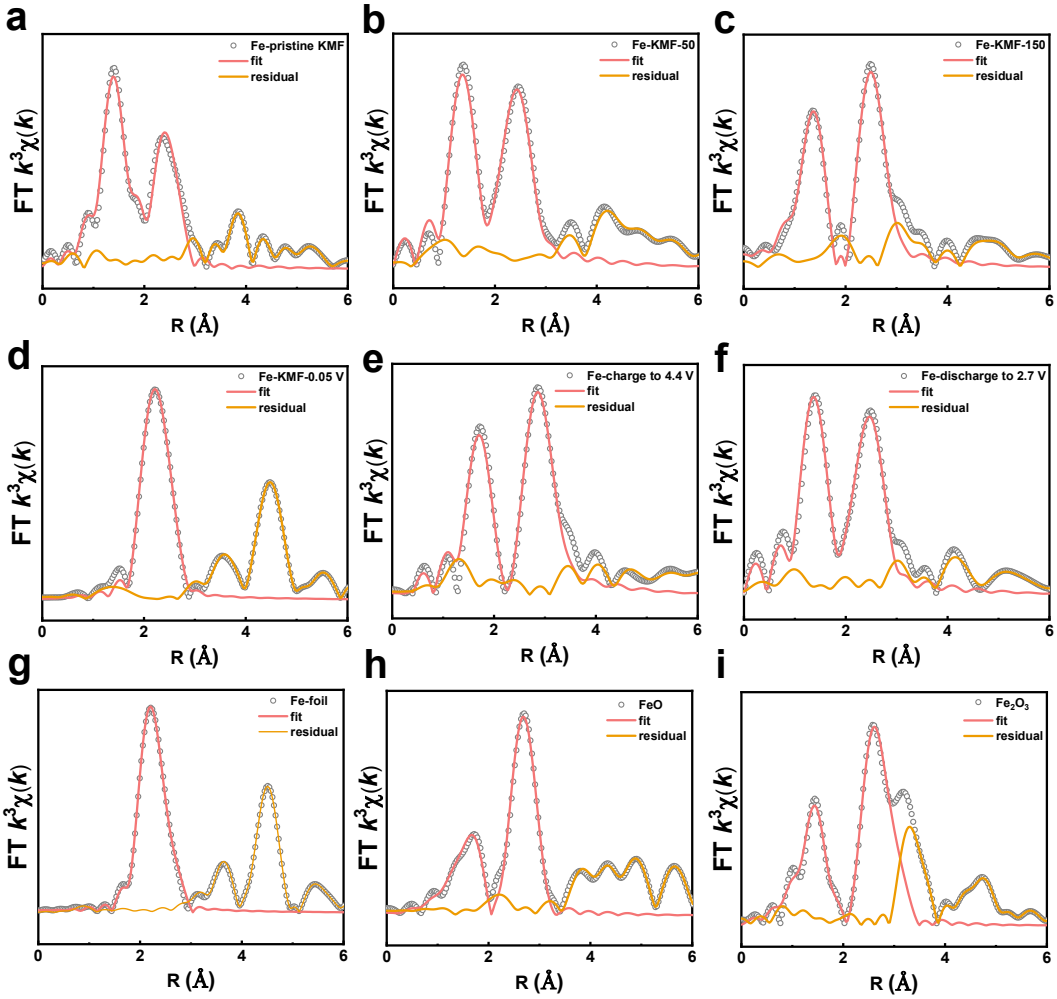

Fig. S12 Main results of the EXAFS analysis. k^3-weighted FT spectra in *R*-space for Fe in different KMF samples and standard samples.

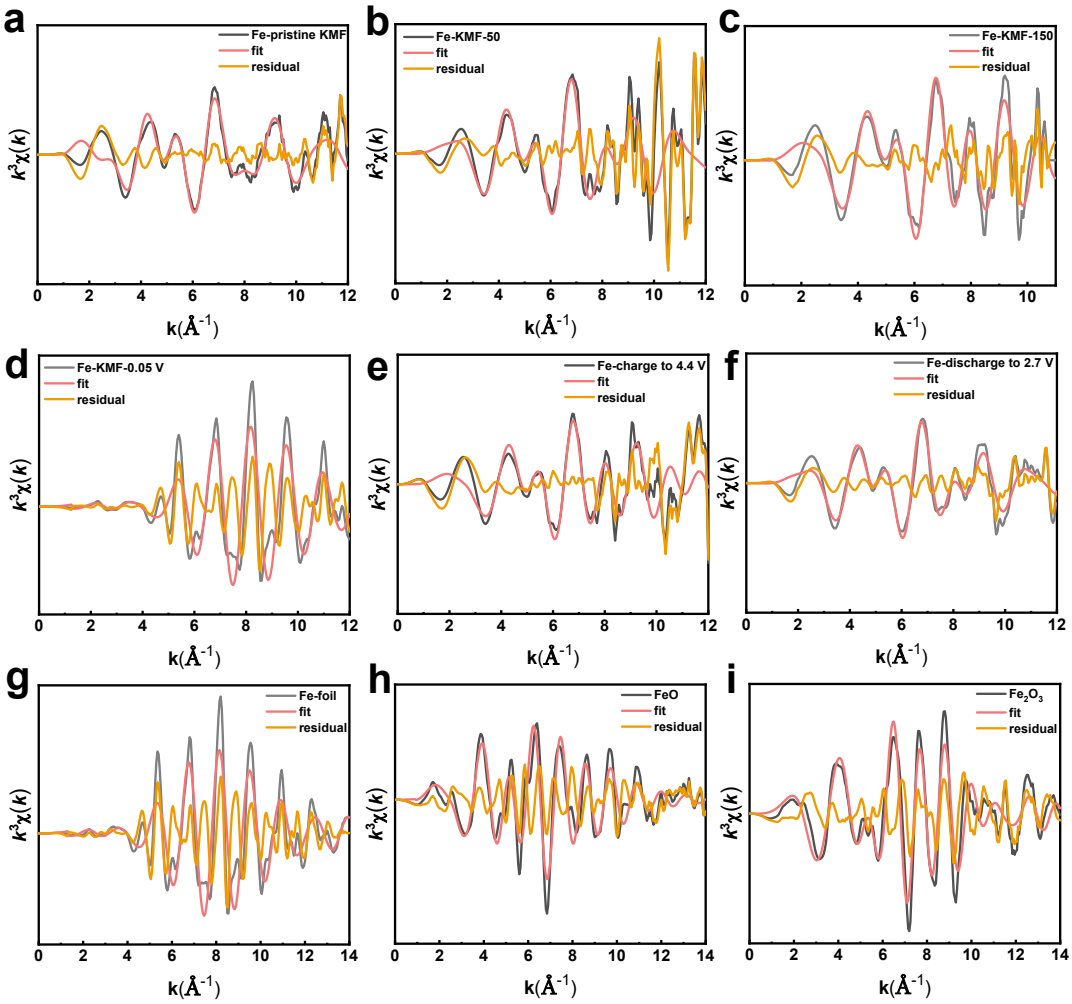

Fig. S13 Main results of the EXAFS analysis. k^3-weighted FT spectra in k-space for Fe in different KMF samples and standard samples.

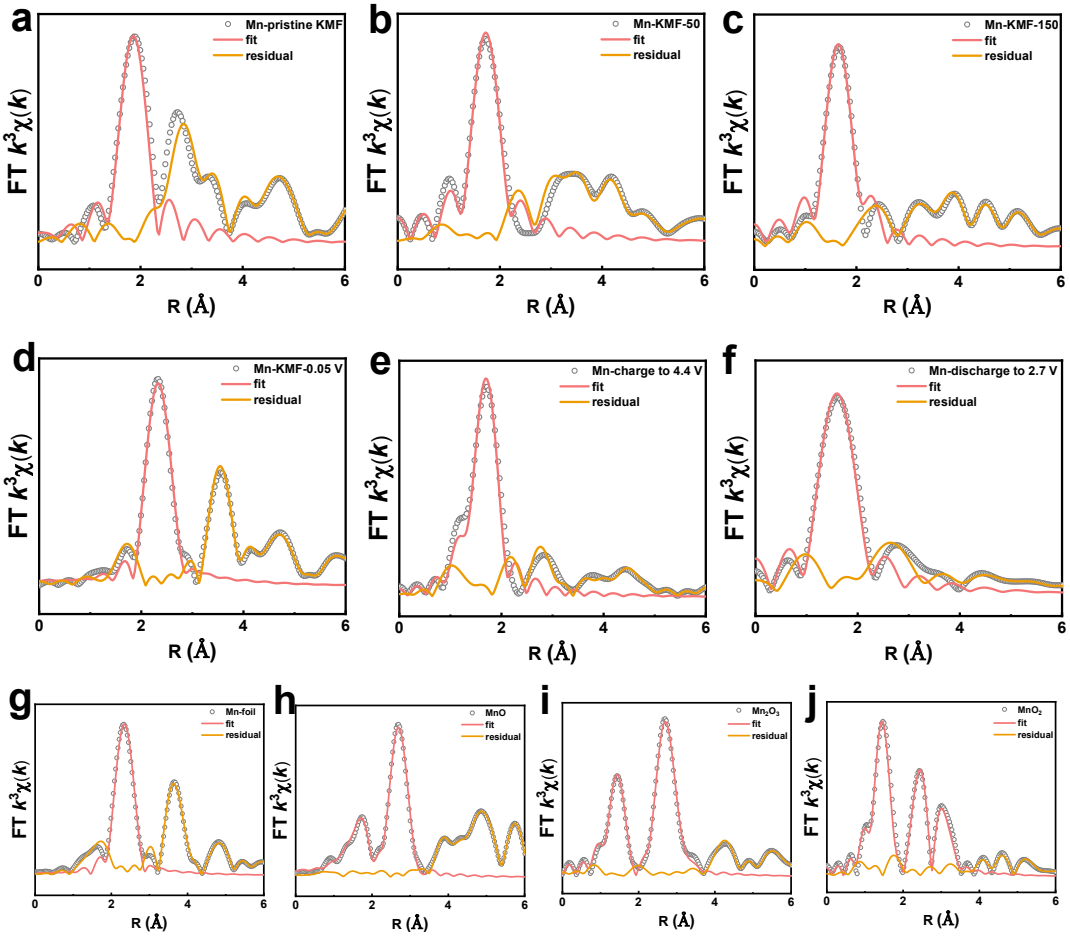

Fig. S14 Main results of the EXAFS analysis. k^3-weighted FT spectra in *R*-space for Mn in different KMF samples and standard samples.

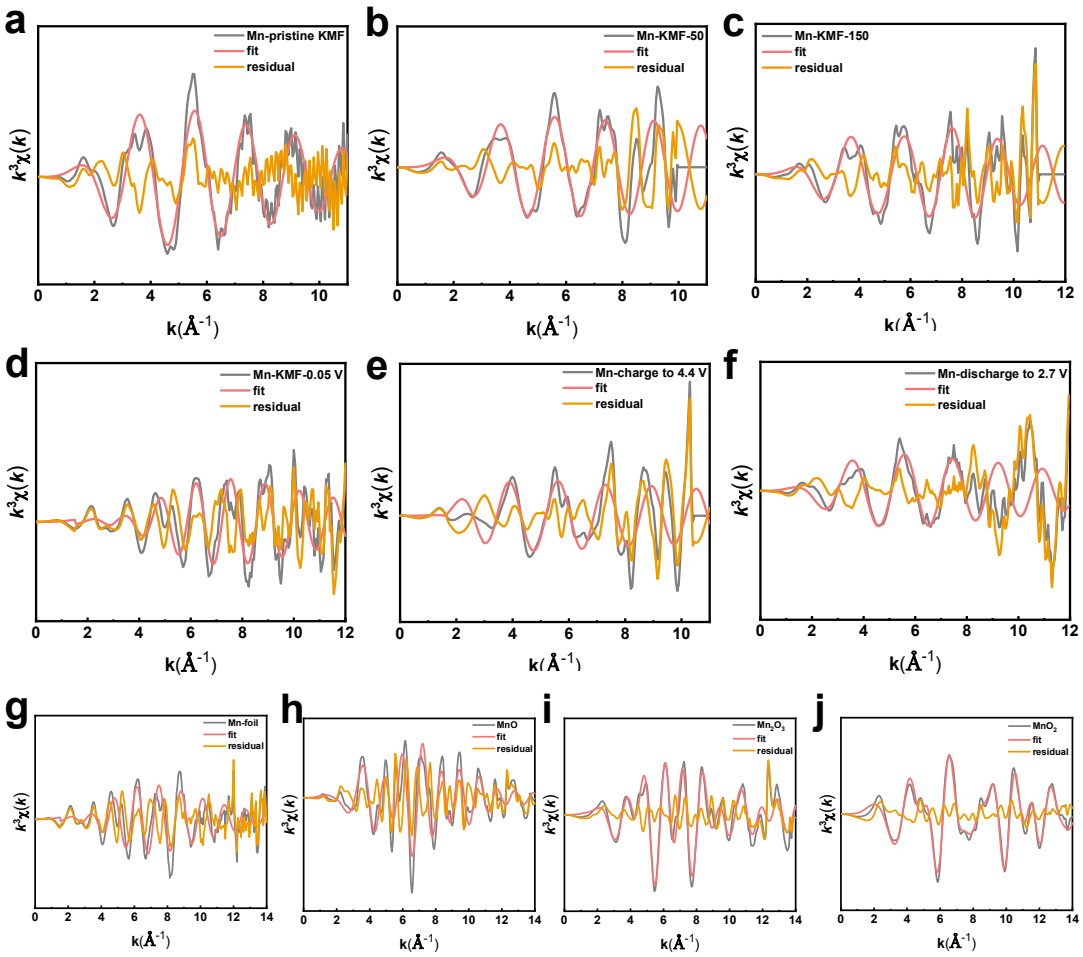

Fig. S15 Main results of the EXAFS analysis. k^3-weighted FT spectra in k-space for Mn in different KMF samples and standard samples.

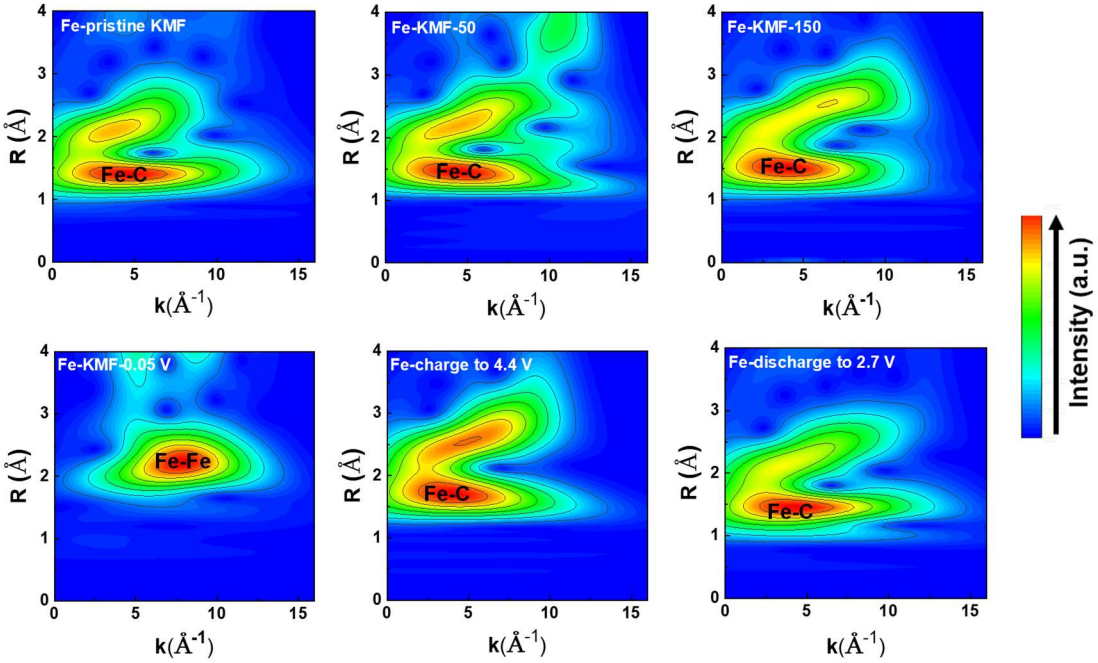

Fig. S16 Main results of the EXAFS analysis. The wavelet-transform images at the Fe *K*-edge in different KMF samples.

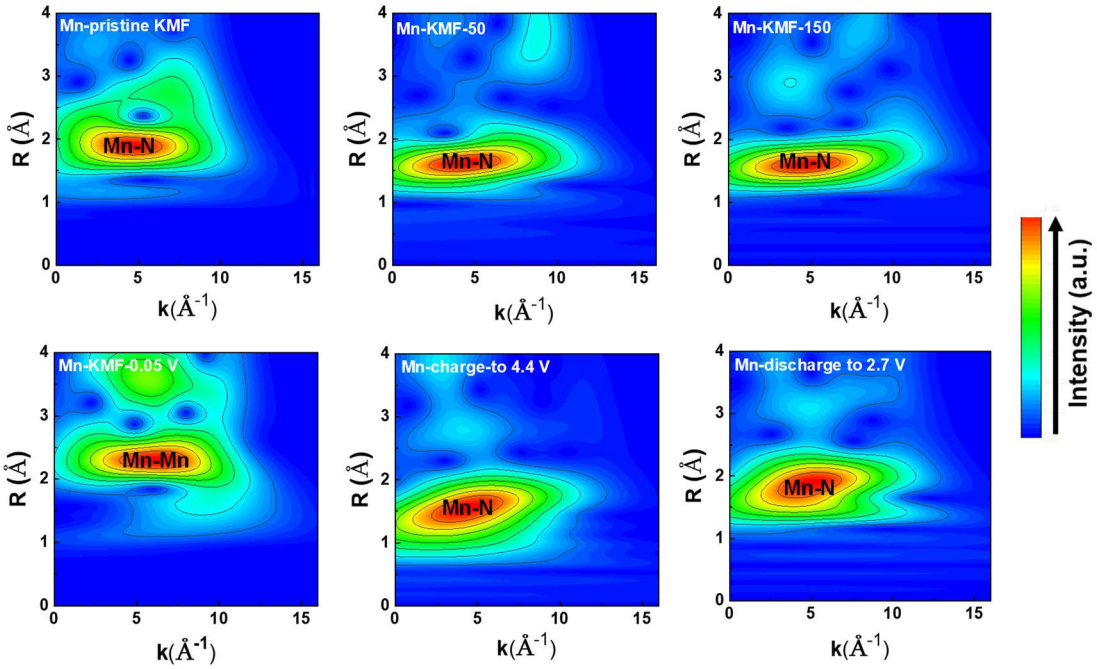

Fig. S17 Main results of the EXAFS analysis. The wavelet-transform images at the Mn *K*-edge in different KMF samples.

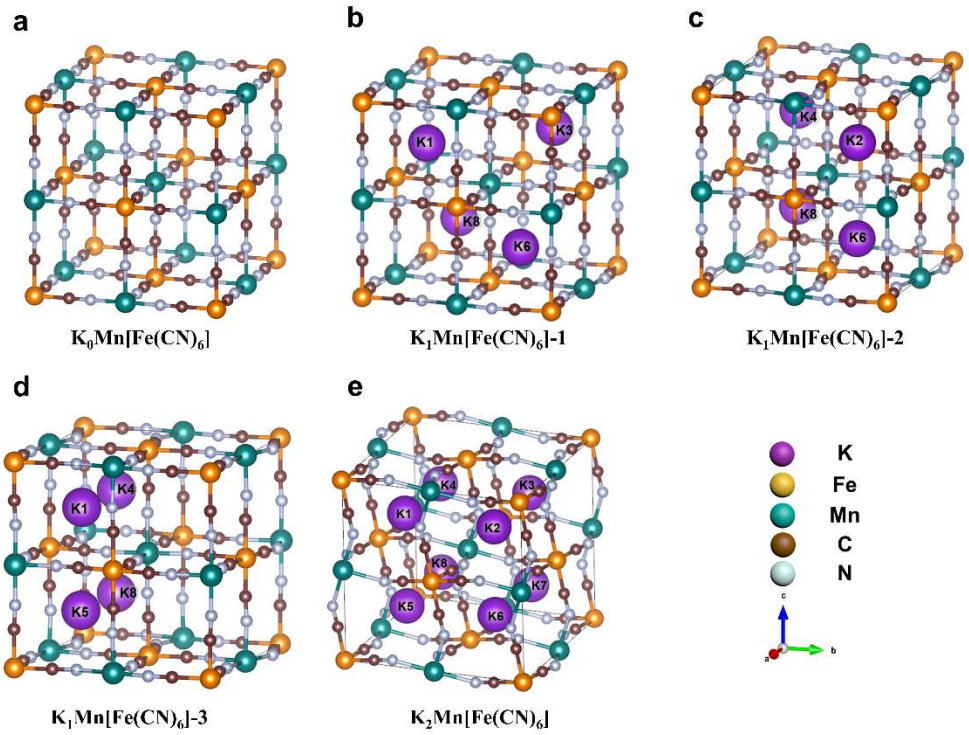

Fig. S18 First-principles calculations. The schematic crystal structure of the (a) $K_0Mn[Fe(CN)_6]$, (b) $K_1Mn[Fe(CN)_6]$-1, (c) $K_1Mn[Fe(CN)_6]$-2, (d) $K_1Mn[Fe(CN)_6]$-3 and (e) $K_2Mn[Fe(CN)_6]$ samples.

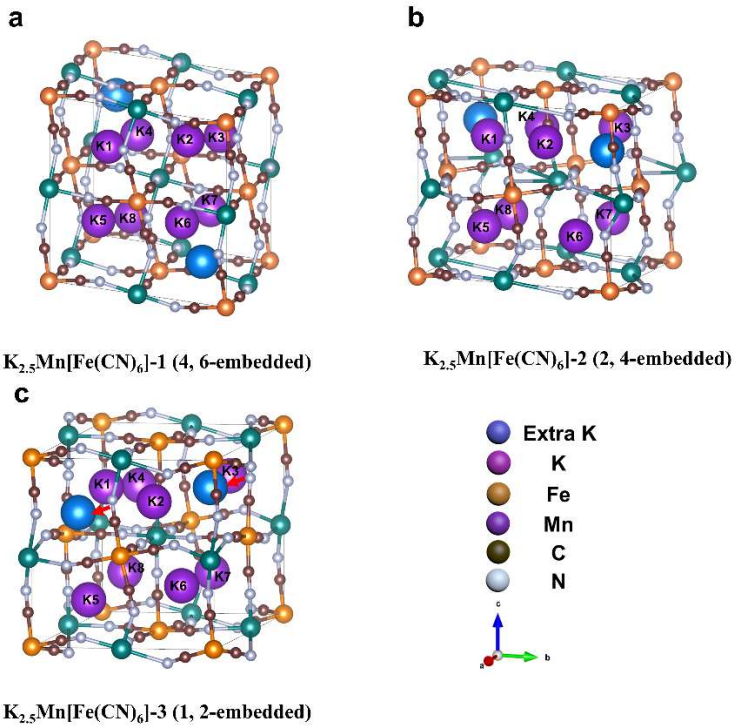

Fig. S19 First-principles calculations. The schematic crystal structure of the (a) $K_{2.5}Mn[Fe(CN)_6]$-1, (b) $K_{2.5}Mn[Fe(CN)_6]$-2, and (c) $K_{2.5}Mn[Fe(CN)_6]$-3 samples.

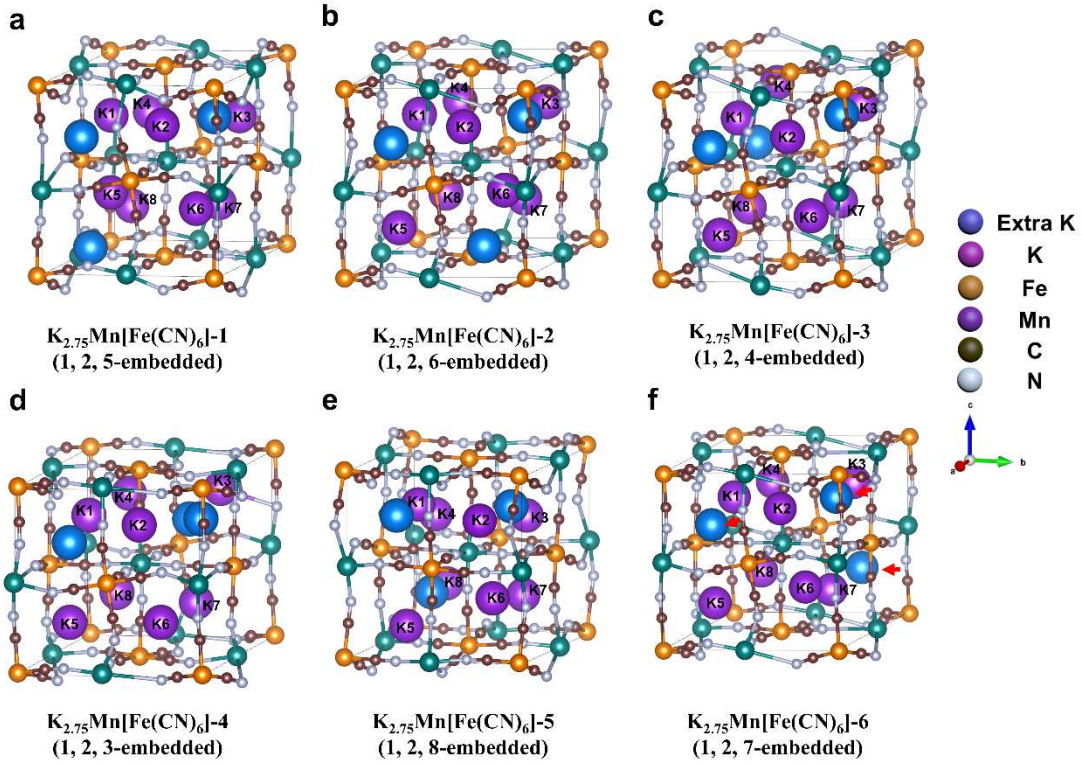

Fig. S20 First-principles calculations. The schematic crystal structure of the (a) $K_{2.75}Mn[Fe(CN)_6]$-1, (b) $K_{2.75}Mn[Fe(CN)_6]$-2, (c) $K_{2.75}Mn[Fe(CN)_6]$-3, (d) $K_{2.75}Mn[Fe(CN)_6]$-4, (e) $K_{2.75}Mn[Fe(CN)_6]$-5, and (f) $K_{2.75}Mn[Fe(CN)_6]$-6 samples.

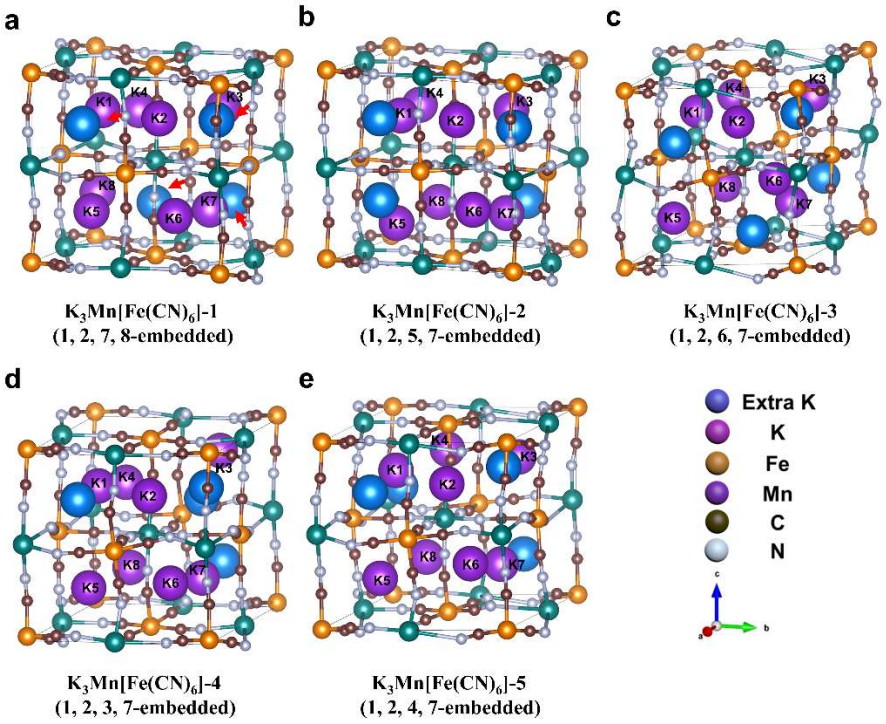

Fig. S21 First-principles calculations. The schematic crystal structure of the (a) $K_3Mn[Fe(CN)_6]$-1, (b) $K_3Mn[Fe(CN)_6]$-2, (c) $K_3Mn[Fe(CN)_6]$-3, (d) $K_3Mn[Fe(CN)_6]$-4, and (e) $K_3Mn[Fe(CN)_6]$-5 samples.

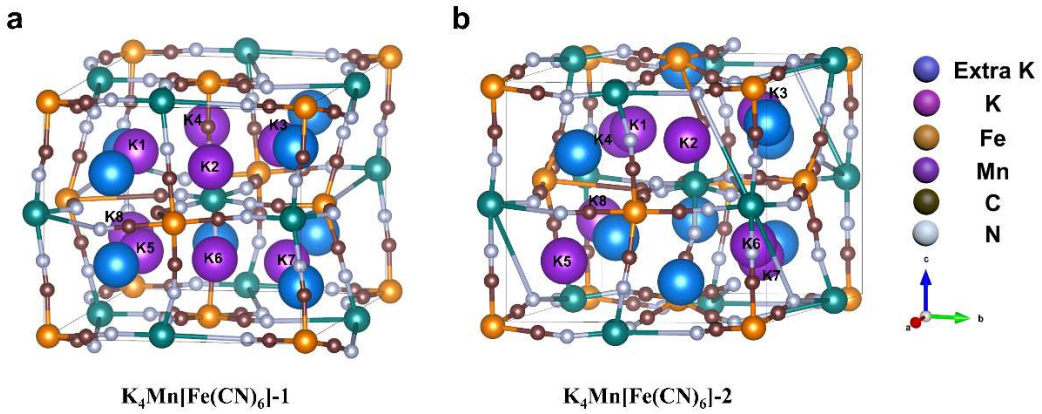

Fig. S22 First-principles calculations. The schematic crystal structure of the (a) $K_4Mn[Fe(CN)_6]$-1 and (b) $K_4Mn[Fe(CN)_6]$-2 samples.

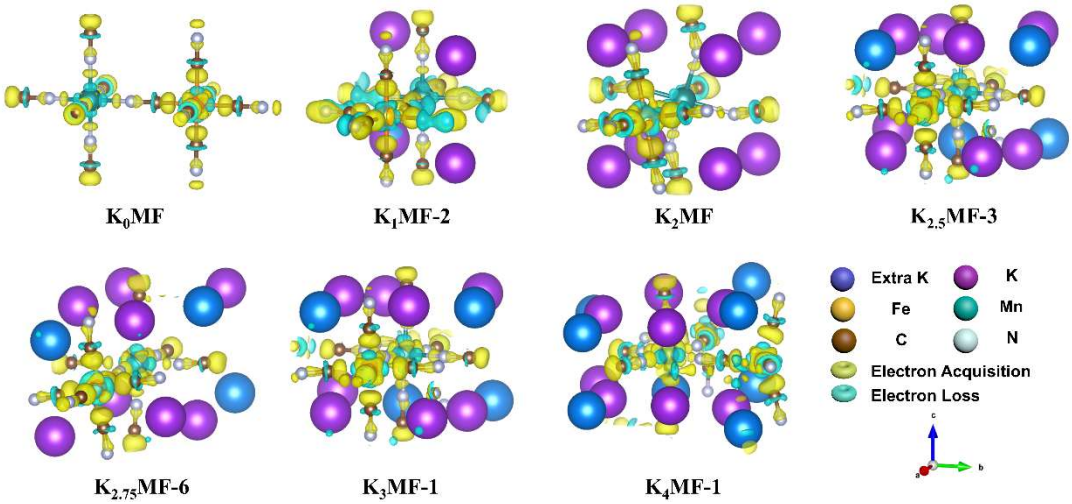

Fig. S23 First-principles calculations. The charge density difference of Mn and Fe in K_0MF, K_1MF-2, K_2MF, $K_{2.5}MF$-3, $K_{2.75}MF$-6, K_3MF-1 and K_4MF-1. Here, yellow indicates electron acquisition and blue indicates electron loss.

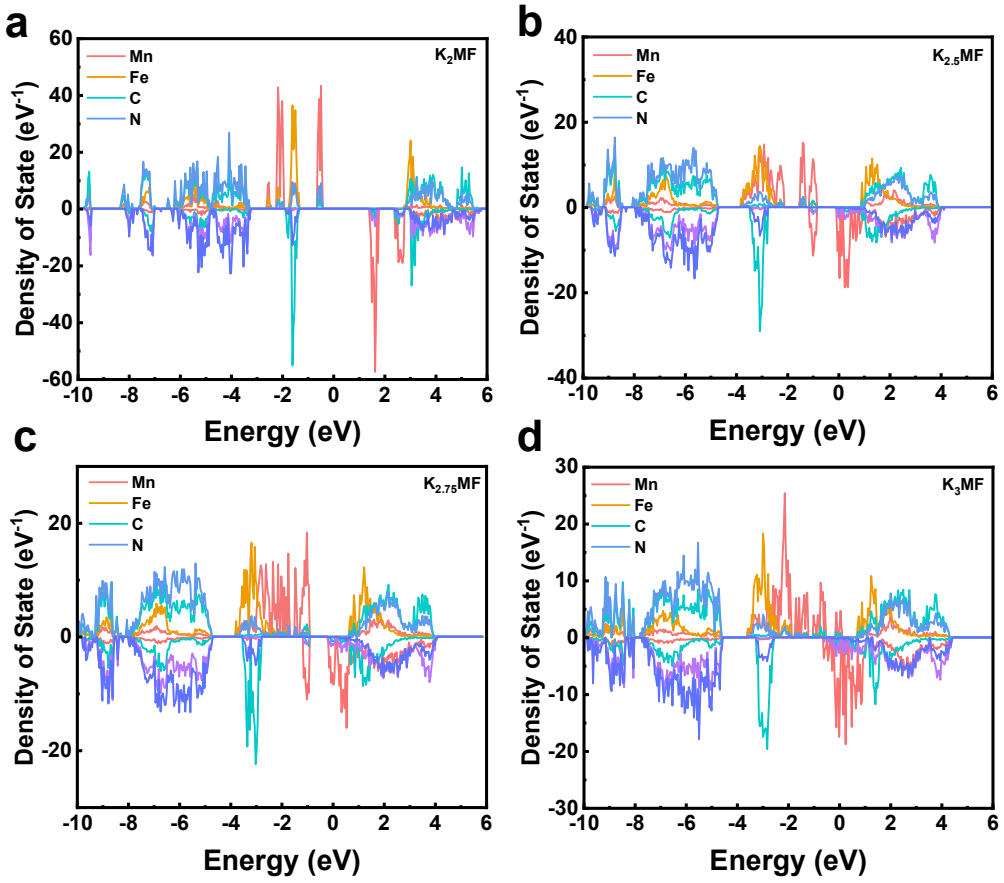

Fig. S24 First-principles calculations. The density of states of K_xMF calculated by using the HSE functional. Here, the Fermi energy is set as zero. (a) K_2MF, (b) $K_{2.5}MF$, (c) $K_{2.75}MF$, and (d) K_3MF.

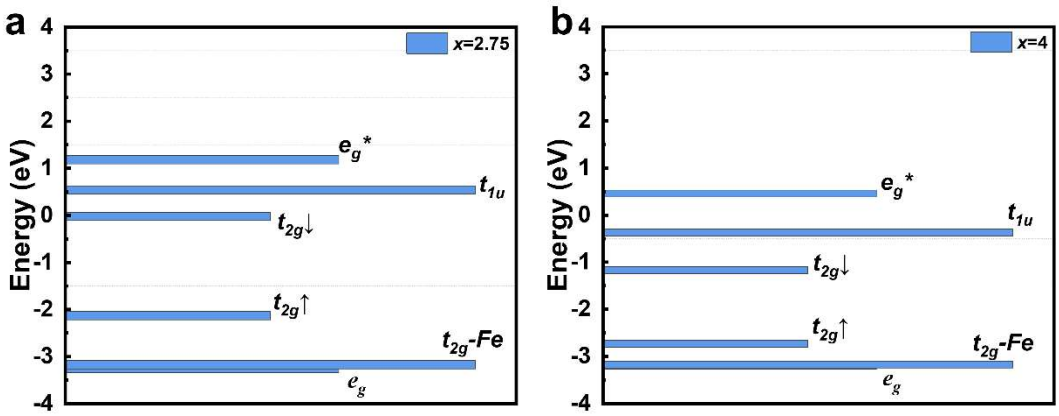

Fig. S25 First-principles calculations. Schematic of the band structure for (a) $K_{2.75}Mn[Fe(CN)_6]$ and (b) $K_4Mn[Fe(CN)_6]$.

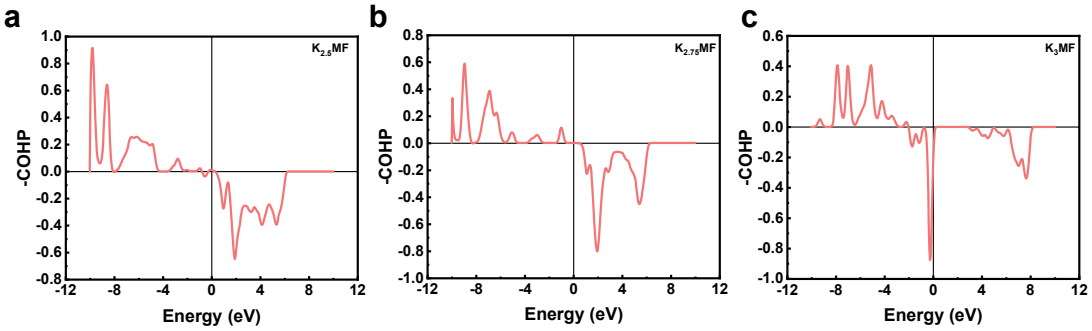

Fig. S26 First-principles calculations. The Crystal Orbital Hamilton Population (COHP) of (a) $K_{2.5}MF$, (b) $K_{2.75}MF$, and c) K_3MF.

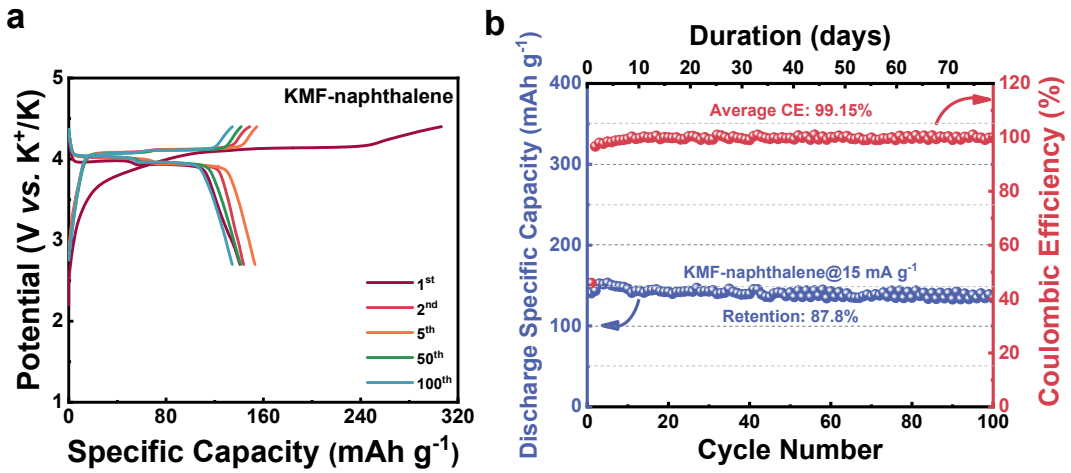

Fig. S27 Electrochemical performance of the chemically overpotassiated KMF-K metal cell. (a) Galvanostatic charge-discharge potential profiles and (b) cycling performance of the KMF-naphthalene at 15 mA g^{-1} (~0.1C). Note: the chemically overpotassiated KMF electrodes are synthesized by reacting pristine KMF electrodes with potassium-naphthalene solution with the detailed experimental procedure shown in synthesis of the chemically overpotassiated KMF electrodes section.

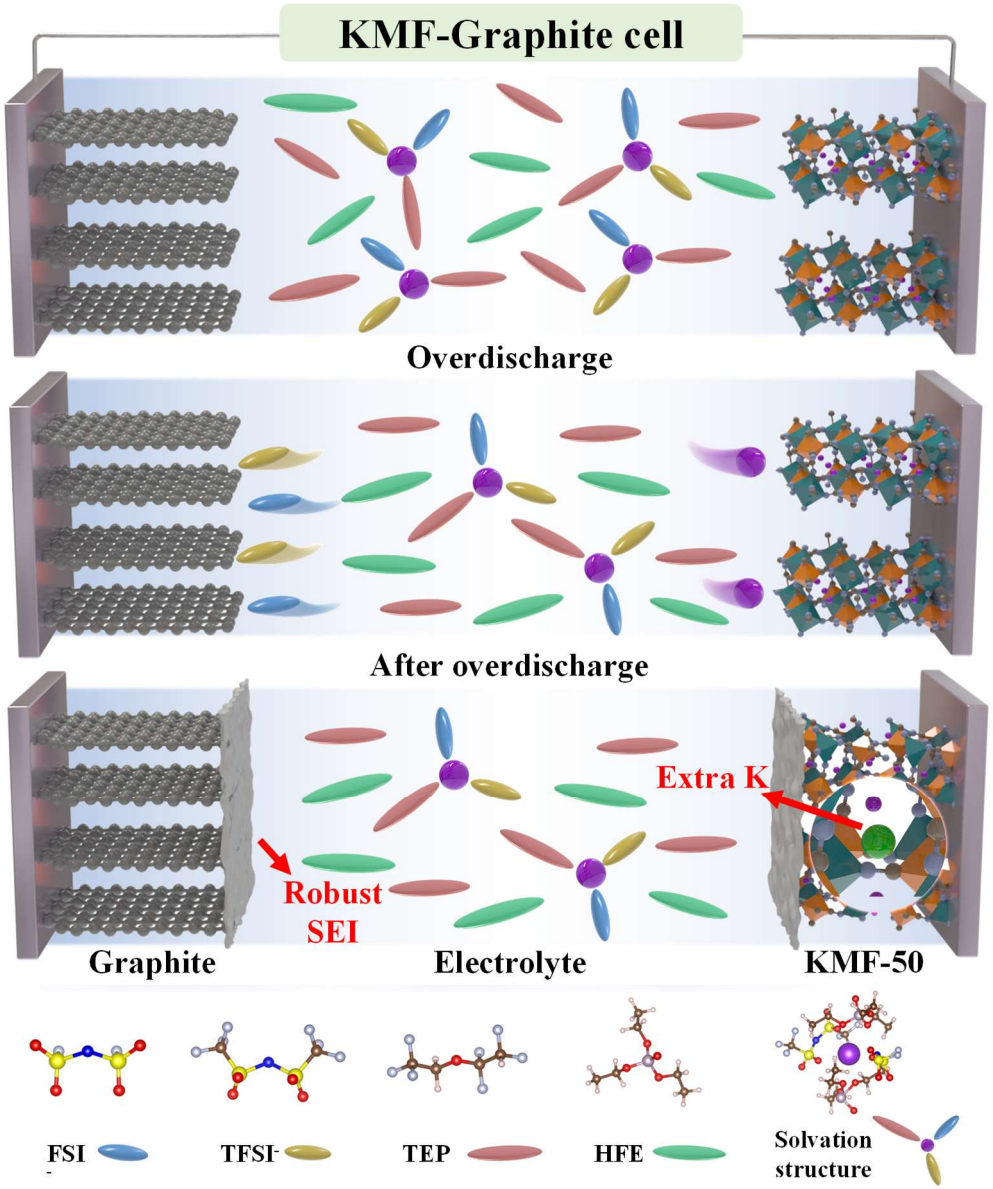

Fig. S28 Schematic illustration of the overdischarge process in the KMF-graphite cell.

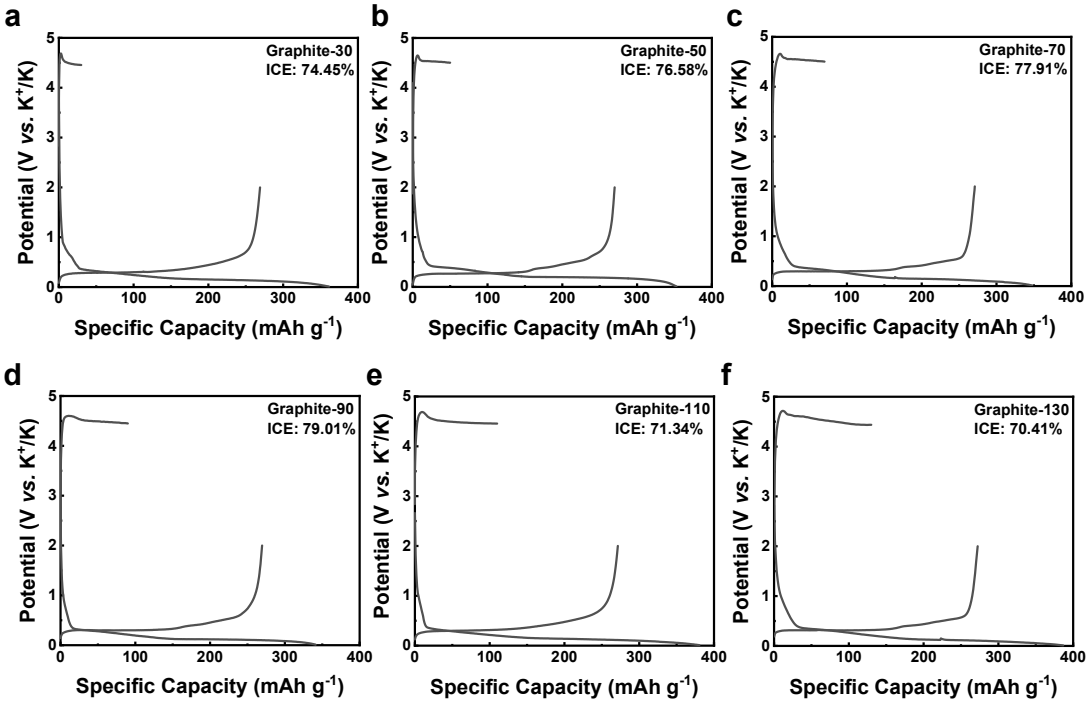

Fig. S29 Electrochemical performance of the graphite-K metal cells undergoing various initial overcharge processes. Galvanostatic charge-discharge potential profiles of the graphite-K metal cells at 50 mA g^{-1}, in which graphite undergoes initial overcharge to specific capacities of (a) 30, (b) 50, (c) 70, (d) 90, (e) 110, and (f) 130 mAh g^{-1}.

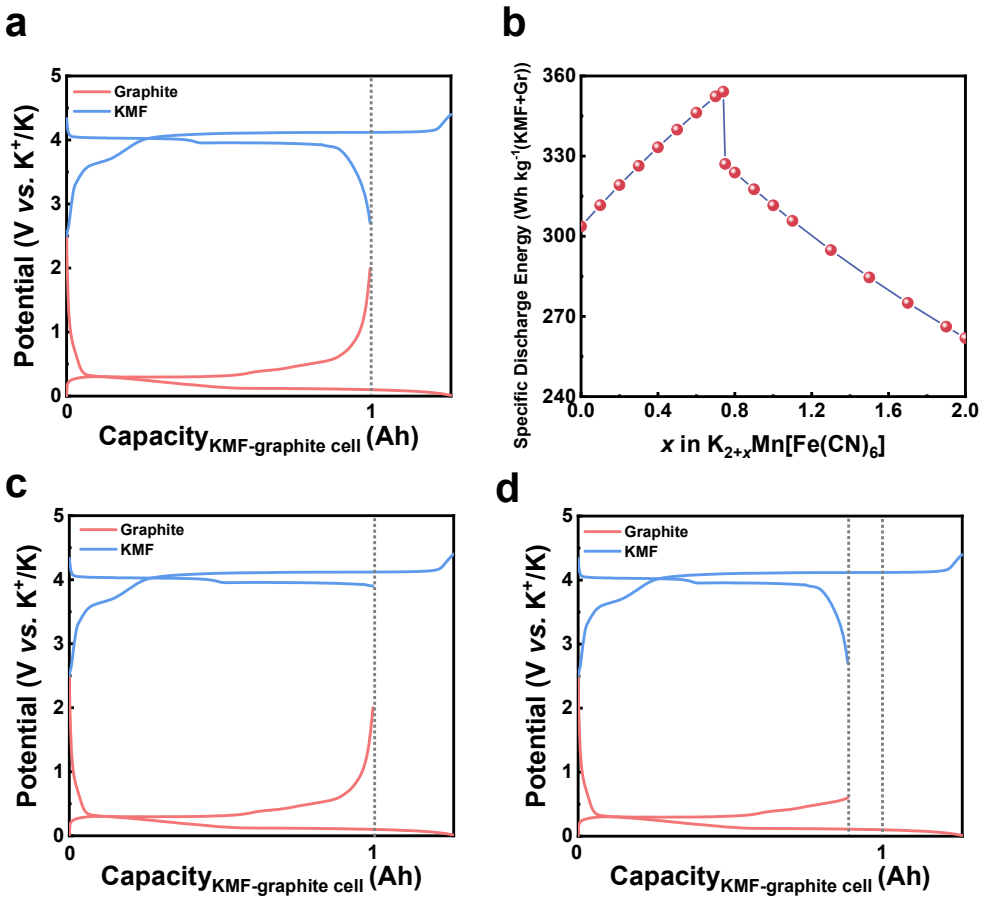

Fig. S30 Calculation of the specific energy in the overpotassiated KMF-graphite cell. (a) The calculated galvanostatic charge-discharge potential profiles of the $K_{2+x}MF$-graphite cell when x=0.74 in $K_{2+x}MF$. (b) The calculated specific energy of the $K_{2+x}MF$-graphite cell (based on the total mass of $K_{2+x}MF$ and graphite in the cell) versus the overpotassiation degree. (c) The calculated galvanostatic charge-discharge potential profiles of the $K_{2+x}MF$-graphite cell when x<0.74. (d) The calculated galvanostatic charge-discharge potential profiles of the $K_{2+x}MF$-graphite cell when x>0.74.

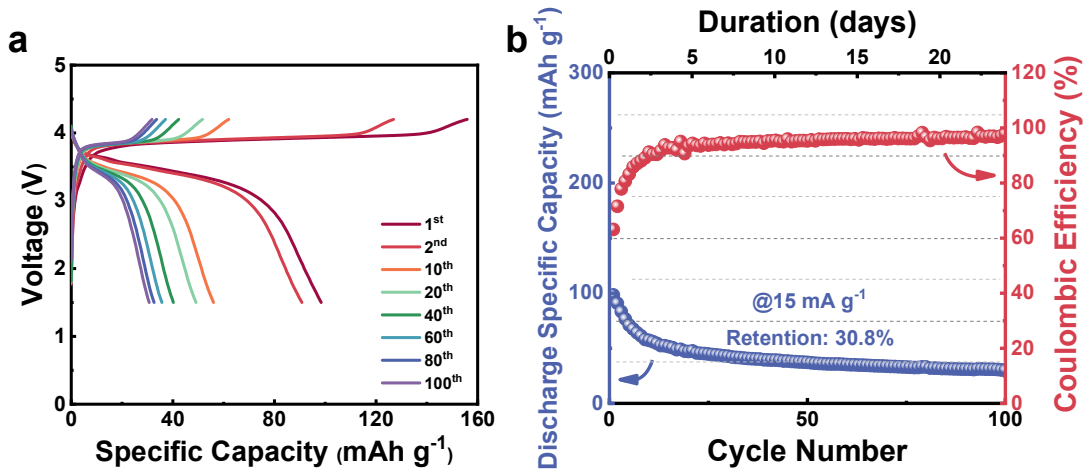

Fig. S31 Electrochemical performance of the KMF-graphite cell without overdischarge treatment. (a) Galvanostatic charge-discharge voltage profiles and (b) cycling performance at 15 mA g^{-1} (~0.1C).

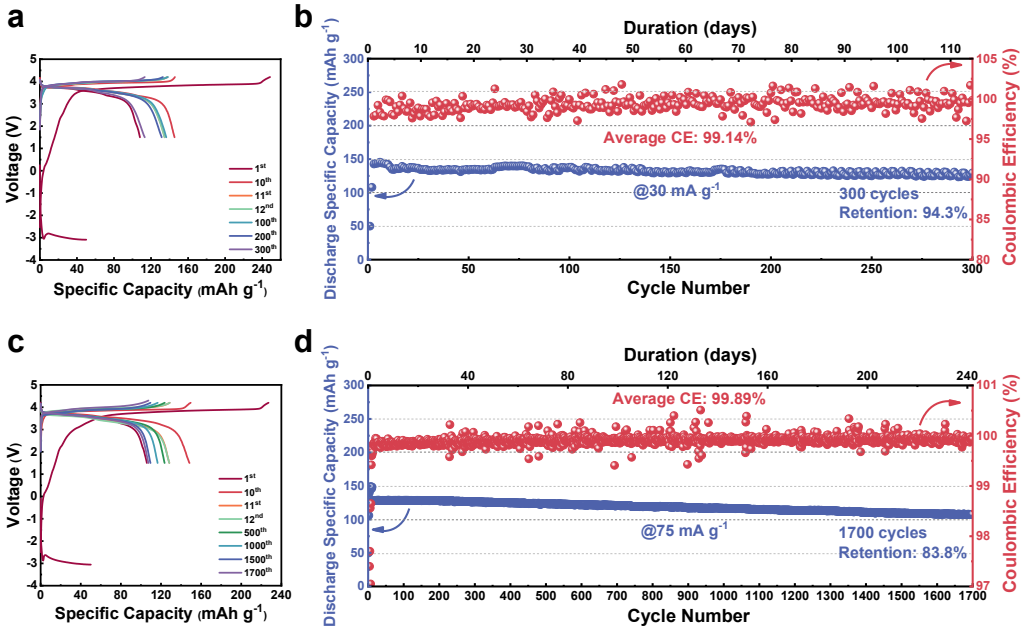

Fig. S32 Electrochemical performance of the KMF-graphite cells with overdischarge treatment. (a) Galvanostatic overdischarge-charge-discharge voltage profiles and (b) cycling performance at 30 mA g^{-1} (~0.2 C). (c) Galvanostatic overdischarge-charge-discharge voltage profiles and (d) cycling performance at 75 mA g^{-1} (~0.5 C).

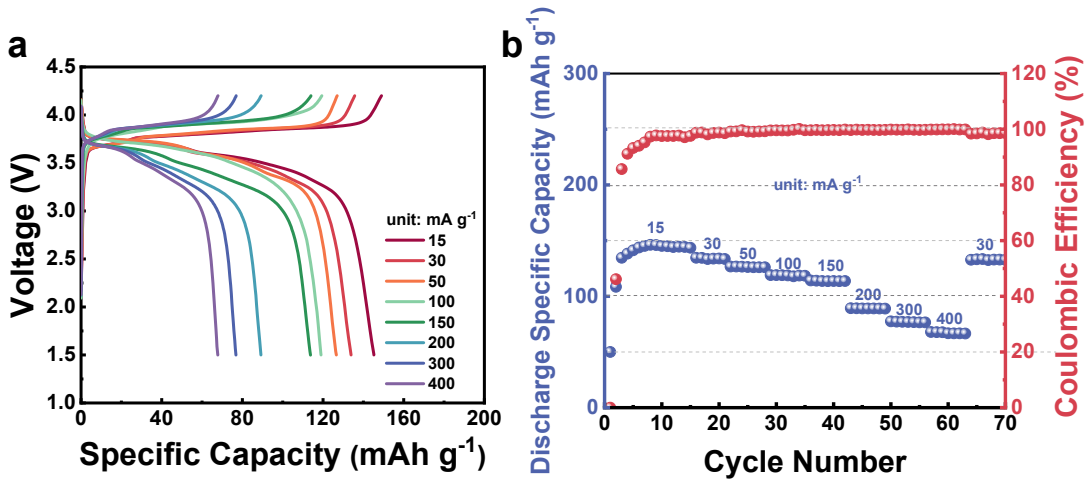

Fig. S33 Rate performance of the KMF-graphite cell with overdischarge treatment. (a) Galvanostatic charge-discharge voltage profiles and (b) rate capability at different specific currents from 15 mA g^{-1} to 400 mA g^{-1}.

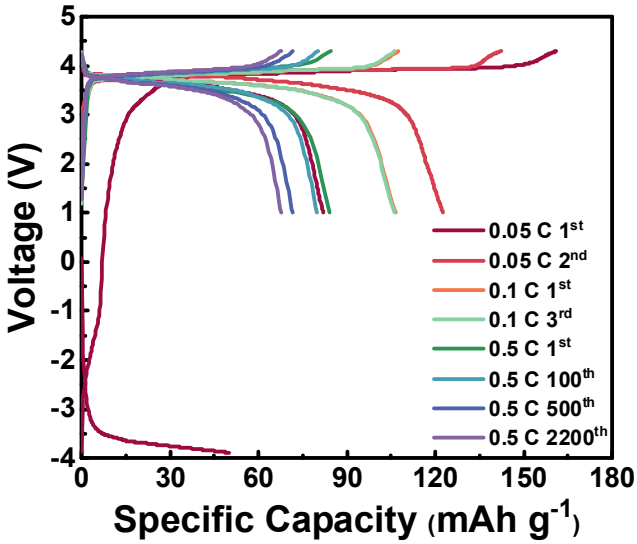

Fig. S34 Electrochemical performance of the KMF-graphite pouch-cell-1 with overdischarge treatment. Galvanostatic overdischarge-charge-discharge voltage profiles of the KMF-graphite pouch-cell.

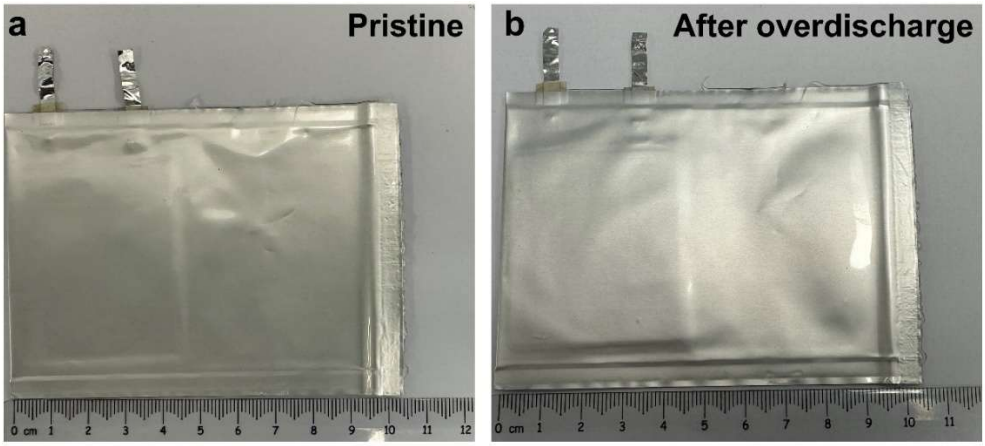

Fig. S35 The digital images of the pouch-cell-1 at various stages. (a) Pristine pouch-type cell-1. (b) Pouch-cell-1 after overdischarge.

Fig. S36 The digital images showing the thickness of the pouch-cell-1 at various stages. (a) Pouch-cell-1 before cycling at 0.5C. (b) Pouch-cell-1 after cycling for 2200 cycles at 0.5C.

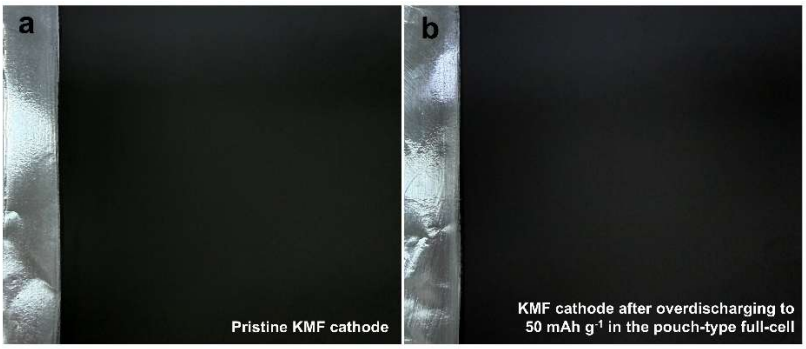

Fig. S37 The digital images of the KMF cathode at various stages. (a) The pristine KMF cathode. (b) The KMF cathode after overdischarging to 50 mAh g^{-1} in the pouch-type full-cell.

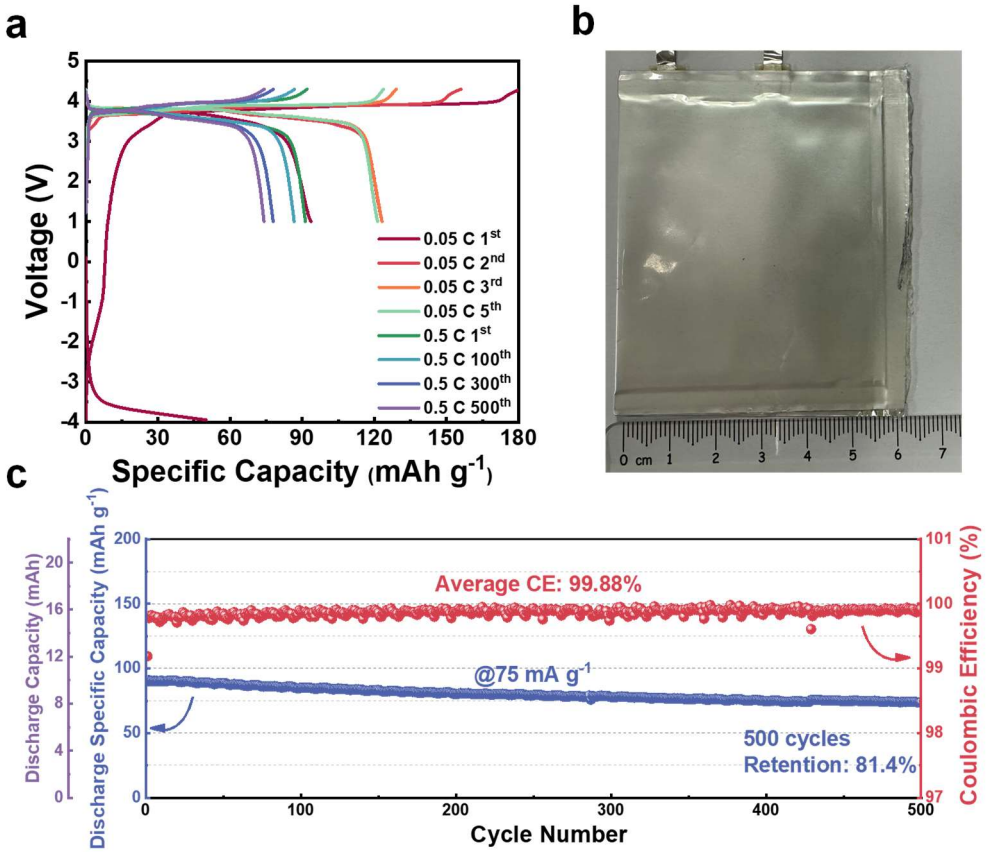

Fig. S38 Electrochemical performance of the KMF-graphite pouch-cell-2. (a) Galvanostatic overdischarge-charge-discharge voltage profiles of the pouch-cell. (b) The digital image of the pouch-cell-2. (c) Cycling performance of the KMF-graphite pouch-cell-2 at 75 mA g^{-1} (~0.5 C).

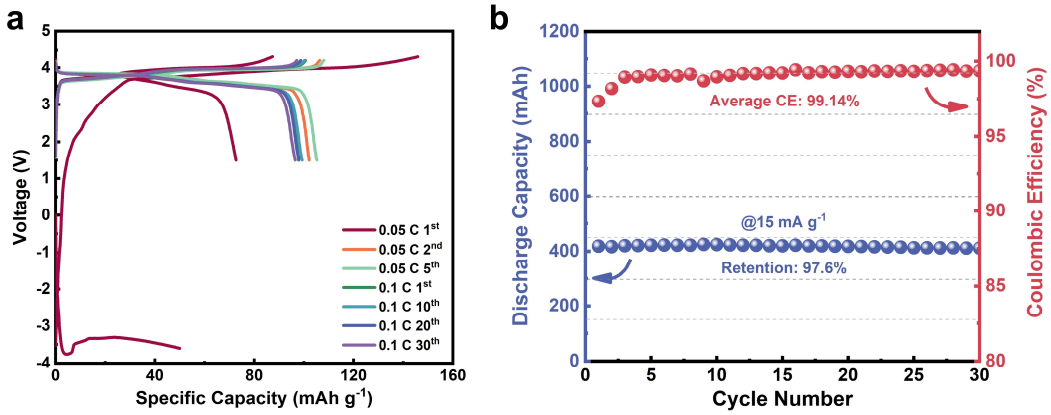

Fig. S39 Electrochemical performance of the large-capacity KMF-graphite pouch-type full-cell. (a) Galvanostatic overdischarge-charge-discharge voltage profiles and (b) cycling performance of the large-capacity pouch-type full-cell at 15 mA g-1 (~0.1 C, calculated based on mass of KMF in the cell).

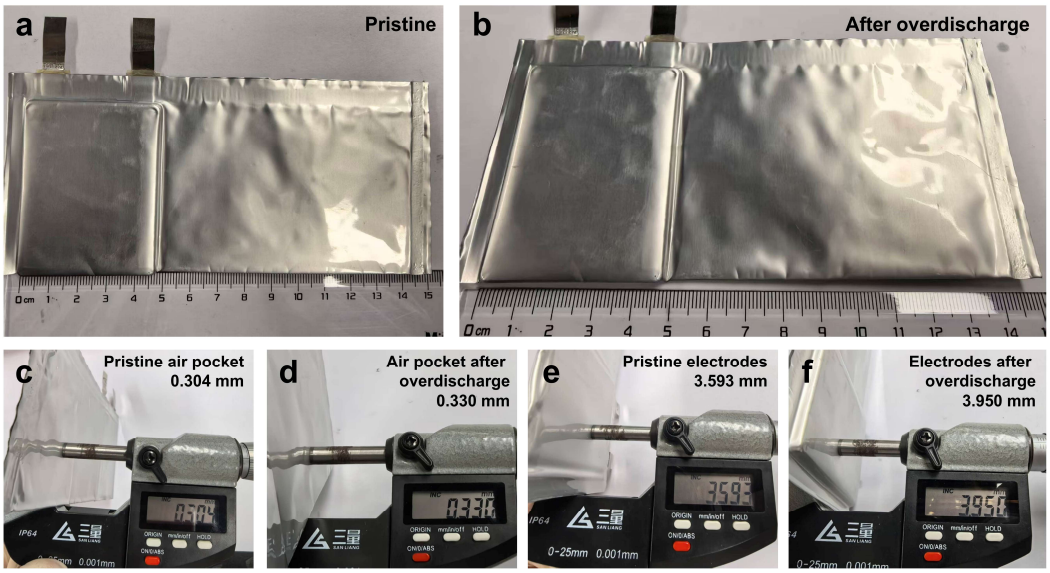

Fig. S40 The digital images of the large-capacity pouch-type full-cell at various stages. The large-capacity pouch-type full-cell (a) before and (b) after overdischarge. The thickness of the air pocket in the large-capacity pouch-type full-cell (c) before and (d) after overdischarge. The thickness of electrodes in the large-capacity pouch-type full-cell (e) before and (f) after overdischarge.

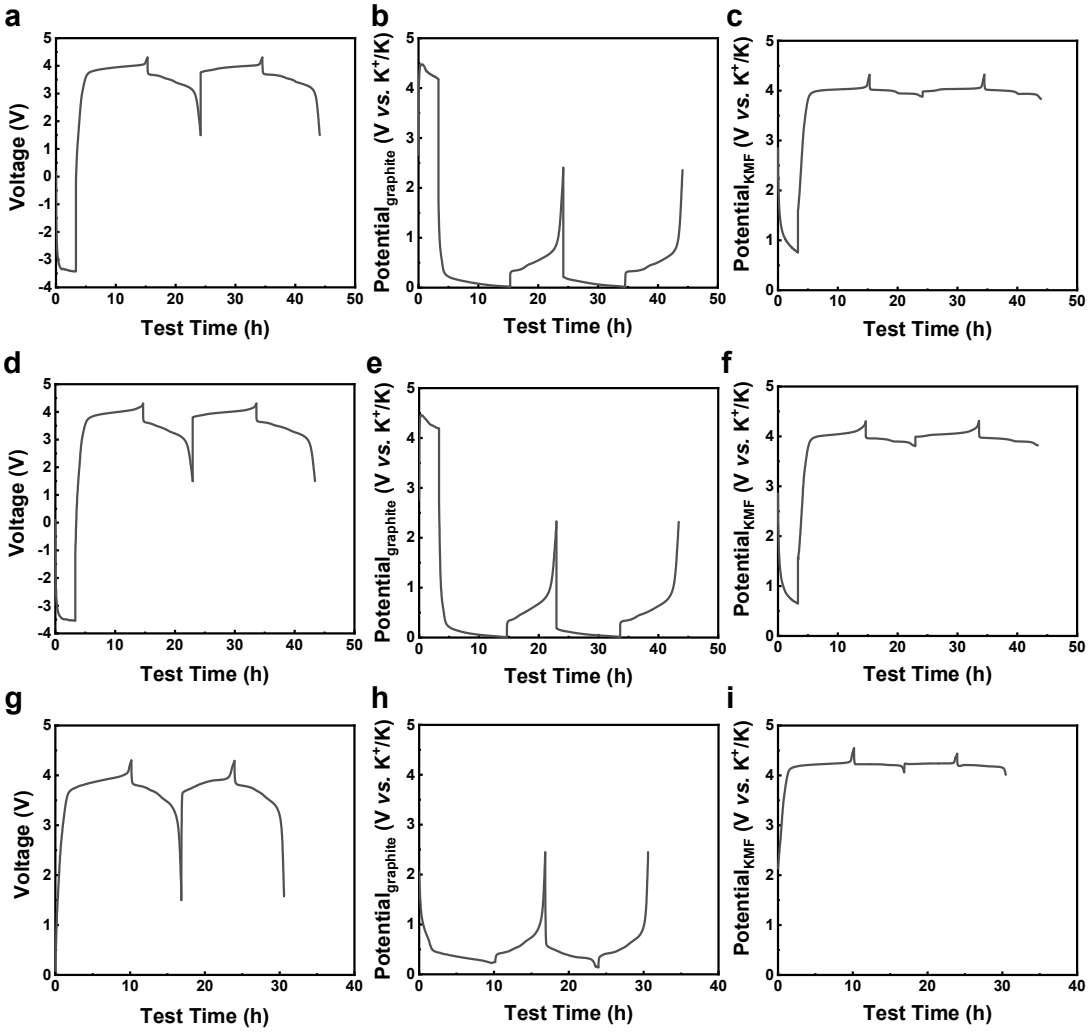

Fig. S41 Electrochemical performance of the three-electrode KMF-graphite cells. (a) Galvanostatic overdischarge-charge-discharge voltage profiles of the KMF-50-graphite cell-1. Potential profiles of (b) graphite and (c) KMF in the KMF-50-graphite cell-1 (with respect to K metal reference electrode). (d) Galvanostatic overdischarge-charge-discharge voltage profiles of the KMF-50-graphite cell-2. Potential profiles of (e) graphite and (f) KMF in the KMF-50-graphite cell-2 (with respect to K metal reference electrode). (g) Galvanostatic charge-discharge voltage profiles of the KMF-graphite cell. Potential profiles of (h) graphite and (i) KMF in the KMF-graphite cell (with respect to K metal reference electrode).

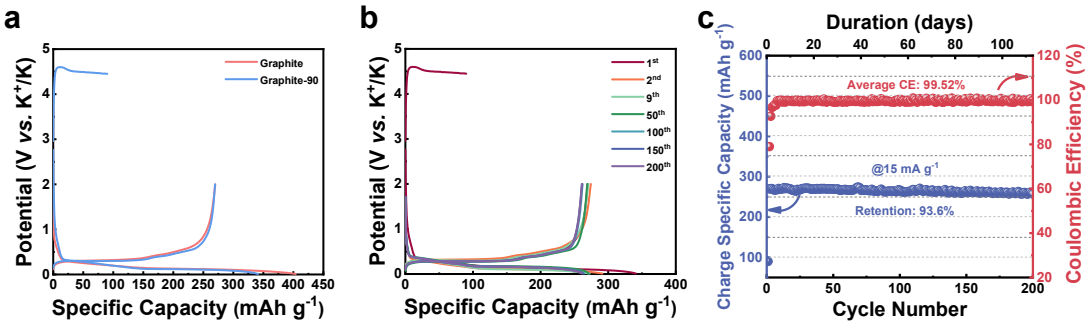

Fig. S42 Electrochemical performance of the graphite-K metal cell. (a) Comparison of the galvanostatic charge-discharge potential profiles of the graphite-K metal cell with or without initial overcharge. (b) Galvanostatic charge-discharge potential profiles and (c) cycling performance of the graphite-K metal cell at 15 mA g^{-1}, which is subject to initial overcharge.

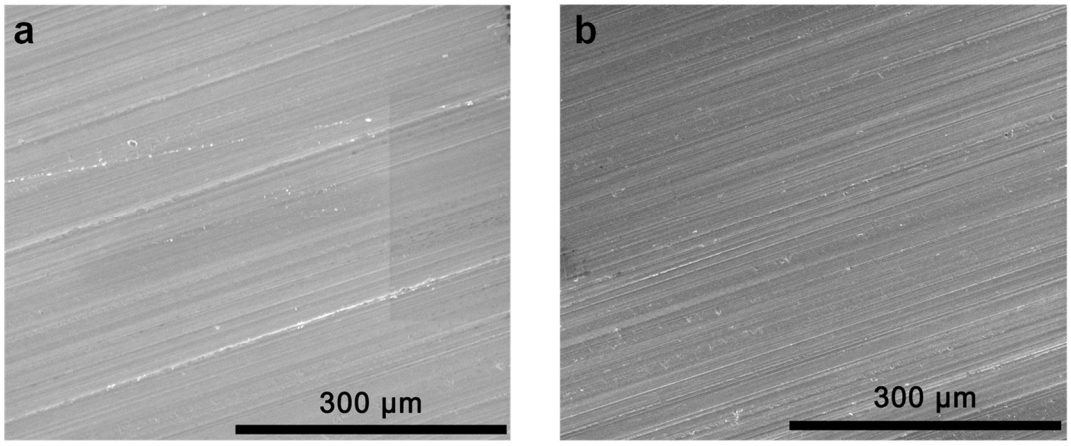

Fig. S43 SEM images of Al current collector on which graphite is loaded. (a) Before and (b) after the initial overcharge process of the graphite-K metal cell.

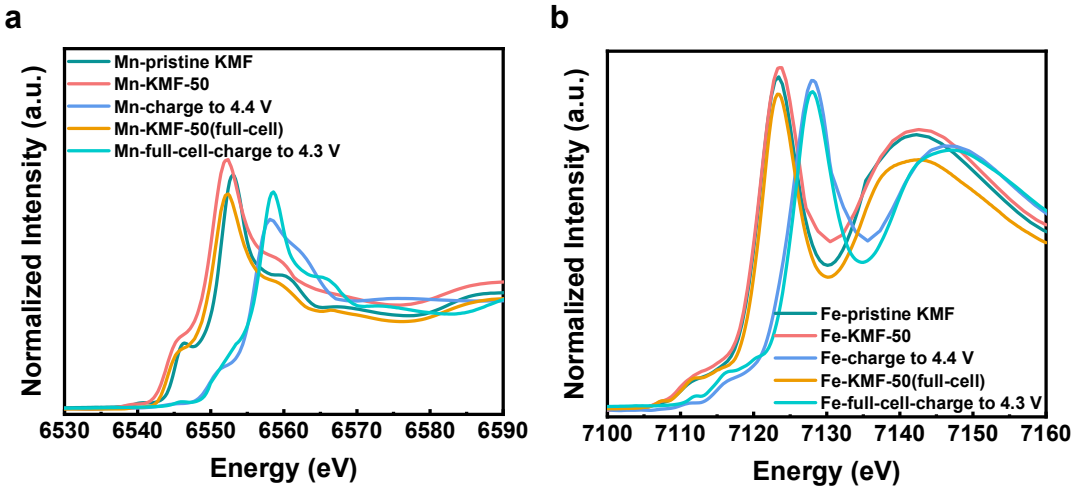

Fig. S44 The XANES analysis of KMF in the full- and half-cells. Recorded XANES (a) Mn and (b) Fe *K*-edge spectra for the KMF electrodes extracted from the KMF-K metal cell and KMF-graphite cell.

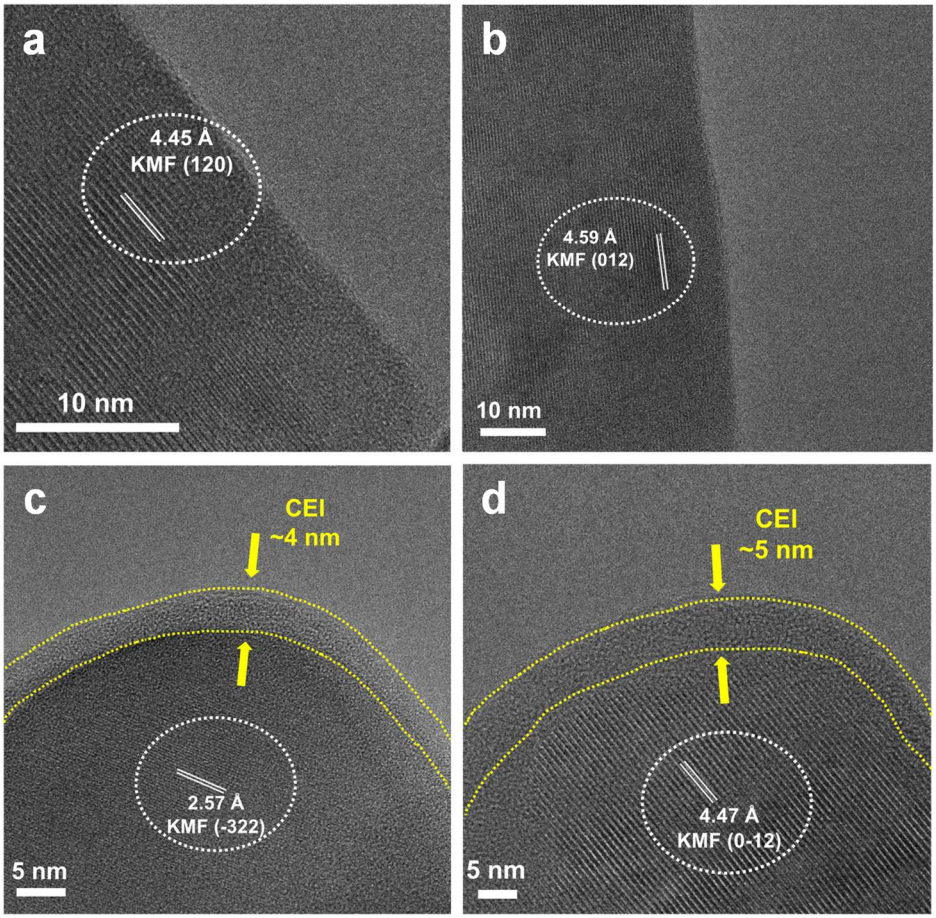

Fig. S45 Cryo-HRTEM images of different KMF samples. (a, b) KMF after initial overdischarge in the full-cell. (c, d) KMF after 100 cycles in the overdischarged full-cell.

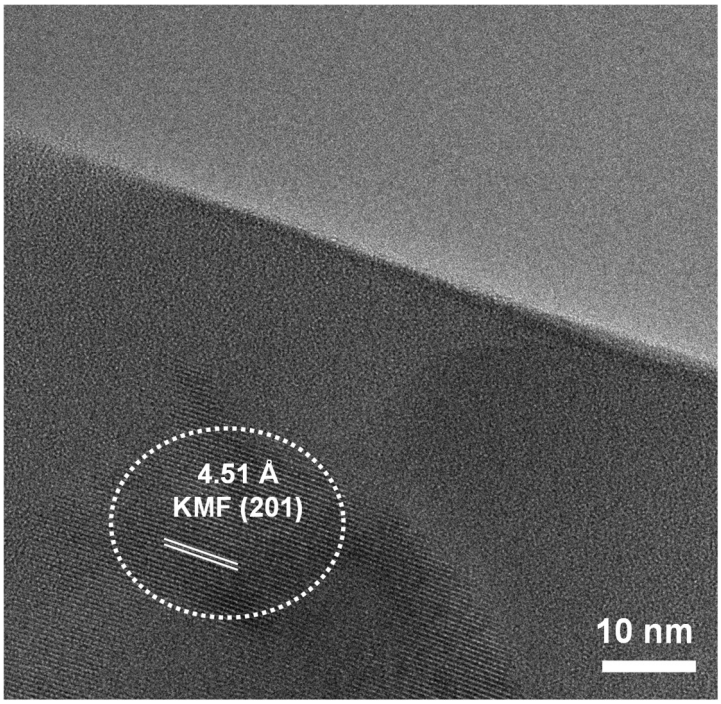

Fig. S46 Cryo-HRTEM image of the pristine KMF.

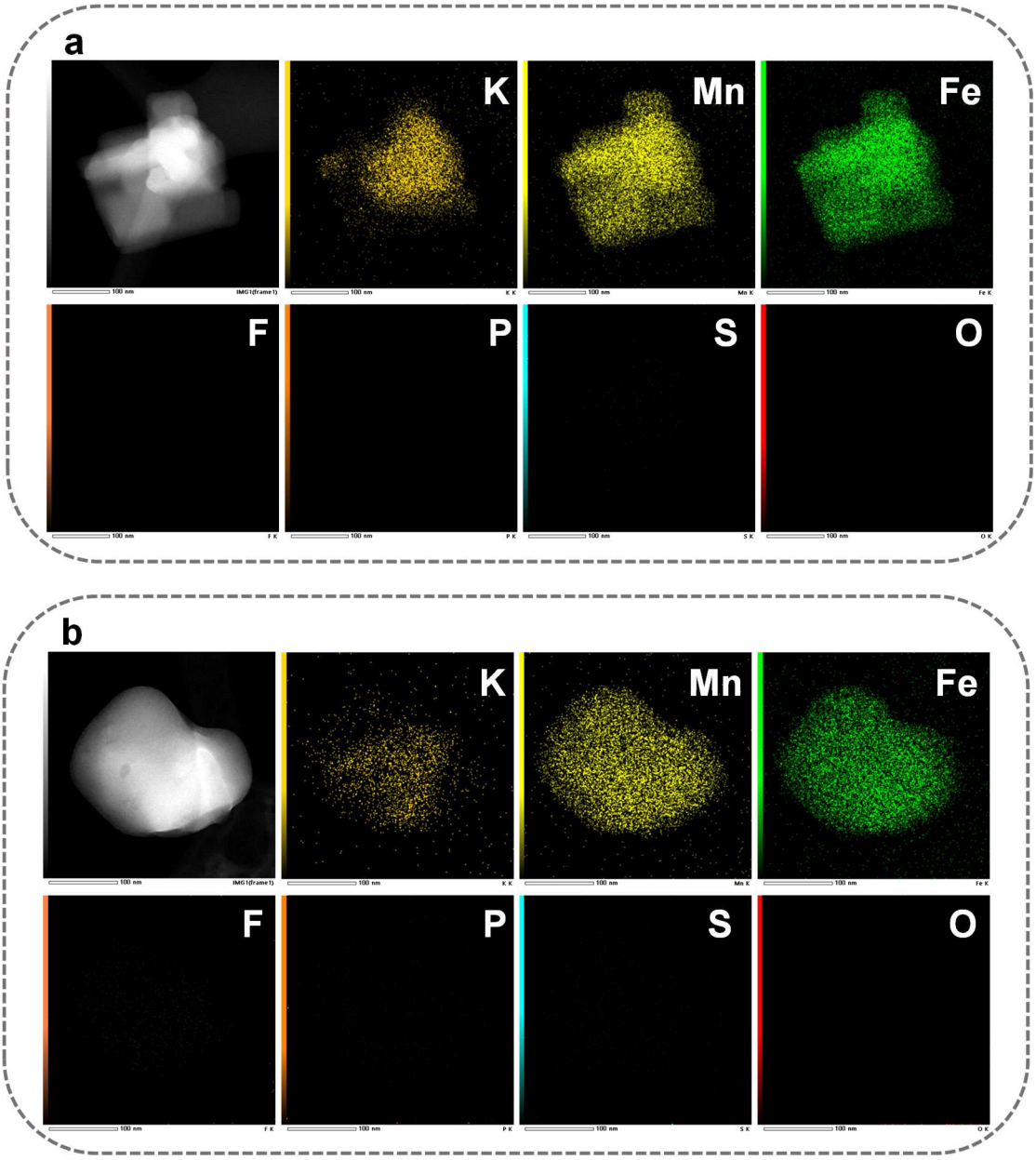

Fig. S47 Cryo-STEM image in different regions and the corresponding EDS elemental mapping of the KMF after initial overdischarge in the full-cell. (a) region 1 and (b) region 2.

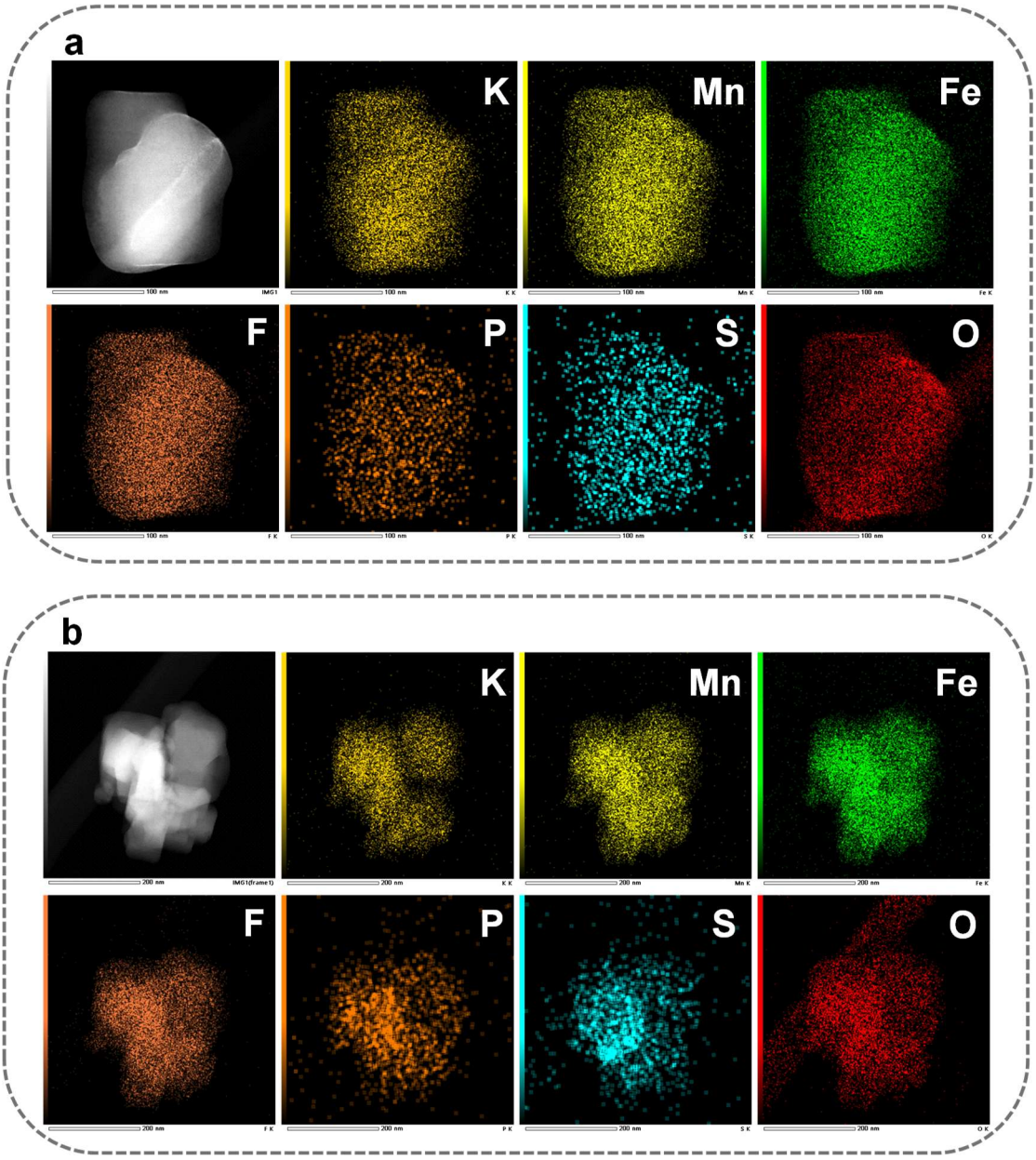

Fig. S48 Cryo-STEM image in different regions and the corresponding EDS elemental mapping of the KMF after 100 cycles in the overdischarged full-cell. (a) region 1 and (b) region 2.

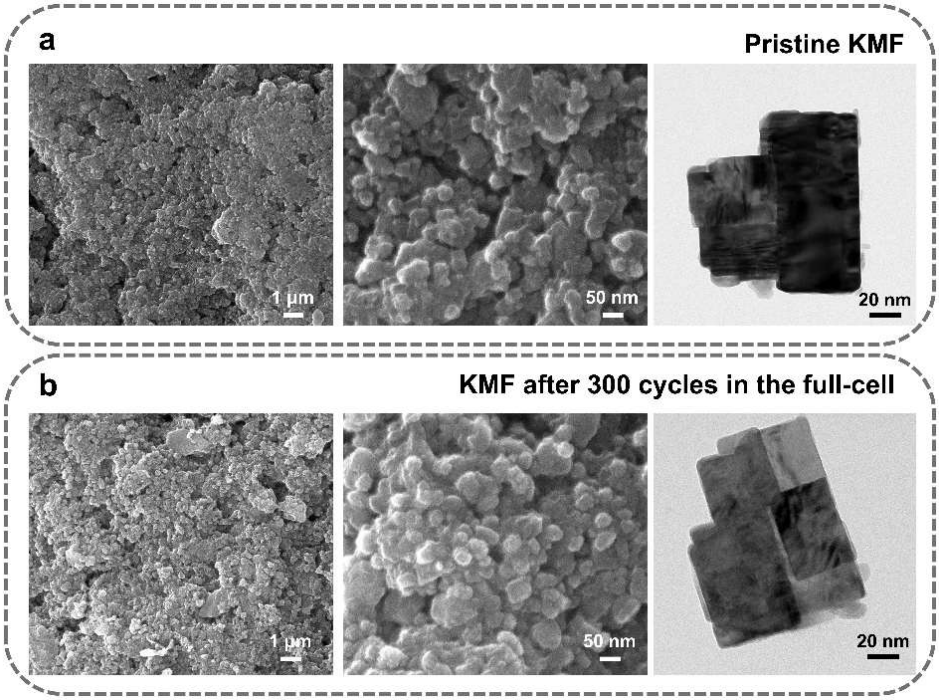

Fig. S49 SEM and TEM images of KMF electrodes at different stages. (a) Pristine KMF. (b) KMF after 300 cycles in the full-cell.

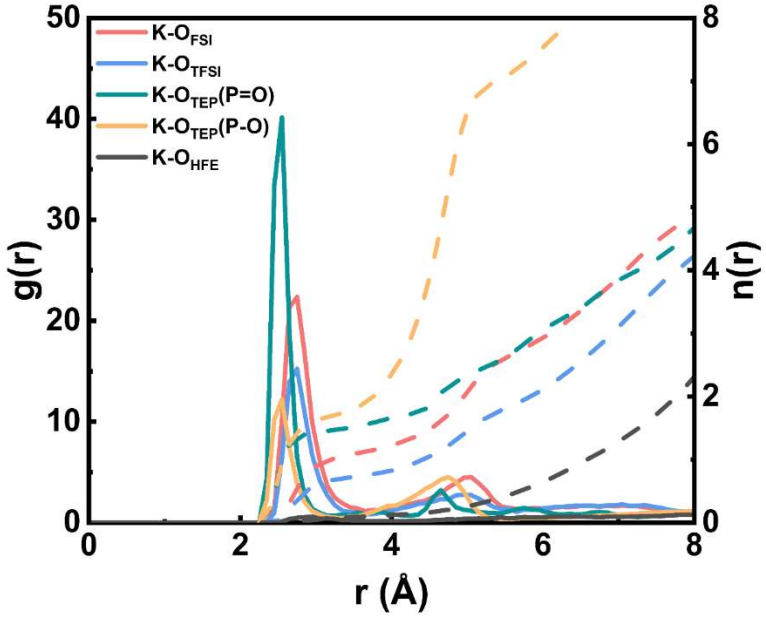

Fig. S50 Cumulative ion number density profiles. Radical distribution functions (RDFs, g(r), solid) and cumulative distribution functions (CDFs, n(r), dashed line) of oxygen around K^+ as a function of distance (r) from MD simulations in the electrolyte.

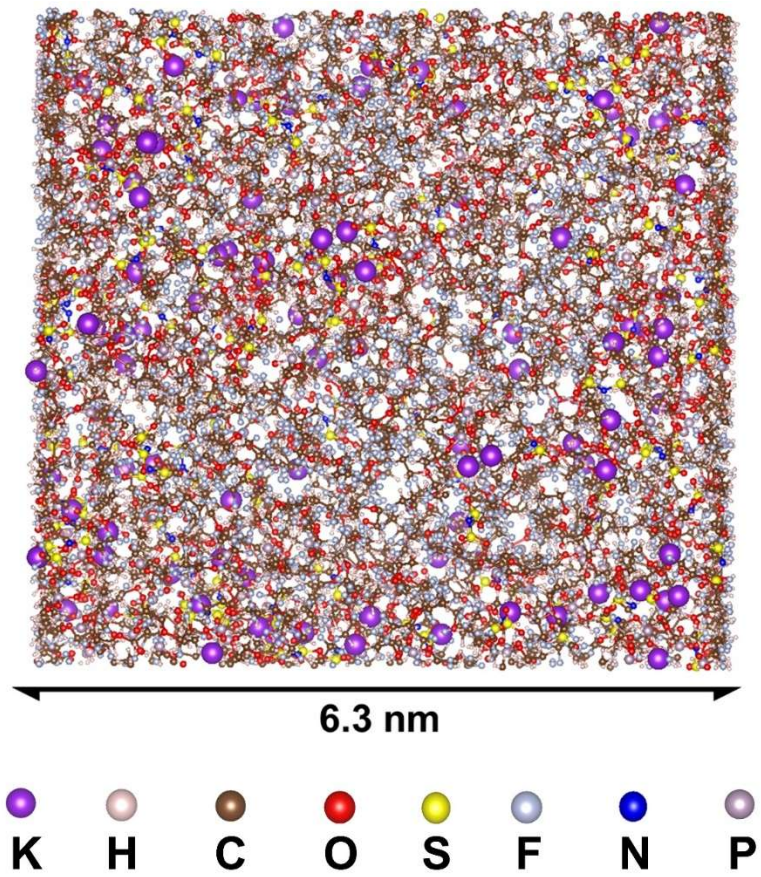

Fig. S51 Microscopic solvation structure of electrolyte obtained from cMD simulations.

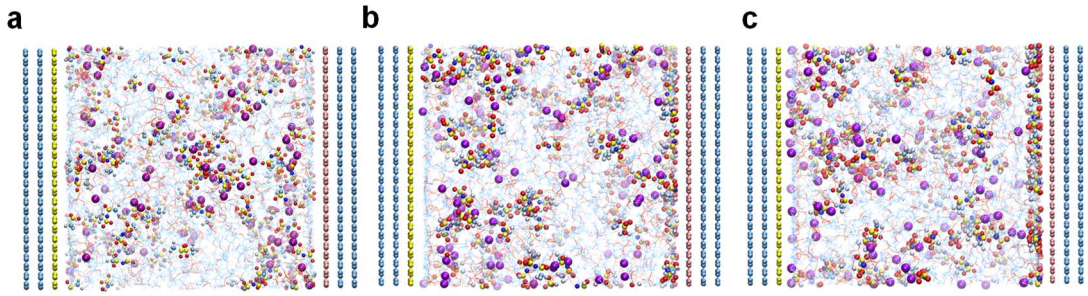

Fig. S52 Cumulative ion number density profiles. The simulated snapshot of ion distribution when (a) 0 μC cm^{-2}, (b) 5 μC cm^{-2}, and (c) 10 μC cm^{-2} charges are applied to the electrode.

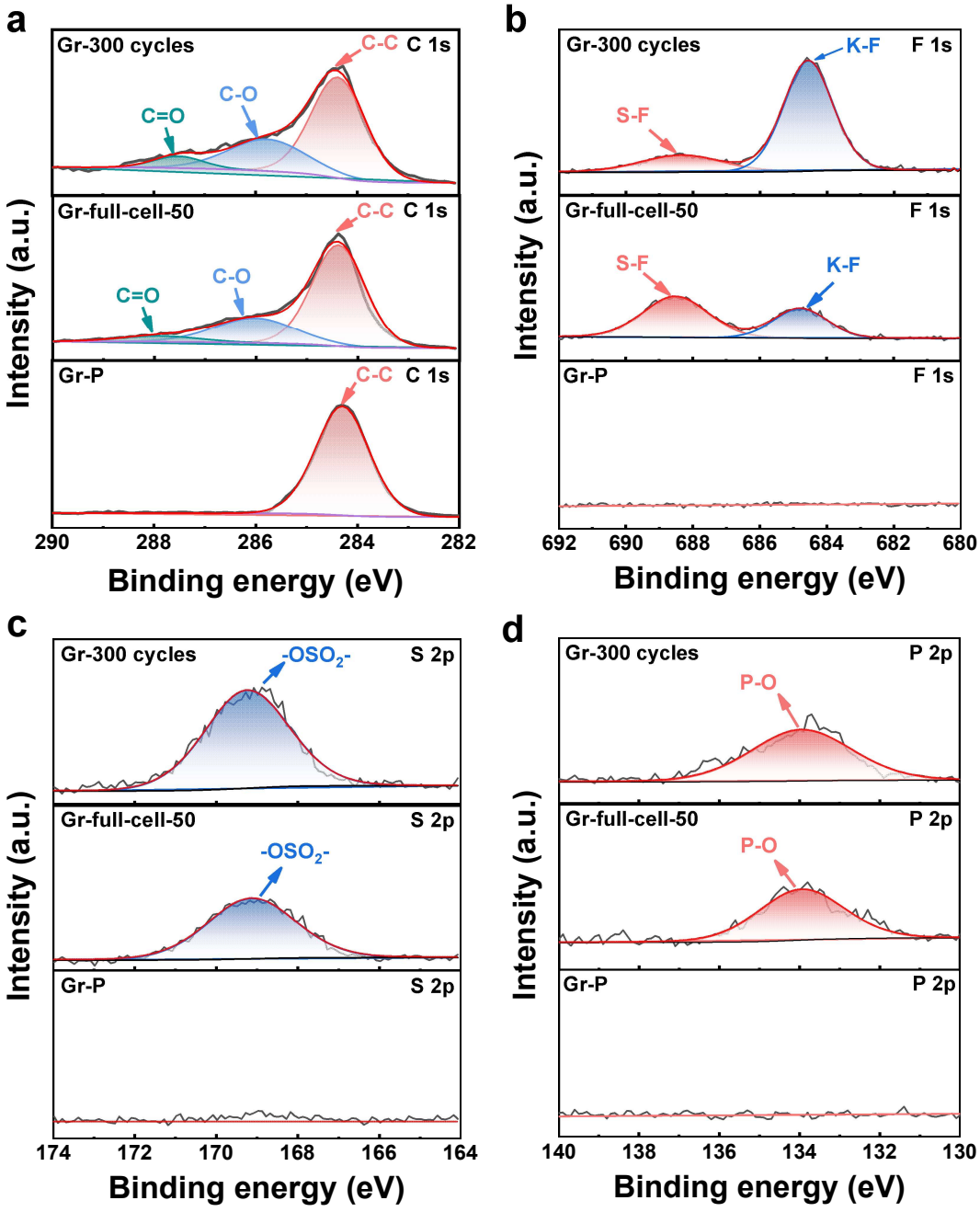

Fig. S53 XPS characterizations of different graphite samples. The XPS spectra of Gr-P, Gr-full-cell-50, and Gr-300 cycles, respectively. (a) The C 1*s*, (b) F 1*s*, (c) S 2*p*, and (d) P 2*p* spectra. Gr-P: pristine graphite powder; Gr-full-cell-50: the graphite electrode after overdischarging the KMF-graphite full-cell; Gr-300 cycles: the graphite electrode after 300 charge-discharge cycles in the overdischarged full-cell.

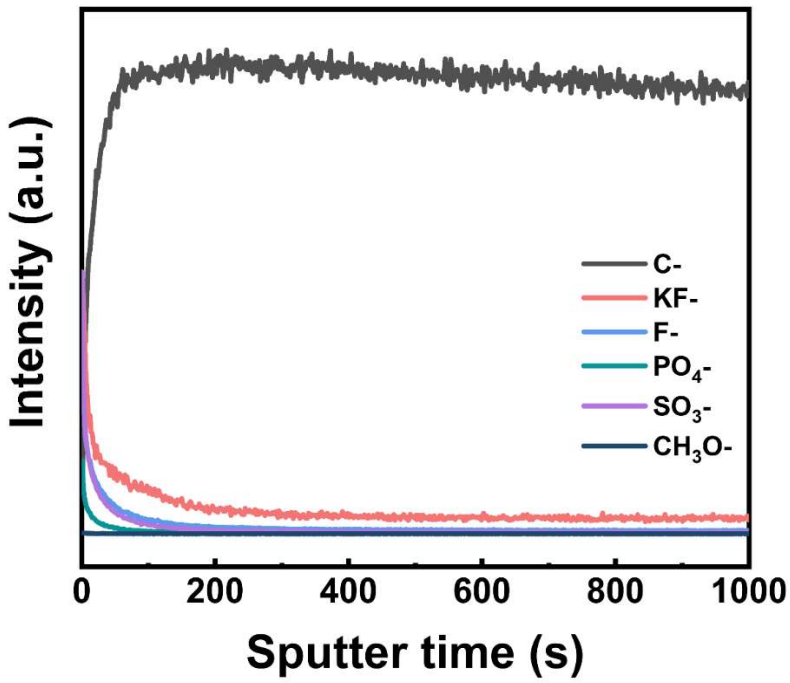

Fig. S54 Characterizations of graphite surface. ToF-SIMS depth profiling curves of the graphite electrode in negative mode. Note: the graphite electrode is obtained from the KMF-graphite full-cell after initial overdischarge.

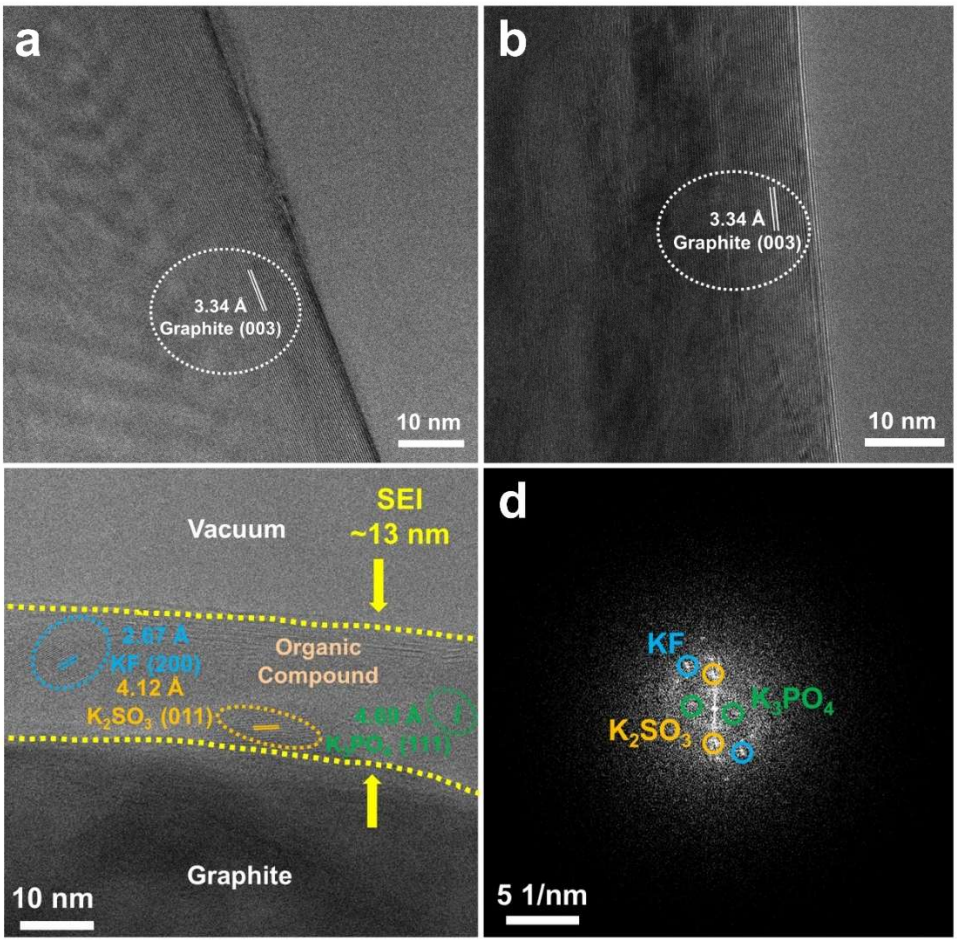

Fig. S55 Characterizations of graphite surface. (a, b) Cryo-HRTEM images of the pristine graphite. (c, d) Cryo-HRTEM image of the SEI formed on the surface of graphite in the KMF-graphite full-cell after initial overdischarge, accompanied by the corresponding FFT images depicted in (d).

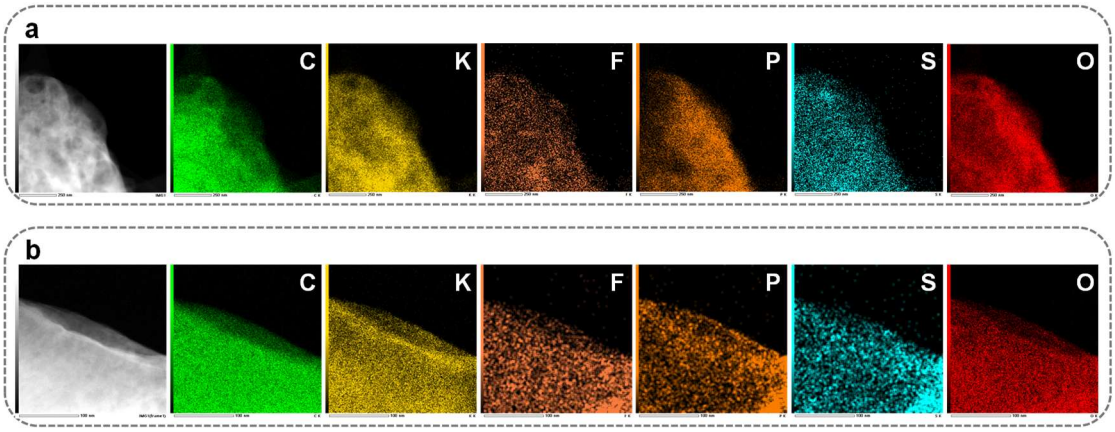

Fig. S56 Characterizations of graphite surface. Cryo-STEM image and the corresponding EDS elemental mapping of the different graphite samples. (a) Graphite in the KMF-graphite full-cell after initial overdischarge. (b) Graphite after 100 cycles in the overdischarged KMF-graphite full-cell.

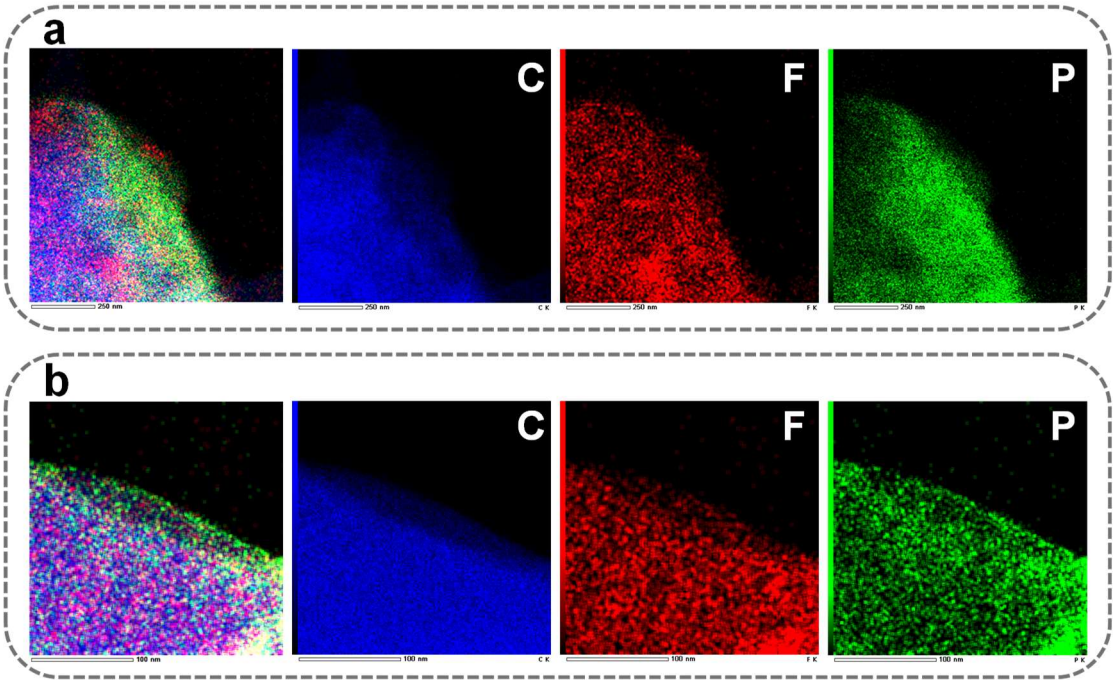

Fig. S57 Characterizations of graphite surface. The EDS elemental mapping of C, F, and P in the different graphite samples. (a) Graphite in the KMF-graphite full-cell after initial overdischarge. (b) Graphite after 100 cycles in the overdischarged KMF-graphite full-cell.

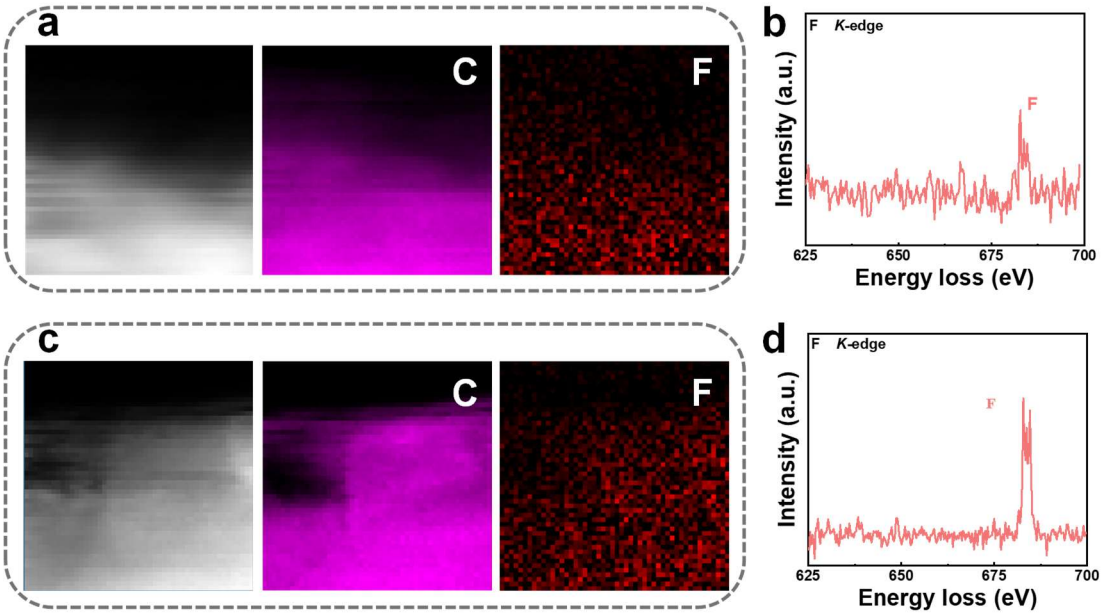

Fig. S58 Characterizations of graphite surface. (a) HAADF image and elemental *K*-edge mapping of C (pink) and F (red) performed by STEM-EELS spectrum imaging of graphite in the KMF-graphite full-cell after initial overdischarge. (b) F *K*-edge EELS spectrum of graphite in the KMF-graphite full-cell after initial overdischarge. (c) HAADF image and elemental *K*-edge mapping of C (pink) and F (red) performed by STEM-EELS spectrum imaging of graphite after 100 cycles in the overdischarged KMF-graphite full-cell. (d) F *K*-edge EELS spectrum of graphite after 100 cycles in the overdischarged KMF-graphite full-cell.

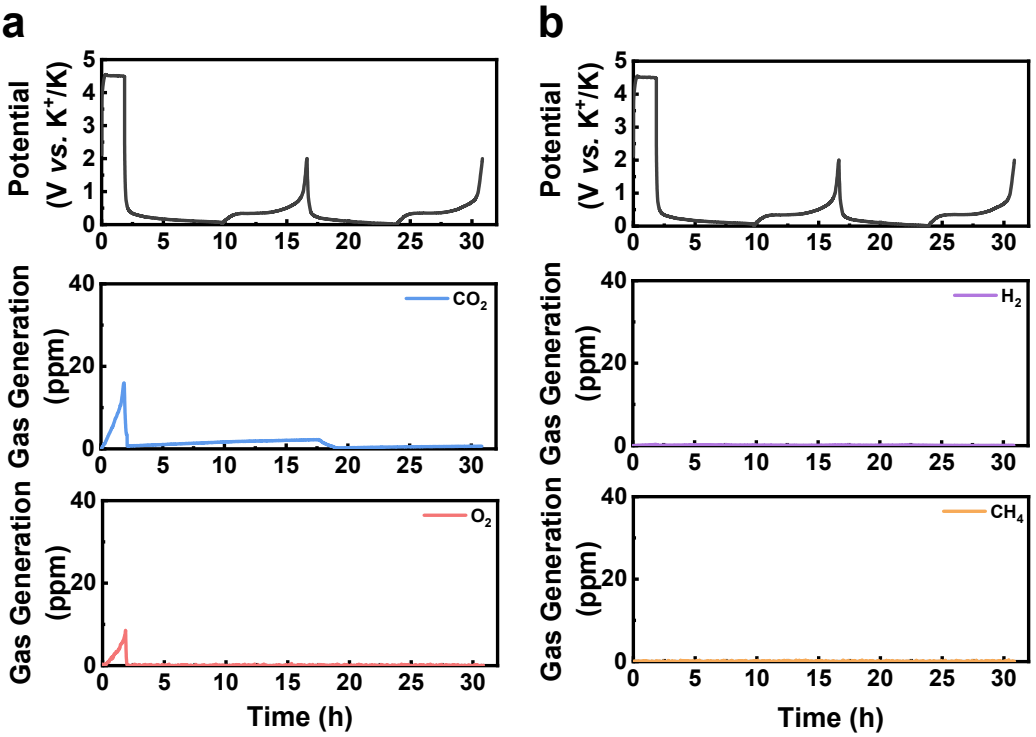

Fig. S59 *In-situ* gas analysis of the graphite-K metal cells subject to initial overcharge. (a) Potential profiles of the graphite electrode in the graphite-K cell, CO_2 and O_2 evolution profiles for the graphite anodes as obtained *via* DEMS. (b) Potential profiles of the graphite electrode in the graphite-K cell, H_2 and CH_4 evolution profiles for the graphite anodes as obtained *via* DEMS.

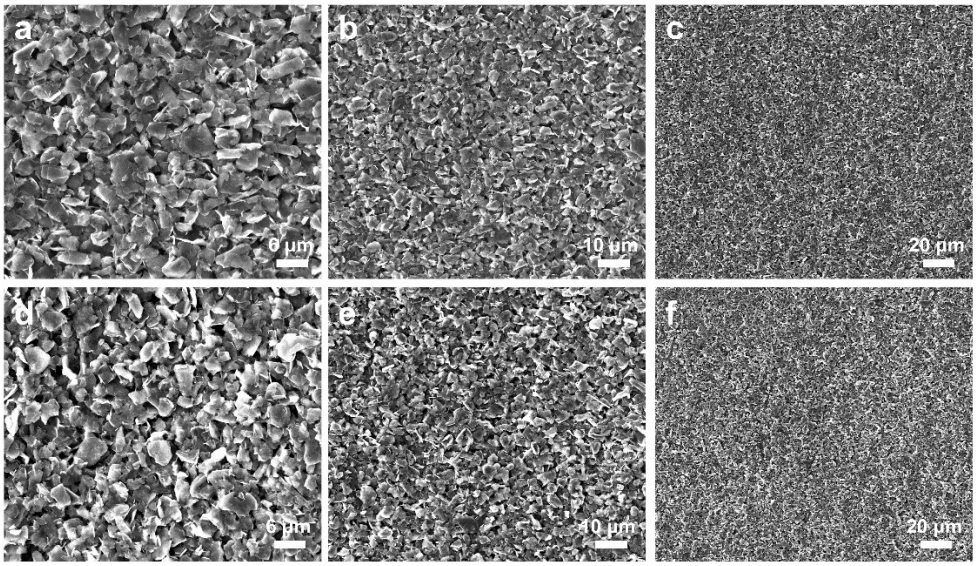

Fig. S60 SEM images of graphite electrodes at different states. (a-c) The pristine graphite electrode. (d-f) The graphite electrode after overdischarge in the full-cell.

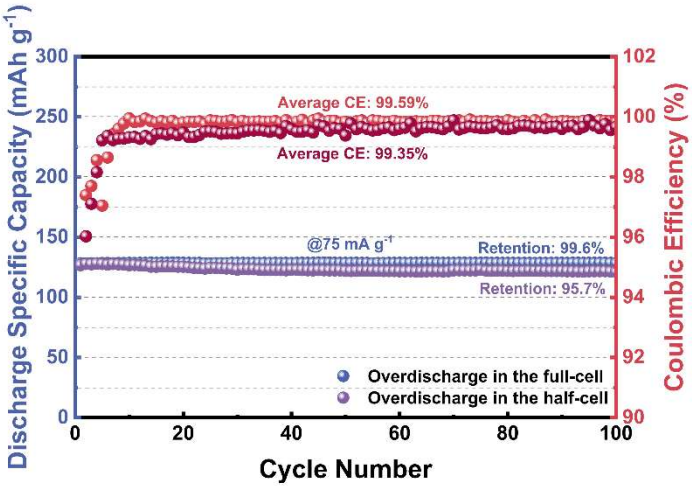

Fig. S61 Cycling performance comparison of full-cells formed by cathode-only pre-potassiation and by the direct full-cell overdischarge protocol.

Table S1. Structural parameters of the as-synthesized KMF sample obtained from Rietveld refinement analysis

Atom	Wyckoff	x	y	z	Occupancy
K	4e	0.751593	0.937367	0.479968	0.98
Fe	2a	0	0	0	1
Mn	2a	0	0.5	0.5	1
C1	4e	0.589868	0.668617	0.195488	1
C2	4e	0.951517	0.734881	0.168736	1
C3	4e	0.704385	0.526161	0.57285	1
N1	4e	0.465781	0.235909	0.837962	1
N2	4e	0.031368	0.351328	0.741322	1
N3	4e	0.202741	0.472606	0.396321	1

S.G. $P2_{1/n}$ a=10.075675 Å, b=7.301648 Å, c=6.932913 Å

α=γ=90°, β=90.246°, volume=510.043 $Å^3$, R_p=1.83%, R_{wp}=2.65%

Table S2. Structural parameters of the KMF-50 sample obtained from Rietveld refinement analysis

Atom	Wyckoff	x	y	z	Occupancy
K	4e	0.75152	0.937407	0.47991	1.31
Fe	2a	0	0	0	1
Mn	2a	0	0.5	0.5	1
C1	4e	0.589851	0.668594	0.195423	1
C2	4e	0.951591	0.735487	0.168328	1
C3	4e	0.704085	0.525963	0.573106	1
N1	4e	0.465439	0.236446	0.838127	1
N2	4e	0.031162	0.350761	0.741175	1
N3	4e	0.203117	0.472632	0.396142	1

S.G. $P2_{1/n}$ a=10.063584 Å, b=7.291874 Å, c=6.924734 Å

α=γ=90°, β=90.283°, volume=508.147 $Å^3$, R_p=1.86%, R_{wp}=2.51%

Table S3. ICP results for the different KMF samples

Sample	K:Mn:Fe*	Molecular formula**
KMF	1.96:1:0.992	$K_{1.96}Mn[Fe(CN)_6]_{0.992}$
KMF-30	2.35:1:0.993	$K_{2.35}Mn[Fe(CN)_6]_{0.993}$
KMF-50	2.62:1:0.996	$K_{2.62}Mn[Fe(CN)_6]_{0.996}$
KMF-70	2.86:1:0.995	$K_{2.86}Mn[Fe(CN)_6]_{0.995}$
KMF-90	3.11:1:0.995	$K_{3.11}Mn[Fe(CN)_6]_{0.995}$
KMF-120	3.51:1:0.994	$K_{3.51}Mn[Fe(CN)_6]_{0.994}$
KMF-150	3.91:1:0.991	$K_{3.91}Mn[Fe(CN)_6]_{0.991}$

*The uncertainties for the measured molar ratio of K and Fe versus Mn are 0.5% and 0.1%, respectively.

**The molecular formula of the samples is calculated based on the ICP-MS results of the KMF and KMF-50 samples.

Table S4. EXAFS fitting parameters at the Mn *K*-edge for various samples (S_0^2=0.97 from Mn-foil)

Sample	shell	CN[a]	R[b](Å)	σ^{2c}(Å^2)	ΔE_0[d](eV)	R factor
Mn-foil	Mn-Mn	2.0±0.1	2.69±0.01	0.0066	8.8±1.9	0.0126
MnO	Mn-O	6	2.20±0.01	0.0092	-4.3±0.4	0.0043
	Mn-Mn	12	3.13±0.01	0.0095		
Mn_2O_3	Mn-O	3.6±0.3	1.91±0.01	0.0046	-7.5±1.9	0.0061
	Mn-Mn1	5.9±0.7	3.11±0.02	0.0064	-1.8±3.1	
	Mn-Mn2	6.0±1.2	3.51±0.02	0.0087	-16.3±4.7	
MnO_2	Mn-O	4.9±0.3	1.89±0.01	0.0030	-6.4±1.3	0.0165
	Mn-Mn1	3.3±0.4	2.87±0.01	0.0052		
	Mn-Mn2	2.8±0.5	3.44±0.01	0.0039		
Mn-KMF	Mn-N	5.9±0.5	2.19±0.01	0.0051	-4.0±1.8	0.0189
Mn-KMF-50	Mn-N	5.6±0.4	2.16±0.01	0.0010	-1.3±1.8	0.0094
Mn-KMF-150	Mn-N	6.0±0.6	2.15±0.01	0.0027	-5.1±2.3	0.0102
Mn-KMF-0.05 V	Mn-Mn	2.0±0.1	2.69±0.01	0.0066	8.8±1.9	0.0126
Mn-charge to 4.4 V	Mn-N	4.2±0.4	1.97±0.01	0.0010	10.0±1.8	0.0195
Mn-discharge to 2.7 V	Mn-N	5.9±0.5	2.19±0.02	0.0030	-6.6±1.5	0.0183

[a]*CN*: coordination numbers; [b]*R*: bond distance; [c]σ^2: Debye-Waller factors; [d] ΔE_0: the inner potential correction. R factor: goodness of fit. Error bounds that characterize the structural parameters obtained by EXAFS spectroscopy were estimated as CN±20%; R ± 1%; σ^2 ± 20%.

Table S5. EXAFS fitting parameters at the Fe *K*-edge for various samples (S_0^2=0.76 from Fe-foil)

Sample	shell	can	R[b](Å)	σ^{2c}(Å^2)	ΔE_0[d](eV)	R factor
Fe-foil	Fe-Fe1	8	2.47±0.01	0.0049	6.8±1.1	0.0036
	Fe-Fe2	6	2.85±0.01	0.0060		
FeO	Fe-O	6	2.12±0.01	0.0144	3.3±0.7	0.0102
	Fe-Fe	12	3.07±0.01	0.0120		
Fe_2O_3	Fe-O1	3	1.93±0.01	0.0062	-2.4±1.0	0.0061
	Fe-O2	3	2.09±0.01	0.0099		
	Fe-Fe1	1	2.90±0.01	0.0041		
	Fe-Fe2	3	2.97±0.01	0.0070		
	Fe-Fe3	3	3.35±0.01	0.0070		
Fe-KMF	Fe-C	5.9±0.6	1.84±0.01	0.0043	-4.5±2.2	0.0122
Fe-KMF-50	Fe-C	5.7±0.4	1.85±0.01	0.0033	-2.2±1.5	0.0110
Fe-KMF-150	Fe-C	6.0±0.7	1.86±0.01	0.0082	-4.1±1.7	0.0195
Fe-KMF-0.05 V	Fe-Fe1	6.2±0.3	2.46±0.01	0.0048	6.0±2.1	0.0056
	Fe-Fe2	5.9±0.8	2.83±0.01	0.0072		
Fe-charge to 4.4 V	Fe-C	5.9±0.6	1.90±0.01	0.0063	-2.1±1.7	0.0115
Fe-discharge to 2.7 V	Fe-C	5.8±0.3	1.84±0.01	0.0041	-0.8±1.5	0.0113

[a]*CN*: coordination numbers; [b]*R*: bond distance; [c]σ^2: Debye-Waller factors; [d] ΔE_0: the inner potential correction. R factor: goodness of fit. Error bounds that characterize the structural parameters obtained by EXAFS spectroscopy were estimated as CN±20%; R ± 1%; σ^2 ± 20%.

Table S6. Calculation of crystal structure parameters of KMF with different K-ion content

Sample	a (Å)	b (Å)	c (Å)	α (°)	β (°)	γ (°)	V*(Å^3)	σ**
KMF	8.185	8.057	8.185	90.000	90.000	91.143	539.68	0.9993
$K_{2.5}$MF-3	8.113	8.077	8.062	87.800	91.79	92.947	527.05	0.9950
$K_{2.75}$MF-6	8.144	8.174	7.985	87.131	93.097	94.224	528.78	0.9947
K_3MF-1	8.261	8.151	7.912	89.969	91.508	92.662	531.99	0.9972
K_4MF-1	8.789	8.768	7.661	88.121	91.622	89.835	589.83	0.9991

*$V = abc\sqrt{1-(\cos\alpha)^2-(\cos\beta)^2-(\cos\gamma)^2+2\cos\alpha\cos\beta\cos\gamma}$

**$\sigma = \sqrt{1-(\cos\alpha)^2-(\cos\beta)^2-(\cos\gamma)^2+2\cos\alpha\cos\beta\cos\gamma}$

In the above equations, α, β, and γ need to be converted into radians. In the K_xMF, there are different σ values for different x values, which are used to characterize the degree of inclination of the cell, or the degree of deviation from the cubic lattice. The smaller the σ value, the greater the degree of tilt or deviation.

Table S7. The Bader charge and electron transfer of Mn and Fe atom in the K_xMF

Sample	Mn		Fe	
	Bader charge	Electron transfer	Bader charge	Electron transfer
K_0MF	5.02	1.98	6.68	1.32
K_1MF-2	5.10	1.90	6.75	1.25
K_2MF	5.46	1.54	6.92	1.08
$K_{2.5}MF$-3	5.68	1.32	7.02	0.98
$K_{2.75}MF$-6	5.79	1.21	7.06	0.94
K_3MF-1	5.88	1.12	7.10	0.90
K_4MF-1	6.25	0.75	7.29	0.71

Table S8. Specific energy of some reported K-ion full-cells

Cathode-Anode materials	Cathode : anode mass ratio	Average discharge voltage (V)	Discharge capacity (mAh g^{-1} — cathode +anode)	Specific energy* (Wh kg^{-1})
KMF-Graphite (This work)	**1 : 0.55**	**3.6**	**94.4**	**339.9**
$K_{0.7}Mn_{0.67}Ni_{0.33}O_2$-pitch-derived soft carbon[34]	1 : 0.42	2.03	84.5	171.5
$K_{1.7}Fe[Fe(CN)_6]_{0.9}$-Graphite[35]	1:0.4	2.94	71.2	209.2
$K_{1.72}Fe[Fe(CN)_6]_{0.96}{\cdot}0.342H_2O$-Graphite[36]	1:0.6	2.83	76.6	216.7
PTCDA-C@$PbTi_{0.9}Mo_{0.1}O_3$[37]	1 : 0.83	2.67	45.4	121.3
$K_{1.75}Mn[Fe(CN)_6]_{0.93}{\bullet}0.16H_2O$-Graphite[38]	1 : 0.6	3.5	68.8	240.8
$K_{0.61}Fe[Fe(CN)_6]_{0.92}{\bullet}0.32H_2O$-Graphite[39]	1 : 1	2.9	40	116
$K_{0.22}Fe[Fe(CN)_6]_{0.805}{\bullet}4.01H_2O$-Super P[40]	1.1 : 1	2.2	34.8	76.6
$K_{1.92}Fe[Fe(CN)_6]_{0.94}{\bullet}0.5H_2O$-$K_2TP$[41]	1 : 0.6	2.8	68.8	192.6
KMn[Fe(CN)$_6$]-BP@Fe_3O_4-NCs@FC[42]	1 : 0.16	2.6	66.6	173.2
KFe[Fe(CN)$_6$]-CNS-1000[43]	1 : 1	2.8	70.2	196.5
$K_3V_2(PO_4)_2F_3$-Graphite[44]	1 : 0.48	3.4	56.8	193.1
$KVPO_4F$-Graphite[45]	1 : 1	3.75	32.5	121.9
KFe[Fe(CN)$_6$]-*on*-CZL[46]	1 : 0.5	2.5	51.8	129.5

$K_2C_6O_6$-$K_4C_6O_6$[47]	1 : 1.2	1.1	31.8	35
$K_{0.5}MnO_2$-Graphite[48]	1 : 0.5	2.64	73.7	194.6
$K_{0.3}MnO_2$-Hard carbon /carbon black[49]	1.35 : 1	2.05	51.7	106
$K_{0.7}Fe_{0.5}Mn_{0.5}O_2$-Soft carbon[50]	2.1 : 1	1.6	55.5	88.8
$K_{0.6}CoO_2$-Hard carbon[51]	3 : 1	1.9	54	102.6
$KCrO_2$-Graphite[52]	3 : 1	1.9	67.5	128.3
$K_{0.6}CoO_2$-Graphite[53]	2 : 1	2.5	35.3	88.3
$K_{0.65}Fe_{0.5}Mn_{0.5}O_2$-Hard carbon[54]	2.1 : 1	2	51.4	102.8
$K_{0.77}MnO_2$•$0.23H_2O$-Hard-soft composite carbon[55]	1.8 : 1	1.8	77	138.6
PTCDA-FCNC-500[56]	1 : 0.52	1.32	101.9	134.5
PTCDA-Co-SNCS-t[57]	1 : 0.5	1.2	55.5	91.7
PTCDA@450-N-$CoTe_2$/LTTC[58]	1 : 0.33	1.7	70.7	120.2
TiS_2-Bi@NC[59]	1 : 3.75	1.2	66.8	80.2
PTCDA-Co-NBC@BP@CA@K[60]	1 : 0.23	2.05	100.5	206
$KVPO_4F$-PTCDI[61]	1 : 0.67	1.95	30	58.5
KMnHCF-KTPF/C[62]	1 : 0.76	2.53	77.5	196.1
$K_{0.8}CrO_2$-Graphite[63]	1 : 1.4	2.3	33	72.6
$KFe[Fe(CN)_6]$-ZnTe@C/$Ti_3C_2T_x$[64]	1 : 1	2.1	52.5	110.3
$K_{0.51}V_2O_5$-Graphite[65]	1 : 1	2.53	47	119
KFeHCF -Graphite[66]	1 : 1	2.65	35	92.8
$K_{1.98}Mn[Fe(CN)_6]_{0.98}$-Graphite[67]	1 : 0.65	3.6	89.8	323.3

*The specific energy is calculated based on the total mass of anode and cathode active materials.

Table S9. Statistical probability of occurrence of various species at 2 nm from the positively charged C electrode

Charge	Species	Occurrence probability
5 μC cm^{-2}	K^+	0
	FSI^-	7.84%
	$TFSI^-$	21.94%
	TEP	23.74%
	HFE	46.47%
10 μC cm^{-2}	K^+	1.26%
	FSI^-	14.72%
	$TFSI^-$	25.85%
	TEP	28.43%
	HFE	29.75%

Supplementary references

1. L. Deng, J. Qu, X. Niu, J. Liu, J. Zhang, Y. Hong, M. Feng, J. Wang, M. Hu, L. Zeng, Q. Zhang, L. Guo and Y. Zhu, *Nat. Commun.*, 2021, **12**, 2167.
2. H. Funke, M. Chukalina and A. Rossberg, *Phys. Scr.*, 2005, **T115**, 232-234.
3. MANUEL MUÑOZ, PIERRE ARGOUL and F. FARGES, *Am. Mineral.*, 2003, **88**, 694-700.
4. S. Dhir, B. Jagger, A. Maguire and M. Pasta, *Nat. Commun.*, 2023, **14**, 3833.
5. S. Maintz, V. L. Deringer, A. L. Tchougréeff and R. Dronskowski, *J. Comput. Chem.*, 2016, **37**, 1030-1035.
6. S. Plimpton, *J. Comput. Phys.*, 1995, **117**, 1-19.
7. Arnau Cordomı´, Olle Edholm and J. J. Perez, *J. Chem. Theory Comput.*, 2009, **5**, 2125–2134.
8. José N. Canongia Lopes, Karina Shimizu, Agílio A. H. Pa´dua, Yasuhiro Umebayashi, Shuhei Fukuda, Kenta Fujii and S.-i. Ishiguro, *J. Phys. Chem. B*, 2008, **112**, 9449-9455.
9. B. Doherty, X. Zhong, S. Gathiaka, B. Li and O. Acevedo, *J. Chem. Theory Comput.*, 2017, **13**, 6131-6145.
10. L. S. Dodda, I. Cabeza de Vaca, J. Tirado-Rives and W. L. Jorgensen, *Nucleic Acids Res.*, 2017, **45**, W331-W336.
11. L. Martínez, R. Andrade, E. G. Birgin and J. M. Martínez, *J. Comput. Chem.*, 2009, **30**, 2157-2164.
12. A. I. Jewett, D. Stelter, J. Lambert, S. M. Saladi, O. M. Roscioni, M. Ricci, L. Autin, M. Maritan, S. M. Bashusqeh, T. Keyes, R. T. Dame, J.-E. Shea, G. J. Jensen and D. S. Goodsell, *J. Mol. Biol.*, 2021, **433**, 166841.
13. K. Momma and F. Izumi, *J. Appl. Crystallogr.*, 2011, **44**, 1272-1276.
14. William Humphrey, Andrew Dalke and K. Schulten, *J. Mol. Graph.*, 1996, **14**, 33-38.
15. A. Stukowski, *Modell. Simul. Mater. Sci. Eng.*, 2010, **18**, 015012.
16. L. Jiang, Y. Lu, C. Zhao, L. Liu, J. Zhang, Q. Zhang, X. Shen, J. Zhao, X. Yu, H. Li, X. Huang, L. Chen and Y.-S. Hu, *Nat. Energy*, 2019, **4**, 495-503.
17. H. Zhang, H. Wang, W. Li, Y. Wei, B. Wen, D. Zhai and F. Kang, *Adv. Funct. Mater.*, 2024,

2312368, DOI: 10.1002/adfm.202312368.

18. A. Mullaliu, J. Asenbauer, G. Aquilanti, S. Passerini and M. Giorgetti, *Small Methods*, 2019, **4**, 1900529.

19. Chuanyong Jing, Suqin Liu, Manish Patel and X. Meng, *Environ. Sci. Technol.*, 2005, **39**, 5481-5487.

20. X. Wan, Q. Liu, J. Liu, S. Liu, X. Liu, L. Zheng, J. Shang, R. Yu and J. Shui, *Nat. Commun.*, 2022, **13**, 2963.

21. B.-C. Hu, Z.-Y. Wu, S.-Q. Chu, H.-W. Zhu, H.-W. Liang, J. Zhang and S.-H. Yu, *Energy Environ. Sci.*, 2018, **11**, 2208-2215.

22. T. Kim, B. Song, A. J. G. Lunt, G. Cibin, A. J. Dent, L. Lu and A. M. Korsunsky, *Chem. Mater.*, 2016, **28**, 4191-4203.

23. M. Wang, Y. Yao, Y. Tian, Y. Yuan, L. Wang, F. Yang, J. Ren, X. Hu, F. Wu, S. Zhang, J. Wu and J. Lu, *Adv. Mater.*, 2023, **35**, 2210658.

24. T. Hosaka, S. Muratsubaki, K. Kubota, H. Onuma and S. Komaba, *J. Phys. Chem. Lett.*, 2019, **10**, 3296-3300.

25. L. Wang, J. Yang, J. Li, T. Chen, S. Chen, Z. Wu, J. Qiu, B. Wang, P. Gao, X. Niu and H. Li, *J. Power Sources*, 2019, **409**, 24-30.

26. S. Liu, J. Mao, L. Zhang, W. K. Pang, A. Du and Z. Guo, *Adv. Mater.*, 2020, **33**, 2006313.

27. Z. Wang, K. Luo, J.-F. Wu, P. Gao, K. Wang, S. Chen, J. Tu, X. Fan and J. Liu, *Energy Environ. Sci.*, 2024, **17**, 274-283.

28. J. Xu, J. Zhang, T. P. Pollard, Q. Li, S. Tan, S. Hou, H. Wan, F. Chen, H. He, E. Hu, K. Xu, X.-Q. Yang, O. Borodin and C. Wang, *Nature*, 2023, **614**, 694-700.

29. L. Fan, R. Ma, Q. Zhang, X. Jia and B. Lu, *Angew. Chem., Int. Ed.*, 2019, **58**, 10500-10505.

30. A.-M. Li, O. Borodin, T. P. Pollard, W. Zhang, N. Zhang, S. Tan, F. Chen, C. Jayawardana, B. L. Lucht, E. Hu, X.-Q. Yang and C. Wang, *Nat. Chem.*, 2024, **16**, 922-929.

31. X. Liu, T. Zhang, X. Shi, Y. Ma, D. Song, H. Zhang, X. Liu, Y. Wang and L. Zhang, *Adv. Sci.*, 2022, **9**, e2104531.

32. Doron Aurbach, Yair Ein-Eli, Orit Chusid (Youngman), Yaakov Carmeli, Matsliach Babai and H. Yamin, *J. Electrochem. Soc.*, 1994, **141**, 603-610.

33. Y. He, S. L. Dreyer, Y. Y. Ting, Y. Ma, Y. Hu, D. Goonetilleke, Y. Tang, T. Diemant, B. Zhou, P. M. Kowalski, M. Fichtner, H. Hahn, J. Aghassi-Hagmann, T. Brezesinski, B. Breitung and Y. Ma, *Angew. Chem., Int. Ed.*, 2023, e202315371, DOI: 10.1002/anie.202315371.

34. L. Duan, C. Shao, J. Liao, L. Song, Y. Zhang, R. Li, S. Guo, X. Zhou and H. Zhou, *Angew. Chem., Int. Ed.*, 2024, **63**, e202400868.

35. J. Zheng, X. Chu, H. Wang, R. Chen, H. Xia, L. Chen, Y. Lin, Y. Li, Z. Lin, M. Ma, Q. Lai and X. Fan, *Angew. Chem., Int. Ed.*, 2025, **64**, e202502016.

36. A. Li, Y. Man, J. Liao, L. Duan, X. Ji and X. Zhou, *Nano Lett.*, 2023, **23**, 10066-10073.

37. W. Yang, J. Huang, Q. Zheng, L. Chen, A. Orita, N. Saito, Z. Zhang, Y. Zhang and L. Yang, *Angew. Chem., Int. Ed.*, 2024, **63**, e202412706.

38. X. Bie, K. Kubota, T. Hosaka, K. Chihara and S. Komaba, *J. Mater. Chem. A*, 2017, **5**, 4325-4330.

39. Y.-H. Zhu, X. Yang, D. Bao, X.-F. Bie, T. Sun, S. Wang, Y.-S. Jiang, X.-B. Zhang, J.-M. Yan and Q. Jiang, *Joule*, 2018, **2**, 736-746.

40. C. Zhang, Y. Xu, M. Zhou, L. Liang, H. Dong, M. Wu, Y. Yang and Y. Lei, *Adv. Funct. Mater.*, 2016, **27**, 1604307.

41. J. Liao, Q. Hu, Y. Yu, H. Wang, Z. Tang, Z. Wen and C. Chen, *J. Mater. Chem. A*, 2017, **5**, 19017-19024.

42. Y. Xiao, F. Liu, H. Shi, L. Hou, G. Qin, C. Yuan and X. W. D. Lou, *Adv. Mater.*, 2023, e2301772, DOI: 10.1002/adma.202301772.

43. Y. Chen, B. Xi, M. Huang, L. Shi, S. Huang, N. Guo, D. Li, Z. Ju and S. Xiong, *Adv. Mater.*, 2022, **34**, e2108621.

44. X. Lin, J. Huang, H. Tan, J. Huang and B. Zhang, *Energy Storage Mater.*, 2019, **16**, 97-101.

45. Y. Gao, W. Li, B. Ou, S. Zhang, H. Wang, J. Hu, F. Kang and D. Zhai, *Adv. Funct. Mater.*, 2023, 2305829, DOI: 10.1002/adfm.202305829.

46. Y. Wang, J. Zeng, Y. Wang, C. Zhang, Q. Wang, L. Gao, D. Sun, X. Jiang, M. Hu, L. Yang, D. Xie, Y. Hao, Z. Hu and X. Wang, *Adv. Mater.*, 2024, **36**, 2410132.

47. Q. Zhao, J. Wang, Y. Lu, Y. Li, G. Liang and J. Chen, *Angew. Chem., Int. Ed.*, 2016, **55**,

12528-12532.

48. L. Deng, T. Wang, Y. Hong, M. Feng, R. Wang, J. Zhang, Q. Zhang, J. Wang, L. Zeng, Y. Zhu and L. Guo, *ACS Energy Lett.*, 2020, **5**, 1916-1922.

49. C. Vaalma, G. A. Giffin, D. Buchholz and S. Passerini, *J. Electrochem. Soc.*, 2016, **163**, A1295-A1299.

50. X. Wang, X. Xu, C. Niu, J. Meng, M. Huang, X. Liu, Z. Liu and L. Mai, *Nano Lett.*, 2017, **17**, 544-550.

51. T. Deng, X. Fan, C. Luo, J. Chen, L. Chen, S. Hou, N. Eidson, X. Zhou and C. Wang, *Nano Lett.*, 2018, **18**, 1522-1529.

52. H. Kim, D.-H. Seo, A. Urban, J. Lee, D.-H. Kwon, S.-H. Bo, T. Shi, J. K. Papp, B. D. McCloskey and G. Ceder, *Chem. Mater.*, 2018, **30**, 6532-6539.

53. H. Kim, J. C. Kim, S.-H. Bo, T. Shi, D.-H. Kwon and G. Ceder, *Adv. Energy Mater.*, 2017, **7**, 1700098.

54. T. Deng, X. Fan, J. Chen, L. Chen, C. Luo, X. Zhou, J. Yang, S. Zheng and C. Wang, *Adv. Funct. Mater.*, 2018, **28**, 1800219.

55. B. Lin, X. Zhu, L. Fang, X. Liu, S. Li, T. Zhai, L. Xue, Q. Guo, J. Xu and H. Xia, *Adv. Mater.*, 2019, **31**, e1900060.

56. X. Zhang, F. Wu, D. Fang, R. Chen and L. Li, *Angew. Chem., Int. Ed.*, 2024, **63**, e202404332.

57. S. Xiong, S. Liu, K. Sun, Q. Wu, Y. Gao, Y. Zhou, L. Hou and F. Gao, *Chem. Eng. J.*, 2025, **505**, 159921.

58. Q. Li, Z. Liang, Y. Huang, W. Zhang, S. Xie, Y. Zhong, C. Zhao, Z. Luo and S. Huang, *Adv. Mater.*, 2025, **37**, 2502894.

59. G. Chen, B. Feng, G. Xu, Q. Gong, L. Yan, C. Zhou, J. Jiang, L. Yang, Q. Wu, X. Wang and Z. Hu, *ACS Energy Lett.*, 2025, **10**, 1821-1828.

60. G. Qin, Q. Wang, Z. Qi, F. Liu and X. He, *Nano Energy*, 2025, **134**, 110541.

61. M. Xia, H. Fu, K. Lin, A. M. Rao, L. Cha, H. Liu, J. Zhou, C. Wang and B. Lu, *Energy Environ. Sci.*, 2024, **17**, 1255-1265.

62. J. Liao, X. Sheng, Z. Yuan, Y. Wang, F. Tu, H. Qi, C. Zhou, Q. Hu and X. Zhou, *Angew.*

Chem., Int. Ed., 2025, e202516467, DOI: 10.1002/anie.202516467.

63. N. Naveen, S. C. Han, S. P. Singh, D. Ahn, K.-S. Sohn and M. Pyo, *J. Power Sources*, 2019, **430**, 137-144.

64. R. Hu, D. Sha, X. Cao, C. Lu, Y. Wei, L. Pan and Z. Sun, *Adv. Energy Mater.*, 2022, **12**, 2203118.

65. Y.-H. Zhu, Q. Zhang, X. Yang, E.-Y. Zhao, T. Sun, X.-B. Zhang, S. Wang, X.-Q. Yu, J.-M. Yan and Q. Jiang, *Chem*, 2019, **5**, 168-179.

66. X. Ma, D. Zhang, H. Fu, A. M. Rao, J. Zhou, L. Fan and B. Lu, *Joule*, 2025, **9**, 101952.

67. X. Wang, C. Gao, S. Zhang, J. Li, J. Wang, S. Lin, S. Lee, F. Kang and D. Zhai, *Energy Environ. Sci.*, 2025, **18**, 7869-7881.